

Doping ZnO Nanoparticles with Rare-earth Element and Investigating Its Photocatalytic Activity

by

Sikder Ashikuzzaman Ayon

Student ID: 0417112003

MASTER OF SCIENCE IN MATERIALS AND METALLURGICAL ENGINEERING



Department of Materials and Metallurgical Engineering

BANGLADESH UNIVERSITY OF ENGINEERING AND TECHNOLOGY (BUET)

October, 2019

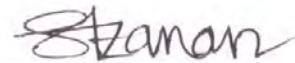
The thesis titled “Doping ZnO Nanoparticles with Rare-earth Element and Investigating Its Photocatalytic Activity” Submitted by Sikder Ashikuzzaman Ayon, Roll No. 0417112003 and Session: April 2017 has been accepted as satisfactory as a partial fulfilment of the requirement for the degree of M.Sc.Engg. in Materials and Metallurgical Engineering on October 27, 2019.

BOARD OF EXAMINERS

1. 
Dr. Md. Muktadir Billah
Assistant Professor
Department of Materials and Metallurgical Engineering, BUET
Chairman
(Supervisor)
2. 
Dr. Fahmida Gulshan
Professor and Head
Department of Materials and Metallurgical Engineering, BUET
Member
(Ex-officio)
3. 
Dr. Ahmed Sharif
Professor
Department of Materials and Metallurgical Engineering, BUET
Member
4. 
Dr. H. M. Mamun Al Rashed
Associate Professor
Department of Materials and Metallurgical Engineering, BUET
Member
5. 
Dr. Jiban Podder
Professor
Department of Physics, BUET
Member
(External)

CANDIDATE'S DECLARATION

Declared that except where specified by reference to other works, the experimental studies embodied in thesis is the result of investigation carried out by the author. Neither the thesis nor any part has been submitted to or is being submitted elsewhere for any other purposes.



Sikder Ashikuzzaman Ayon

ACKNOWLEDGEMENT

First, I would like to express my sincerest gratitude to the Almighty, the benevolent and the merciful, for His graciousness, unlimited kindness and divine blessings.

I would like to express my sincere gratitude to my thesis supervisor, Dr. Md. Muktadir Billah, Assistant Professor, MME, for his kind supervision, indispensable guidance, constructive suggestions and continuous encouragement during this thesis work. I am truly indebted to him for his esteemed guidance and encouragement from the beginning to the end of this thesis.

I would like to thank Prof. Dr. Fahmida Gulshan, Head, MME, for her continuous support and encouragement to excel in research and academia, and for allowing me to use the various facilities of MME without hindrance.

I would like to convey my regards to Prof. Dr. Mohammed Abdul Basith, Professor, Physics, for his constant and priceless help with experimental aspects of this research project and for allowing me to run experiment on Nanotechnology Research Laboratory, BUET.

I am immensely grateful to Dr. Md. Saiful Islam, Lecturer, GCE, for helping me unconditionally with the involving procedures of rietveld analysis.

A special thanks goes to Sajjad Hasan, M.Sc. student Physics, BUET, for his timely support to conduct various tests at Nanotechnology Research Laboratory, BUET.

I would like to thank all the member of GCE departments for their continuous support. Without their support the research would be difficult to complete.

Finally, I must express my very profound gratitude to my parents, my younger sister Urbi and to my wife Tonny, for providing me with unfailing support and continuous encouragement throughout my years of study and through the process of researching and writing this thesis. This accomplishment would not have been possible without them.

ABSTRACT

In this study, pristine and rare-earth elements doped ZnO nanoparticles were successfully synthesized as potential photocatalysts by modified sol-gel method. Synthesized nanoparticles were characterized using X-ray diffraction, field emission scanning electron microscopy, energy dispersion X-ray spectrum analysis, UV-visible diffuse reflectance spectroscopy, photoluminescence spectroscopy and simultaneous thermogravimetry-differential scanning calorimetry. ZnO nanoparticles were doped to enhance the photocatalytic degradation efficiency of the nanoparticles. Optimized process parameters were used to synthesize $Zn_{1-x}Ho_xO$ and $Zn_{1-x}Sm_xO$ nanoparticles ($x = 0.01, 0.03$ and 0.05). Rare earth elements were added to utilize their ability of introducing sideway band to reduce optical band gap and shift its photocatalytic activation towards visible range of the solar spectra. Also, the elements were added because of their electron scavenger nature to reduce photogenerated electron-hole recombination rate for better photocatalytic properties of the nanoparticles.

In the current exploration, modified sol-gel derived ZnO nanoparticles were effectively doped with rare earth elements i.e. Ho and Sm. Prior to doping, synthesis and annealing parameters were optimized to have pristine ZnO nanoparticles with enhanced photocatalytic properties. Effect of process parameters, chelating agent and dopants on the surface morphology of ZnO nanoparticles, along with particle size distribution (uniform size and bimodal), were studied steadily. Crystallization of the nanoparticles and successful doping were confirmed prior to their usage for photocatalytic degradation. Effect of doping on absorption edge shifting, to use visible spectra to a greater extent for photocatalytic degradation, was investigated thoroughly. Finally, doping concentrations were optimized for both Ho and Sm to maximize photocatalytic efficiency and all the findings were analyzed for understanding the fundamental mechanisms i. e. structure-property relationship and kinetics.

TABLE OF CONTENTS

CANDIDATE'S DECLARATION	Error! Bookmark not defined.
ACKNOWLEDGEMENT	iv
ABSTRACT	v
LIST OF FIGURES	ix
LIST OF TABLES	xii
1 INTRODUCTION	1
1.1 BACKGROUND AND RESEARCH MOTIVATION	1
1.2 OBJECTIVE OF THE PRESENT STUDY	2
2 LITERATURE REVIEW	3
2.1 PHOTOCATALYSIS	3
2.1.1 Homogeneous Photocatalysis	3
2.1.2 Heterogeneous Photocatalysis	4
2.2 PHOTOCATALYTIC MECHANISM	4
2.2.1 Oxidation Mechanism	5
2.2.2 Reduction Mechanism	6
2.3 ADVANTAGES OF PHOTOCATALYSIS FOR DYE DEGRADATION	7
2.4 CHARACTERISTICS OF PHOTOCATALYSTS	8
2.5 PHOTOCATALYTIC ACTIVITY ENHANCEMENT	8
2.6 ZnO AS POTENTIAL PHOTOCATALYST	8
2.7 PROPERTIES OF ZnO	10
2.7.1 Crystal Structure of ZnO	12
2.7.2 Electrical Properties	14
2.7.3 Optical Properties	14
2.8 FACTORS AFFECTING PHOTOCATALYTIC EFFICIENCY OF ZnO	15
2.8.1 Band Gap	15
2.8.2 Annealing Temperature	17
2.8.3 Initial Dye Concentration	18
2.8.4 Catalyst Loading	18
2.8.5 pH of Reaction Solution	19
2.9 LIMITATIONS AS PHOTOCATALYST	20
2.10 IMPROVEMENT OF ZnO AS PHOTOCATALYST	20
2.10.1 Metal/non-metal Doping	20
2.10.1.1 Potential Dopants: Rare-Earth Elements	21
2.10.2 Coupling with Other Semiconductors	22

2.10.3	Crystal Growth and Shape Control	23
2.10.4	Surface Modification of ZnO	23
2.11	METHODS OF ZnO NANOPARTICLES PRODUCTION	23
2.11.1	Mechanochemical Process	23
2.11.2	Controlled Precipitation	24
2.11.3	Sol-Gel Method	25
2.11.3.1	Modified Sol-gel Method.....	27
2.11.4	Solvothermal and Hydrothermal Method.....	27
2.11.5	Method Using an Emulsion or Microemulsion Environment	28
2.11.6	Other Methods	29
2.12	APPLICATIONS OF ZnO	29
2.12.1	Rubber Industry.....	29
2.12.2	The Pharmaceutical and Cosmetic Industries	30
2.12.3	The Textile Industry	30
2.12.4	The Electronics and Electrotechnology Industries	31
2.12.5	Miscellaneous Applications	32
3	EXPERIMENTAL	35
3.1	RAW MATERIALS	35
3.2	SYNTHESIS OF ZNO NANOPARTICLES.....	36
3.3	CHARACTERIZATIONS.....	38
3.3.1	X-ray Diffractometry (XRD)	38
3.3.2	Field Emission Scanning Electron Microscopy (FESEM).....	39
3.3.3	Differential Scanning Calorimetry (DSC) & Thermogravimetric Analysis (TGA)..	39
3.3.4	UV-vis Spectroscopy.....	40
3.3.5	Photoluminescence Spectroscopy	41
3.3.6	Photocatalytic Activity Measurement	41
4	RESULTS AND DISCUSSION	44
4.1	OPTIMIZATION OF ANNEALING TEMPERATURE	44
4.1.1	XRD for Different Annealing Temperatures.....	44
4.1.2	SEM for Different Annealing Temperatures	50
4.1.3	UV-vis DRS Spectra for Different Annealing Temperatures	54
4.1.4	Photoluminescence Emission Spectra for Different Annealing Temperatures	56
4.1.5	DSC and TGA for Synthesized Non-annealed ZnO	57
4.1.6	Photocatalytic Activity Measurement for Different Annealing Temperatures	58
4.1.7	Selection of Annealing Temperature.....	59
4.2	OPTIMIZATION OF CHELATING AGENT	60

4.2.1. XRD for Different Chelating Agent Ratios.....	60
4.2.2. SEM for Different Chelating Agent Ratios.....	61
4.3 EFFECT OF RARE-EARTH DOPANTS	63
4.3.1 XRD for Doped ZnO Nanoparticles.....	63
4.3.2 SEM for Doped ZnO Nanoparticles.....	71
4.3.3 UV-vis DRS spectra for Doped ZnO Nanoparticles	76
4.3.4 Photoluminescence Emission Spectra for Doped ZnO Nanoparticles	81
4.3.6 Photocatalytic Activity Measurement of Doped ZnO Nanoparticles.....	82
4.3.6.1 Degradation Efficiency of Doped ZnO Nanoparticles.....	82
4.3.6.2 Degradation Kinetics of Doped ZnO Nanoparticles	86
4.3.6.3 Degradation Mechanism of Doped ZnO Nanoparticles.....	88
5 CONCLUSION.....	90
6 SCOPE FOR FUTURE INVESTIGATIONS.....	92
REFERENCES.....	93

LIST OF FIGURES

Figure 2.1	Schematic representation of semiconductor photocatalytic mechanism	5
Figure 2.2	Schematic representation of oxidation mechanism	6
Figure 2.3	Schematic representation of reduction mechanism	7
Figure 2.4	Heterogeneous photocatalytic oxidation steps	9
Figure 2.5	Degradation of organic pollutants by ZnO in the presence of solar light	9
Figure 2.6	Stick and ball representation of ZnO crystal structures: (A) Cubic Rocksalt, (B) Cubic Zincblende and (C) Hexagonal Wurtzite	13
Figure 2.7	Tetrahedrally coordinated hexagonal wurtzite structure of ZnO	13
Figure 2.8	Representation of band gap variation with particle size.....	16
Figure 2.9	Representation of surface area to volume ratio	17
Figure 2.10	Surface charges for ZnO nanoparticles as a function of pH of reaction solution.	19
Figure 2.11	Overview showing two examples of synthesis by the sol-gel method: (a) films from a colloidal sol; (b) powder from a colloidal sol transformed into a gel.....	26
Figure 2.12	Overview of synthesis by the hydrothermal method.....	28
Figure 3.1	XRD Machine.....	38
Figure 3.2	FESEM	39
Figure 3.3	STA/TG-DSC	40
Figure 3.4	UV-vis Spectroscopy.....	40
Figure 3.5	Spectro-fluorophotometer.....	41
Figure 3.6	Photocatalytic activity measurement setup: (a) dark box with UV light, (b)centrifuge machine, (c) pH meter, (d) UV-vis spectroscopy.....	42
Figure 3.7	Photocatalytic activity measurement setup with Xenon lump housing E10180 ..	43
Figure 3.8	Functional group present in dyes: (a) Rhodamine B and (b) Methylene Blue.....	43
Figure 4.1	XRD patterns showing crystalline structure of ZnO nanoparticles annealed at different temperatures.....	46
Figure 4.2	XRD patterns showing increasing crystallinity of ZnO nanoparticles with increasing annealing temperature (normalized XRD patterns)	46
Figure 4.3	Variation of activation energy for ZnO nanoparticles annealed at different temperature change.....	50

Figure 4.4	Morphology of ZnO nanoparticles (at 30,000X and 1,00,000X) at different annealing temperatures: (a) 400 ⁰ C, (b) 500 ⁰ C, (c) 600 ⁰ C, (d) 700 ⁰ C	52
Figure 4.5	Elemental analysis and particle size distribution of ZnO nanoparticles at different annealing temperatures: (a) 400 ⁰ C, (b) 500 ⁰ C, (c) 600 ⁰ C, (d) 700 ⁰ C	53
Figure 4.6	Progressive increase in reflectance with increasing annealing temperature	54
Figure 4.7	Progressive decrease in band gap with increasing annealing temperature: (a) 400 ⁰ C, (b) 500 ⁰ C, (c) 600 ⁰ C, (d) 700 ⁰ C	55
Figure 4.8	PL emission spectra showing (a) near band gap emission and (b) orange band emission at different annealing temperatures	56
Figure 4.9	Combined DSC and TGA plot showing exothermic and endothermic reactions along with weight changes during heating	57
Figure 4.10	Variation of the absorption spectra for MB solution in the presence of ZnO annealed at (a) 500 ⁰ C and (b) 600 ⁰ C under UV light at different time intervals.	58
Figure 4.11	XRD patterns showing crystalline structure of ZnO nanoparticles at different precursor to citric acid ratios	60
Figure 4.12	XRD patterns showing increasing crystallinity of ZnO nanoparticles at different precursor to citric acid ratios (normalized XRD patterns)	61
Figure 4.13	Morphology of ZnO nanoparticles (at 30,000X and 1,00,000X) at different precursor to citric acid ratios: (a) 1:1 and (b) 1:2	62
Figure 4.14	Particle size distribution of ZnO nanoparticles at different precursor to citric acid ratios: (a) 1:1 and (b) 1:2	62
Figure 4.15	XRD patterns showing crystalline structure of ZnO nanoparticles at different Ho concentrations.....	64
Figure 4.16	XRD patterns showing crystalline structure of ZnO nanoparticles at different Sm concentrations.....	65
Figure 4.17	XRD patterns showing decreasing crystallinity of ZnO nanoparticles at different Ho concentrations (normalized XRD patterns)	65
Figure 4.18	XRD patterns showing decreasing crystallinity of ZnO nanoparticles at different Sm concentrations (normalized XRD patterns).....	66
Figure 4.19	XRD patterns showing peak shift of (002) plane of ZnO nanoparticles at different Ho concentrations (normalized XRD patterns)	66
Figure 4.20	XRD patterns showing peak shift of (002) plane of ZnO nanoparticles at different Sm concentrations (normalized XRD patterns).....	67

Figure 4.21 Morphology of ZnO nanoparticles (at 30,000X and 1,00,000X) at different Ho Concentrations: (a) pristine, (b) 1 mol% (c) 3 mol% and (d) 5 mol%	72
Figure 4.22 Morphology of ZnO nanoparticles (at 30,000X and 1,00,000X) at different Sm Concentrations: (a) pristine, (b) 1 mol% (c) 3 mol% and (d) 5 mol%	73
Figure 4.23 Elemental analysis and particle size distribution of ZnO nanoparticles at different Ho concentrations: (a) pristine, (b) 1 mol%, (c) 3 mol% and (d) 5 mol%	74
Figure 4.24 Elemental analysis and particle size distribution of ZnO nanoparticles at different Sm concentrations: (a) pristine, (b) 1 mol%, (c) 3 mol% and (d) 5 mol%.....	75
Figure 4.25 Variation in band gap with increasing Ho concentration: (a) pristine, (b) 1 mol%, (c) 3 mol% and (d) 5 mol%	77
Figure 4.26 Variation in band gap with increasing Sm concentration: (a) pristine, (b) 1 mol%, (c) 3 mol% and (d) 5 mol%	78
Figure 4.27 Variation in reflectance with increasing Ho concentration	79
Figure 4.28 Variation in reflectance with increasing Sm concentration.....	79
Figure 4.29 Variation in absorbance with increasing Ho concentration.....	80
Figure 4.30 Variation in absorbance with increasing Sm concentration	80
Figure 4.31 PL emission spectra showing (a) near band gap emission and (b) orange band emission at different Ho concentrations	81
Figure 4.32 PL emission spectra showing (a) near band gap emission and (b) orange band emission at different Sm concentrations	82
Figure 4.33 Variation of the absorption spectra for Rh B solution in the presence of (a) pristine, (b) 3 mol% Ho doped and (c) 3 mol% Sm doped ZnO nanoparticles under UV light at different time intervals	83
Figure 4.34 Variation in remaining concentration of dye among pristine, 3 mol% Ho and 3 mol% Sm doped ZnO nanoparticles.....	84
Figure 4.35 Variation in degradation efficiency among pristine, 3 mol% Ho and 3 mol% Sm doped ZnO nanoparticles.....	85
Figure 4.36 PL emission spectra comparing recombination rate among pristine, 3 mol% Ho and 3 mol% Sm doped ZnO	85
Figure 4. 37 Visual inspection of progressive degradation of Rh B solution in the presence of 3 mol% Ho doped ZnO nanoparticles under UV light at different time intervals	86
Figure 4.38 Variation in degradation kinetics among pristine, 3 mol% Ho and 3 mol% Sm doped ZnO nanoparticles	87
Figure 4.39 Possible photocatalytic mechanism of Ho- and Sm-doped ZnO nanoparticles ...	89

LIST OF TABLES

Table 2.1 Important physical properties of ZnO.....	11
Table 3.1 Experimental variables and raw materials for different compositions	37
Table 4.1 XRD data analysis for annealing temperature 400 ⁰ C.....	47
Table 4.2 XRD data analysis for annealing temperature 500 ⁰ C.....	47
Table 4.3 XRD data analysis for annealing temperature 600 ⁰ C.....	48
Table 4.4 XRD data analysis for annealing temperature 700 ⁰ C.....	48
Table 4.5 Rietveld analysis for ZnO nanoparticles annealed at different temperatures	49
Table 4.6 XRD data analysis 1 mol% Ho-doping.....	67
Table 4.7 XRD data analysis 3 mol% Ho-doping.....	68
Table 4.8 XRD data analysis 5 mol% Ho-doping.....	68
Table 4.9 XRD data analysis 1 mol% Sm-doping	69
Table 4.10 XRD data analysis 3 mol% Sm-doping	69
Table 4.11 XRD data analysis 5 mol% Sm-doping	70
Table 4.12 Rietveld analysis for Ho-doped ZnO nanoparticles.....	70
Table 4.13 Rietveld analysis for Sm-doped ZnO nanoparticles	70
Table 4.14 Kinetics parameters for pristine and doped ZnO	87

1 INTRODUCTION

1.1 BACKGROUND AND RESEARCH MOTIVATION

In recent years, implementation of water reclamation and reuse is gaining attention rapidly world-wide due to the water scarcity occurred as a result of climate change and poor water resource management (i.e. limited access to clean water resources and as water demand exceeds the available resources) [1-2]. Access to clean water is becoming an ever increasing problem in the expanding global economy and high population countries. One of the attractive solutions in response to water issues is implementation of wastewater reclamation and reuse projects to ensure a sustainable water development and management. However, concerns still arise from the fact that persistent organic pollutants (POPs) could still be present in treated water. POPs are carbon-based chemical substances that are resistant to environment degradation and have been continuously released into the environment. POPs can cause severe harm to human beings and wildlife because of their poor biodegradability and carcinogenic characteristics in nature [3]. Solar photocatalysis is an effective solution for this problem, which has received increasing attention due to its great potential as a green and eco-friendly process for the elimination of POPs to increase the security of clean water. Photocatalyst has the capability of absorbing light and producing electron-hole pairs that enable chemical transformations of the reaction participants and regenerate its chemical composition after each cycle of such interactions. Semiconductor oxides such as TiO_2 , ZnO , Fe_2O_3 etc. act as heterogeneous photocatalyst [4-6].

Zinc Oxide (ZnO) nanoparticle, an n-type semiconductor, is emerging as a promising material in the field of photonics, optoelectronics, spintronics, gas sensors and photocatalysts applications due to its wide band gap of 3.37 eV and large exciton binding energy of 60 MeV. Additionally, its low cost, non-toxic nature, high physical and chemical stability, higher absorption efficiency across a large fraction of the solar spectrum, give ZnO nanoparticles an edge over other semiconductor photocatalysts [7-8].

High photocatalytic activity of ZnO photocatalyst is retarded due to the quick recombination of photo-generated charge carriers [9-10]. To improve the photocatalysis efficiency, it is essential to delay the recombination of the charge carriers. Enhancement of the separation of

charge carriers in ZnO nanoparticles can be done by modifying crystallinity and morphology of nanoparticles. Moreover, as ZnO nanoparticles have a band gap around 3.37 eV, band gap tuning is important to improve solar energy conversion performance of ZnO nanoparticles.

Doping with rare-earth elements provide an effective mean to enhance the photocatalytic activity of ZnO nanoparticles [11]. To the best of the knowledge, no work has been reported so far for doping Holmium (Ho) and Samarium (Sm) in ZnO nanoparticles by modified sol-gel route. Modified sol-gel route has advantage over other process due its low cost, low processing temperatures, high chemical homogeneity along with the possibility of controlling the size and morphology of particles. Moreover, the photocatalytic activity of Ho- and Sm-doped ZnO nanoparticles have not been investigated to its full extent. Herein motivated by the above concerns, Ho- and Sm-doped ZnO nanoparticles prepared by modified sol-gel method and their structural, optical and photocatalytic properties were investigated in detail.

1.2 OBJECTIVE OF THE PRESENT STUDY

The specific aim of this work was to focus on the synthesis of Ho- and Sm-doped ZnO nanoparticles with a concentration on improving the photocatalytic activity. Keeping this in mind, there were three principal objectives of this work. These were:

- Optimizing the process parameters for synthesizing ZnO nanoparticles by modified sol-gel method
- Doping rare earth elements, Holmium (Ho) and Samarium (Sm) in ZnO nanoparticles at optimized condition
- Studying the effect of doping on structural modification of ZnO nanoparticles and investigating its photocatalytic activity

The expected outcome of this research was having rare earth element (Ho & Sm) doped ZnO nanoparticles exhibiting strong photocatalytic activity. Moreover, this study would allow to understand the fundamental effect of rare earth element doping on the structure and photocatalytic activity of ZnO nanoparticles.

2 LITERATURE REVIEW

2.1 PHOTOCATALYSIS

Photocatalysis is the amalgamation of photochemistry and catalysis. The word “photocatalysis” is derived from the Greek language and composed of two parts:

- The prefix photo means light
- Catalysis is the process where a substance involves in altering the rate of a chemical transformation of the reactants without being altered in the end. The substance which is known to be a catalyst increases the rate of the reaction by reducing the activation energy.

Hence, photocatalysis is a process where light and catalysts are concurrently used to support or speed up a chemical reaction. So, photocatalysis can be defined as catalysis driven acceleration of a light-induced reaction.

Photocatalysis is an extraordinary method which can be used for various purposes like degradation of various organic pollutants in wastewater, production of hydrogen, purification of air and antibacterial activity [12-13]. Recently, the photocatalytic process is attaining more concentration in the field of wastewater treatment to obtain complete mineralization of the pollutant achieved under mild conditions of temperature and pressure. The rate of photo mineralization of an organic compound by photocatalysis method primarily depends on the parameters i.e. structure, shape, size, and surface area of the catalyst, reaction temperature, pH, light intensity, amount of catalyst and concentration of wastewater [14-17]. Photocatalyst is classified into two categories: homogeneous and heterogeneous process [4-6].

2.1.1 Homogeneous Photocatalysis

In homogeneous photocatalysis, the reactants and the photocatalyst exist in the same phase. Homogeneous photocatalytic processes mostly are used with metal complexes as catalysts (transition metals complexes like iron, copper, chromium, etc.). In this process, under the photon and thermal condition, the higher oxidation state of metal ion complexes generate hydroxyl radicals. These hydroxyl radicals react with organic matter which leads destruction

of toxic matters. Homogeneous photocatalysis employs Fenton's reagent, which is a mixture of hydrogen peroxide and an Fe^{2+} salt to produce hydroxyl radicals under UV irradiation at wavelengths above 300 nm [15].

2.1.2 Heterogeneous Photocatalysis

Heterogeneous catalysis has the catalyst in a different phase from the reactants. Semiconducting materials (TiO_2 , ZnO , SnO_2 , and CeO_2) mainly act as heterogeneous photocatalysts because of its favorable combination of electronic structures, which is characterized by a filled valence band and an empty conduction band, light absorption properties, charge transport characteristics and excited states lifetime. The ultimate goal of heterogeneous photocatalyst design is to start reactions between the excited electrons with oxidants to produce reduced products, and/or reactions between the generated holes with reductants to produce oxidized products. Due to the generation of positive holes and electrons, oxidation-reduction reactions take place at the surface of semiconductors. Heterogeneous photocatalysis is a technically gifted method which can be used for the degradation of various organic pollutants in wastewater [18-19].

This process has several advantages over the homogenous processes such as

- Complete mineralization
- No waste disposal problem
- Low cost
- Necessity of mild temperature and pressure conditions

2.2 PHOTOCATALYTIC MECHANISM

Photocatalytic reaction primarily depends on wavelength or light (photon) energy and the catalyst. In general, semiconducting materials are used as a catalyst which performs as sensitizers for the irradiation of light stimulated redox process due to their electronic structure, which is characterized by a filled valence band and a vacant conduction band. Figure 2.1 shows the schematic representation of semiconductor photocatalytic mechanism.

The fundamental steps [19-20] in the process of semiconductor photocatalysis are as follows:

- When the light energy in terms of photons fall on the surface of a semiconductor and if the energy of incident ray is equivalent or more than the bandgap energy of the semiconductor, the valence band electrons are agitated and move to the conduction band of the semiconductor.
- Holes would be left in the valence band of the semiconductor. These holes in the valence band can oxidize water molecules to generate hydroxyl radicals. The hydroxyl radicals have strong oxidizing power responsible for the degradation of pollutants.
- The conduction band electrons react with dissolved oxygen species to form superoxide ions. These electrons induce the redox reactions.

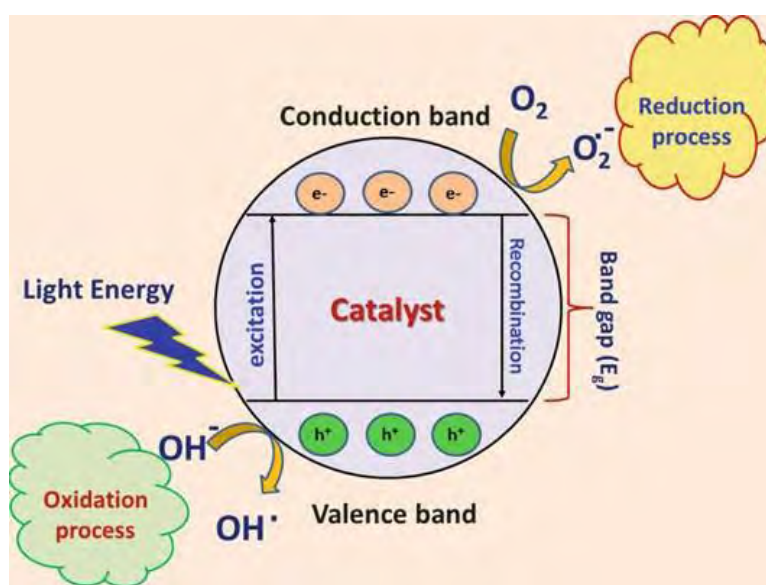


Figure 2.1 Schematic representation of semiconductor photocatalytic mechanism

These holes and electrons could undergo successive oxidation and reduction reactions with any species, which might be adsorbed on the surface of the semiconductor to give the necessary products.

2.2.1 Oxidation Mechanism

The photocatalyst surface contains water, which is mentioned as “absorbed water.” This water is oxidized by positive holes created in the valence band due to the electrons shift to the

conduction band as a result of light irradiation, thus making way for the formation of hydroxyl ($\text{OH}\cdot$) radicals, which have strong oxidative decomposing power. Afterward, these hydroxyl radicals react with organic matter present in the dyes. If oxygen is present when this process happens, the intermediate radicals in the organic compounds along with the oxygen molecules can experience radical chain reactions and consume oxygen in some cases. In such a case, the organic matter finally decomposes ultimately becoming carbon dioxide and water. Under such circumstances, organic compounds can react straightly with the positive holes, resulting in oxidative decomposition [20]. The complete oxidation processes are shown in Figure 2.2.

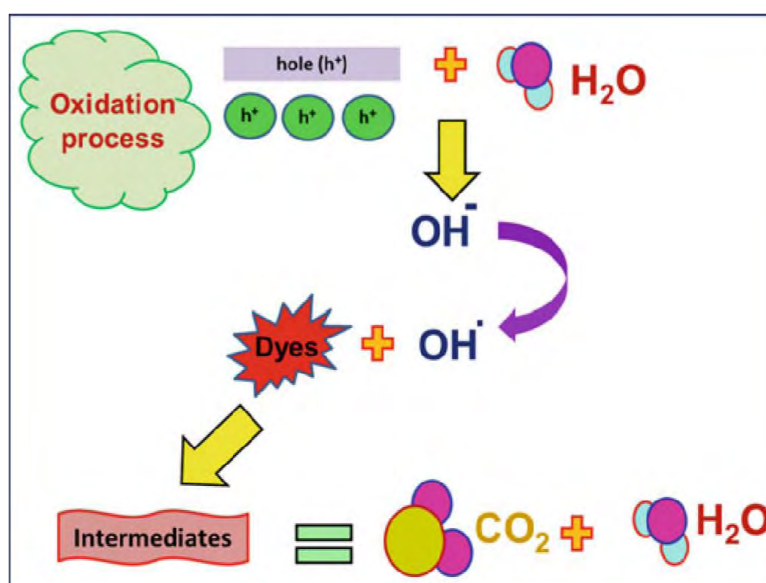


Figure 2.2 Schematic representation of oxidation mechanism

2.2.2 Reduction Mechanism

Figure 2.3 represents the reduction process, the reduction of oxygen contained in the air occurs as a pairing reaction. Reduction of oxygen takes place as an alternative to hydrogen generation due to the fact that oxygen is an easily reducible substance. The conduction band electrons react with dissolved oxygen species to form superoxide anions. These superoxide anions get attached to the intermediate products in the oxidative reaction, forming peroxide or changing to hydrogen peroxide and then to water. The reduction is likely to occur more easily in organic matter than in water. Therefore, the higher concentration of organic matter tends to increase the number of positive holes. This reduces the carrier recombination and enhances the photocatalytic activity [20].

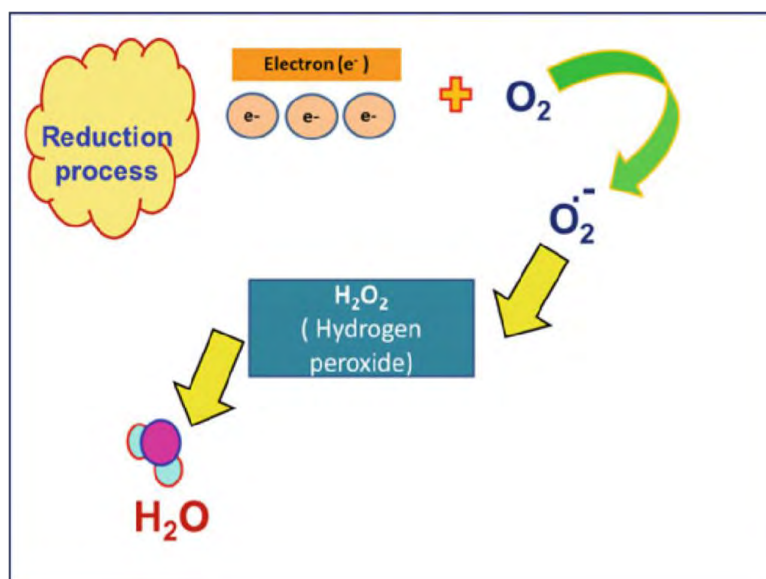


Figure 2.3 Schematic representation of reduction mechanism

2.3 ADVANTAGES OF PHOTOCATALYSIS FOR DYE DEGRADATION

The advantages of this photocatalytic technology are as follows:

- Photocatalysis offers a good replacement for the energy-intensive conventional treatment methods (adsorption on activated carbon, ultrafiltration, reverse osmosis, coagulation by chemical agents, ion exchange on synthetic adsorbent resins) with the capacity for using renewable and pollution-free solar energy.
- Photocatalysis leads to the formation of harmless products, unlike conventional treatment measures, which transfer pollutants from one phase to another.
- The photocatalytic process can be used in the destruction of a variety of hazardous compounds in different wastewater streams.
- The reaction conditions for photocatalysis are mild, the reaction time is modest and a lesser chemical input is required.
- Minimal of secondary waste generation
- It can be applied to hydrogen generation, gaseous phase, and aqueous treatments as well for solid (soil) phase treatments to some extent.

2.4 CHARACTERISTICS OF PHOTOCATALYSTS

An excellent semiconductor photocatalyst should possess

- Wide band gap: About 1.1-3.4 eV
- Ability to utilize visible and/or near-UV light
- Photo-stability: Resistant to self-degradation under radiation
- Biological and chemical inertness
- Valence band energy (eV): Lower than oxidation potential of oxygen
- Conduction band energy (eV): Higher than reduction potential of hydrogen
- Capability of water splitting
- Ability to transport electrons to the surface
- Inexpensive and non-toxic

2.5 PHOTOCATALYTIC ACTIVITY ENHANCEMENT

Enhanced photocatalytic activity can be achieved by

- Improve interfacial charge transfer
- Improve the charge separation
- Inhibition of charge carrier recombination

Modify the surface of the particles is an essential step to prevent the electron-hole recombination via metal and nonmetal doping, coupling with various metal and metal oxides and surface sensitization by the polymer.

2.6 ZnO AS POTENTIAL PHOTOCATALYST

ZnO is an n-type of semiconductor having a broad direct band gap width (3.37 eV), large excitation binding energy (60 meV) and deep violet/borderline ultraviolet (UV) absorption at room temperature [21]. It is an excellent semiconductor oxide that possesses favorable excellent electrical, mechanical and optical properties, similar to TiO₂. In addition, ZnO not only has good photocatalytic activity, but also has antifouling and antibacterial properties.

Furthermore, the production cost of ZnO is up to 75% lower than that of TiO₂ and Al₂O₃ nanoparticles [8].

The heterogeneous photocatalytic mechanism for ZnO nanoparticles can be explained as shown in Figure 2.4 [10]. The steps of photocatalysis are

1. Organic pollutants diffuse from liquid phase to the surface of ZnO NPs
2. Adsorption of organic pollutants on ZnO surface
3. Oxidation and reduction reactions in the adsorbed phase
4. Desorption of the dye degradation products
5. Removal of products from the interface region

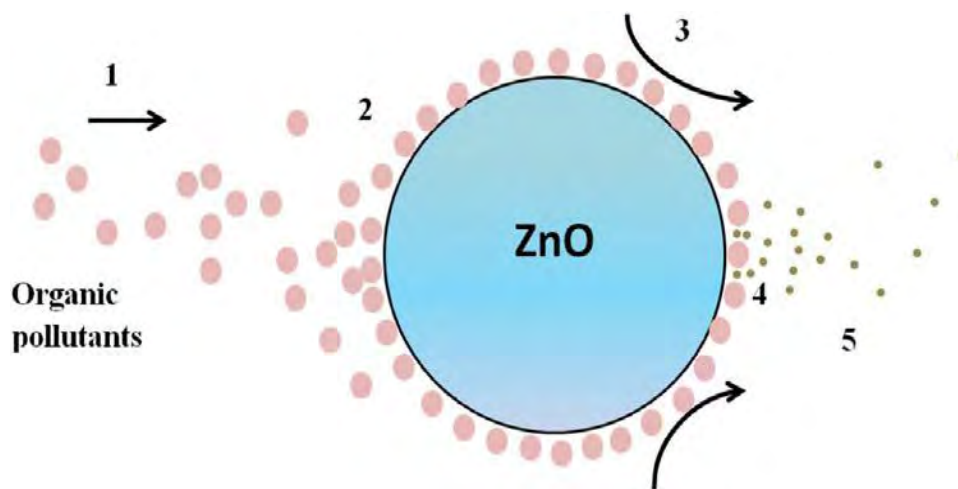


Figure 2.4 Heterogeneous photocatalytic oxidation steps

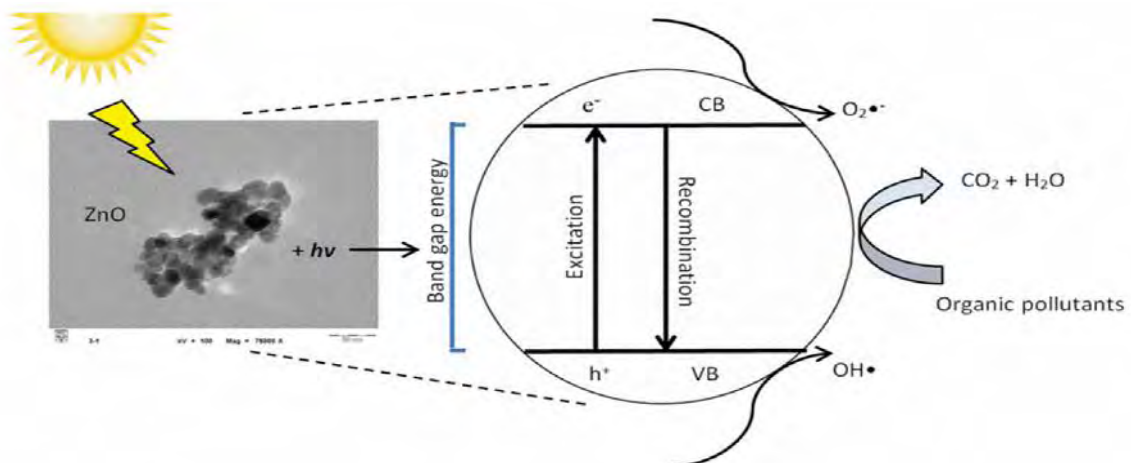


Figure 2.5 Degradation of organic pollutants by ZnO in the presence of solar light

Figure 2.5 illustrates the redox reaction occurring during photocatalysis. When ZnO is photo-induced by solar light with photonic energy ($h\nu$) equal to or greater than the excitation energy (E_g), e^- from the filled valence band (vb) are promoted to an empty conduction band (cb). This photo-induced process produces electron-hole (e^-/h^+) pairs as shown in Eq. (1). The electron-hole pairs can migrate to the ZnO surface and be involved in redox reactions as shown in Eqs. (2)- (4), wherein the h^+ reacts with water and hydroxide ions to produce hydroxyl radicals while e^- reacts with oxygen to produce superoxide radical anions, which reacts with H^+ to generate perhydroxyl free radical and then hydrogen peroxide (Eqs. (5)- (6)). Hydrogen peroxide will then react with superoxide radicals to form hydroxyl radicals (Eqs. (7)- (8)). Then, the resulting hydroxyl radicals, which are powerful oxidizing agents, will attack the pollutants adsorbed on the surface of ZnO to rapidly produce intermediate compounds (Eq. (9)). Intermediates will eventually be converted to green compounds such as CO_2 , H_2O and mineral acids as shown in Eq. (10) [22,23]. The mechanism of photodegradation of organic compounds in the presence of solar radiation via redox reaction can be summarized as follows:



2.7 PROPERTIES OF ZnO

ZnO is a member of II-VI semiconducting compounds and occurs naturally as the mineral zincite. It is a hexagonal wurtzite type crystal exhibiting anisotropy [24]. ZnO is a well-known n-type semiconductor having piezoelectric, dielectric properties with a wide direct bandgap of 3.37 eV at room temperature (300 K) and a large exciton binding energy of 60 meV, which is 2.4 times the effective thermal energy ($k_B T = 25 \text{ meV}$) at room temperature [25-26]. ZnO is

considered a good candidate for TCO electrodes in solar cells because it is transparent to the visible light (>80%). It is also considered a prime candidate for UV and blue light emitting devices such as blue LED and LASERs due to its large exciton binding energy. Due to large exciton binding energy, the excitons remain dominant in optical processes even at room temperature. Its resistance to radiation damages also makes it useful for space applications. Since ZnO is the hardest of the II-VI semiconductors due to the higher melting point of 2248 K and large cohesive energy of 1.89 eV, its performance is not degraded as easily as the other compounds through the appearance of defects. Since Zinc, the main constituent is cheap, non-toxic and abundant, ZnO has become commercially viable [27]. Some of the important properties of ZnO are summarized in Table 2.1 [28].

Table 2.1 Important physical properties of ZnO

Physical Parameters	Values
Crystal Structure	Rock salt, Zinc blende and Wurtzite
Molecular Weight	81.37 g mol ⁻¹
Color	Pure microcrystalline zinc oxide is white Single crystal zinc oxide is colorless
Bond Length	1.977 μm
Bandgap (T = 300 K)	3.37 eV (direct)
Excitation Binding Energy	60 meV
Electron Mobility	2.5-300(cm ² Vs ⁻¹) (Bulk ZnO), 1000(cm ² Vs ⁻¹) (Single nanowire)
Thermal Conductivity	0.6 W cm ⁻¹ C ⁻¹
Coefficient of Thermal Expansion	4×10 ⁻⁶ /°C
Relative Density	5.606 g/cm ³
Refractive Index for Wurtzite	2.0041
Heat Capacity: C _p (25 °C)	9.62 cal/deg/mol
Electron Effective Mass	0.26 m _e
Relative Dielectric Constant	8.5
Lattice Constants (T = 300 K)	
a	0.32495 nm
c	0.52069 nm
c/a	1.602
Melting Point	1975 °C
Minimum Pressure at Melting Point	7.82 atm
Boiling Point	2360 °C
Electron Diffusion Coefficient	5.2 cm ² s ⁻¹ (Bulk ZnO), 1.7 × 10 ⁻⁷ cm ² s ⁻¹ (Particulate Film)

2.7.1 Crystal Structure of ZnO

Zinc oxide crystallizes in three forms: hexagonal Wurtzite (*B4*), cubic zincblende (*B3*) and the rarely observed cubic rocksalt (*B1*), as shown in Figure 2.6 [29]. The wurtzite structure is most stable and thus most common at ambient conditions. The zincblende form can be stabilized by growing ZnO on substrates with cubic lattice structure. In both cases, the zinc and oxide are tetrahedral. The rocksalt NaCl-type structure is only observed at relatively high pressures ~ 10 GPa. The hexagonal and zincblende ZnO lattices have no inversion symmetry. This and other lattice symmetry properties result in piezoelectricity of the hexagonal and zinc blende ZnO, and in pyro-electricity of hexagonal ZnO [30].

At ambient pressure and temperature, ZnO crystallizes in the wurtzite structure, as shown in Figure 2.7. This is a hexagonal lattice, belonging to the space group $P6_{3mc}$ or C_{6v}^4 with lattice parameters $a = 0.32495$ and $c = 0.52069$ nm and is characterized by two interconnecting sublattices of Zn^{2+} and O^{2-} , such that each Zn ion is surrounded by tetrahedra of O ions, and vice-versa. This tetrahedral coordination gives rise to polar symmetry along the hexagonal axis. This polarity is responsible for a number of the properties of ZnO including its piezoelectricity and spontaneous polarization, and is also a key factor in crystal growth, etching and defect generation [31].

The four most common face terminations of wurtzite ZnO are the polar Zn terminated (0001) and O terminated (000 $\bar{1}$) faces (c-axis oriented), and the non-polar (1120) (*a*-axis) and (1010) faces both of which contain an equal number of Zn and O atoms. The polar faces are known to possess different chemical and physical properties and the O-terminated face possesses a slightly different electronic structure compared to the other three faces. Along the c-axis, the positively charged Zn-(0001) polar surface and negative charged O-(000 $\bar{1}$) polar surface are the strongest polarity surfaces. The polar surfaces contribute to the variety of ZnO nanostructures by surface reconstruction to maintain a stable structure. When a stress force is applied, the non-central symmetric structure will lead to the separation of the central point of positive charges and that of negative charges, resulting in a polarization [32-33]. Additionally, the polar surfaces and the (1010) surface are found to be stable, however the (1120) face is less stable and generally has a higher level of surface roughness than its counterparts. The (0001) plane is also the basal plane. Apart

from causing the inherent polarity in the ZnO crystal, the tetrahedral coordination of this compound is also a common indicator of sp^3 covalent bonding. However, the Zn–O bond also possesses very strong ionic character, and thus ZnO lies on the borderline between being classed as a covalent and ionic compound, with an ionicity of $f_i = 0.616$ on the Phillips ionicity scale [34].

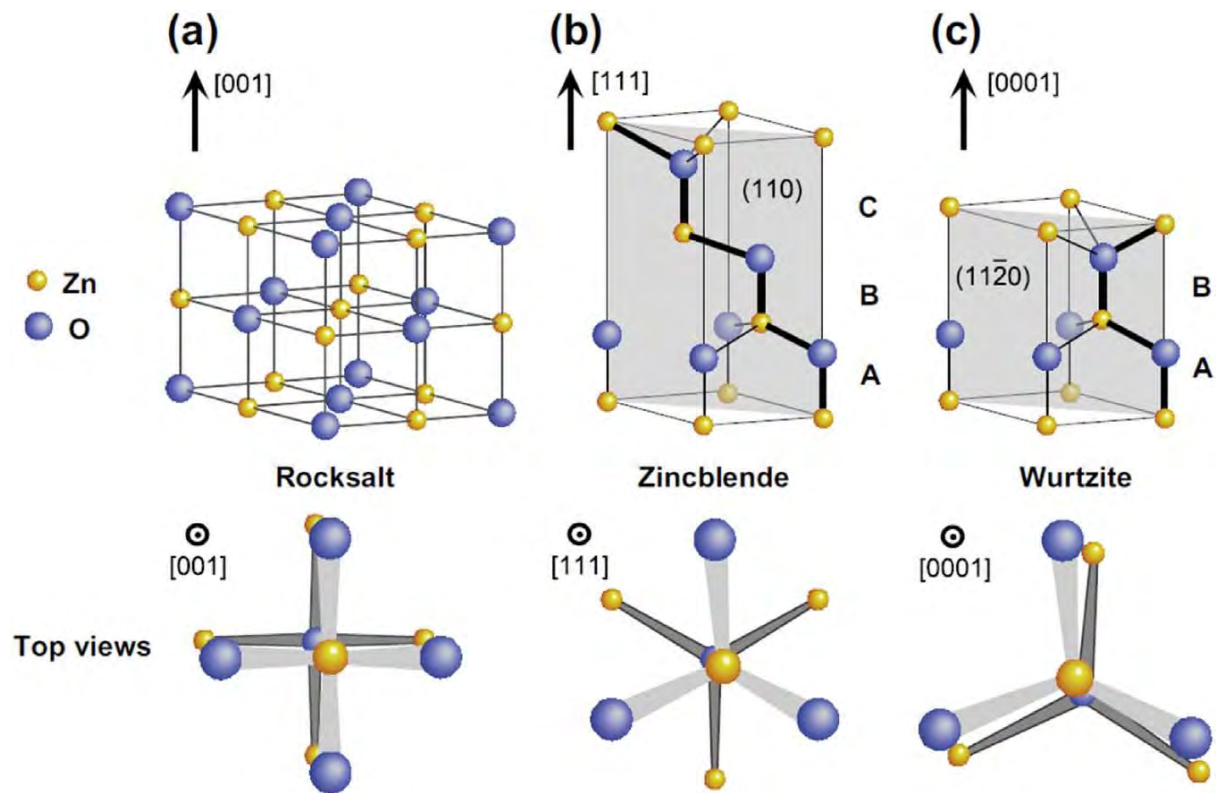


Figure 2.6 Stick and ball representation of ZnO crystal structures: (A) Cubic Rocksalt, (B) Cubic Zincblende and (C) Hexagonal Wurtzite

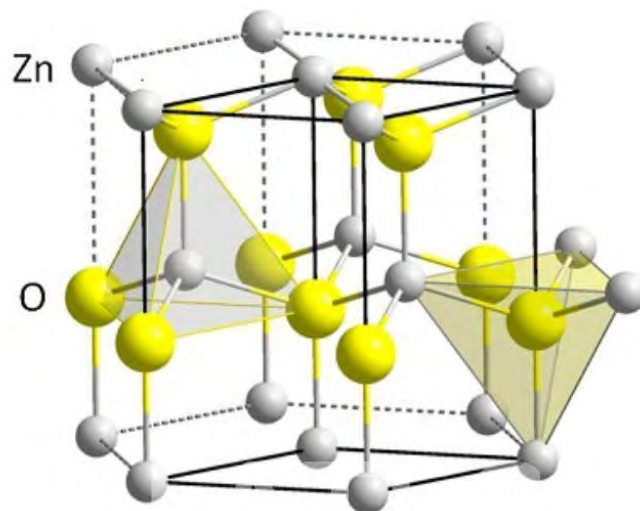


Figure 2.7 Tetrahedrally coordinated hexagonal wurtzite structure of ZnO

2.7.2 Electrical Properties

The fundamental study of the electrical properties of ZnO nanostructures is crucial for developing their future applications in nanoelectronics. ZnO has a quite large band gap of 3.37 eV at room temperature. The advantages of a large band gap include higher values of breakdown voltages, sustaining large electric fields, high-temperature and high-power operations. ZnO has n-type character, in the absence of doping. Non-stoichiometry is usually the origin of n-type character. Due to defects such as oxygen vacancies and zinc interstitials, ZnO nanoparticles are reportedly show n-type semiconductor behavior. The main impediment of ZnO for wide-ranging applications in electronics and photonics rests with the difficulty of p-type doping. Successful p-type doping for ZnO nanostructures will greatly enhance their future applications in nanoscale electronics and optoelectronics. P-type and n-type ZnO nanowires can serve as p-n junction diodes and light emitting diodes (LED) [35].

2.7.3 Optical Properties

Zinc oxide is generally transparent to visible light but strongly absorbs ultra violet light below 3655 Å. The absorption is typically stronger than other white pigments. In the region of visible wavelengths, regular zinc oxide appears white. The band gap energy (between valence and conducting bands) is 3.37 eV, this corresponds to the energy of 3655 Å photons. Under ultra violet light zinc oxide is photoconductive. The combination of optical and semiconductor properties make doped zinc oxide a contender for new generations of devices. The larger exciton binding energy, which will allow for room temperature devices operating with higher efficiency and lower power threshold for lasing by optical pumping. Solar cells require a transparent conductive coating, indium tin oxide and zinc oxide (doped) are the best materials [36].

Intrinsic optical properties of ZnO nanostructures are being intensively studied for implementing photonic devices. Photoluminescence (PL) spectra of ZnO nanostructures have been extensively reported. Excitonic emissions have been observed from the photoluminescence spectra of ZnO nanorods. It is shown that quantum size confinement can significantly enhance the exciton binding energy [37]. Strong emission peak at 380 nm due to band-to-band transition and green-yellow emission band related to oxygen vacancy are

observed. PL spectra show that ZnO nanoparticle is a promising material for UV emission, while its UV lasing property is of more significance and interest. Due to its near-cylindrical geometry and large refractive index (~ 2.0), ZnO nanowire/nanorod is a natural candidate for optical waveguide. The additional advantages of ZnO lasers are that the excitonic recombination lowers the threshold of lasing, and quantum confinement yields a substantial density of states at the band edges and enhances radiative efficiency.

UV photoconductivity of ZnO is governed by surface-related and bulk-related processes. The surface-related process is primarily governed by the adsorption and desorption of the chemisorbed oxygen at the surface of the ZnO, which is exploited for gas sensing application. This process becomes prominent in nanocrystalline films, where the surface area is large. In the bulk-related process, oxygen molecules in the grain boundaries contribute to photoconductivity. The bulk-related process is however considered to be faster in comparison to the surface-related process. For UV-detection, the fast component, due to the generation of photo carriers and their radiative and non-radiative recombination through local centres, is of greater importance. Inherent defect centres, such as oxygen vacancies and zinc interstitials are believed to be responsible for visible photoluminescence in ZnO [38].

2.8 FACTORS AFFECTING PHOTOCATALYTIC EFFICIENCY OF ZnO

2.8.1 Band Gap

Due to quantum size effects (QSE), band gap energy increases with decreasing particle size as shown in Figure 2.8, which explains why the nanoparticles have wider band gap than the corresponding bulk matter. In bulk ZnO the energy levels are closely spaced and thus form quasi-continuous bands. On moving to the nano-regime the energy level separation increases and discrete energy levels are formed. However, quantum confinement effects are observable at sizes below 10 nm for most semiconductor materials. Absorption spectrum shows a shift towards lower wavelength (blue region of UV region) for ZnO nanoparticles and is one of the most important aspects in photocatalytic reactions [39].

The energy gap between valence and conduction band is defined as the band gap (E_g). The photocatalytic activity of ZnO nanoparticles largely depends upon the band gap value being affected by its surface and structural properties, particle size distribution and porosity. Average crystal size and specific surface area of ZnO heterogeneous photocatalysis is directly related to the efficiency of ZnO as photocatalyst. The optical band gap energy (E_g) of the ZnO nanomaterials can be calculated by using Tauc's equation which exhibits the relationship between absorption coefficient and the incident photon energy of semiconductors [40]. The Tauc's Eq. (11) is as follows:

$$(\alpha h\nu) = A (h\nu - E_g)^n \tag{11}$$

Where, α is the absorption coefficient, $h\nu$ is the energy of the photon, A is a constant, E_g is the optical band gap and n is a value that depends on the nature of the electronic transition responsible for the absorption.

Band gap can also be calculated from diffuse reflectance spectra by using Kubelka-Muck (K-M) transform. The K-M transform of the measured spectroscopic observable is approximately proportional to the absorption coefficient and hence is approximately proportional to the concentration [41].

$$\frac{K}{S} = \frac{(1 - R_\infty)^2}{2R_\infty} \tag{12}$$

Where k is the absorption coefficient of the sample and S is the scattering co-efficient.

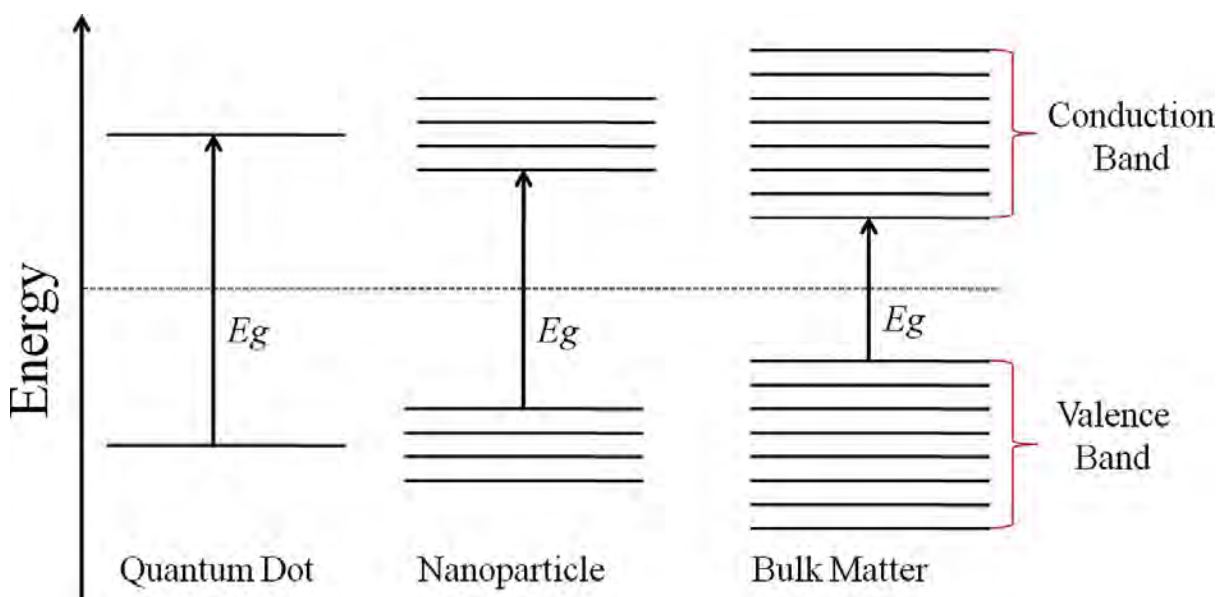


Figure 2.8 Representation of band gap variation with particle size

2.8.2 Annealing Temperature

The most important factors affected by the particle size of ZnO nanomaterials are the surface to volume ratio, band gap shift and consequently the charge separation between free electrons (e^-_{cb}) in the empty conduction band and positive holes (h^+_{vb}) in the valence band [42]. As the particle size decreases the surface area increases, thereby increasing the surface area to volume ratio as shown in Figure 2.9. Since the process of photo-degradation occurs at the surface of a catalytic semiconductor, increasing the surface area to volume ratio, by decreasing the particle size is expected to enhance the photocatalytic activity. Moreover, the extent of adsorption of dye molecules is also increased on the surface of the photocatalyst [43-44].

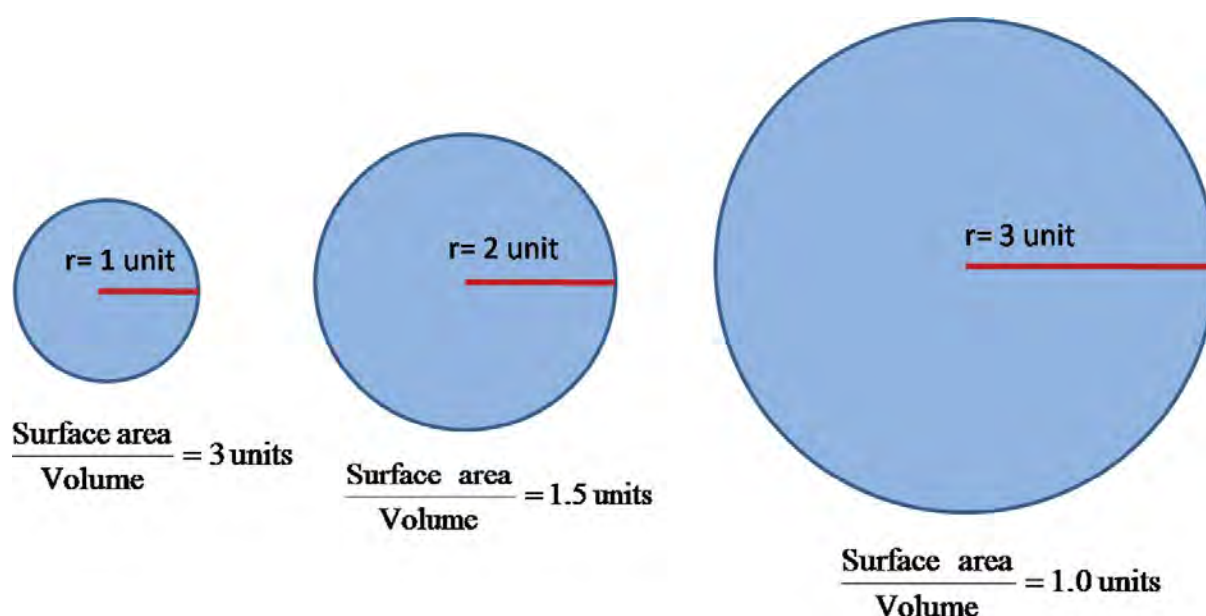


Figure 2.9 Representation of surface area to volume ratio

A red shift in UV-visible absorption spectra of the samples can be attributed to the agglomerations and large particle size at the high calcinations temperature. For high photo activity a photocatalyst should have large surface area and high crystallinity to reduce photo-excited electron-hole recombination rate. With increasing annealing temperature, crystallinity increases. Crystallinity plays an important role for the enhancement of photocatalytic activity as compared to the effects caused by large surface area up to a certain limit of annealing temperature. Decreased photocatalytic activity at high annealing temperatures can be ascribed to the reduction of surface area due to agglomerations [45-46].

2.8.3 Initial Dye Concentration

The quantity of active sites and the intensity of incident photons on the surface of ZnO photocatalyst are the two very important factors for the photodegradation process to take place. As the dye concentration is increased for a constant catalytic amount, fewer active sites are available for the degradation process. At higher dye concentration solution becomes more intense reducing the path length of photons, thereby lowering the number of photons on the catalyst surface. The dye molecules rather than the photocatalyst may absorb a significant amount of incident photons which may also reduce the catalytic efficiency. As a result, the production of relative amounts of $O_2^{\cdot-}$, HO^{\cdot}_2 , H_2O_2 and $\cdot OH$ on the surface of the catalyst is decreased, thereby decreasing the photocatalytic efficiency. So, photodegradation decreases with increasing dye concentration [47-49].

2.8.4 Catalyst Loading

The photocatalytic activity of ZnO nanoparticles is greatly affected by the amount of the catalyst added during photo-degradation process. Depending upon the concentration of dye, volume of the solution irradiated, experimental setup and energy of the incident photon different research groups have optimized the catalyst amount. Photodegradation efficiency increases with catalyst loading but a high dose of catalyst beyond a certain amount decreases the photodegradation efficiency of ZnO nanoparticles. The fact is that, increase of the amount of photocatalyst, increases the surface effective sites, consequently leading to enhanced production of $O_2^{\cdot-}$, HO^{\cdot}_2 , H_2O_2 and $\cdot OH$ radicals. The number of adsorbed dye molecules also increase owing to an increase in the number of photocatalyst particles, causing increased photo-degradation. When the amount of photocatalyst is enhanced beyond an optimum limit turbidity impedes further penetration of light in the solution and photo-degradation is decreased. At higher concentration, photocatalyst surface becomes unavailable for photon absorption. Furthermore, agglomeration and sedimentation of photocatalyst particles, light scattering at catalytic surface and deactivation of activated molecules by collision with ground state molecules are also found responsible for reducing the rate of photocatalytic reaction. The optimum catalyst loading is thus, dependent on initial solute concentration, total active surface area and availability of more active sites on catalyst surface [50-51].

2.8.5 pH of Reaction Solution

The presence of H^+ or OH^- ions in the reaction vessel during photocatalytic process can change the surface charge properties and size of ZnO nanoparticles [52]. ZnO can also undergo decomposition in strongly acidic ($pH < 4$) (Eq. (13)) or strongly alkaline ($pH > 11$) (Eq. (14)) medium.



Hence the pH of the reaction solution can effectively influence the photocatalytic efficiency of ZnO. In slightly acidic medium, the perhydroxyl radical (HO_2^{\cdot}) can form hydrogen peroxide, which can enhance the formation of the hydroxyl radical. Under weakly alkaline condition increased concentration of hydroxyl ions may induce hydroxyl radical formation. Hence, pH of solution plays an important role in the photo-degradation process using ZnO as photocatalyst. The exact interpretation is however difficult because it affects the electrostatic interactions between the dye and ZnO surface and charged or neutral radicals formed during the reaction process. The point zero charge (PZC) for ZnO is 9.0 ± 0.3 . Below $pH = 9$, ZnO surface is positively charged and above this pH, ZnO surface is negatively charged as shown in Figure 2.10 due to the adsorption of OH^- ions which favors the formation of OH^{\cdot} radical and hence, the enhancement of the photocatalytic efficiency [53-55].

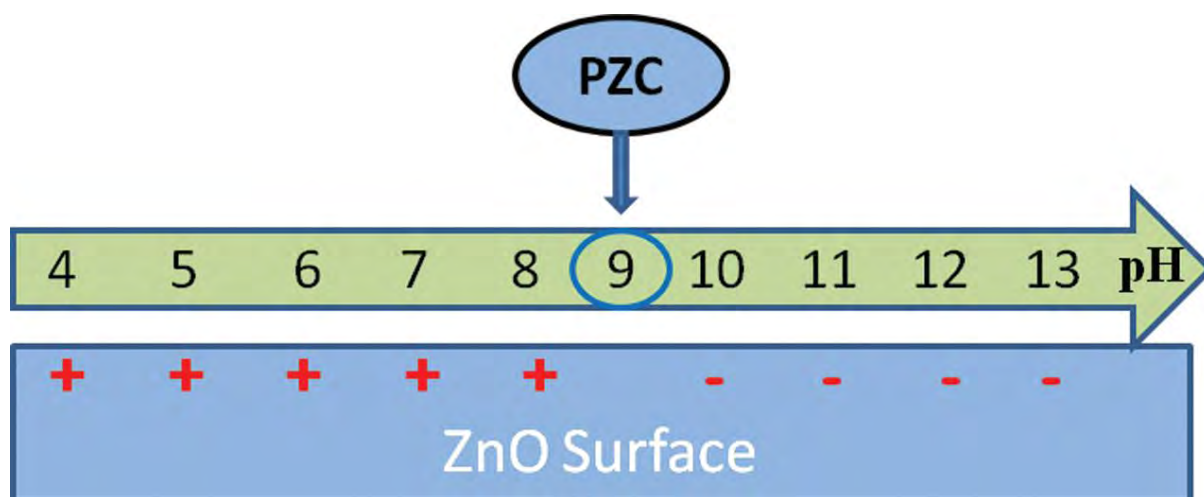


Figure 2.10 Surface charges for ZnO nanoparticles as a function of pH of reaction solution

2.9 LIMITATIONS AS PHOTOCATALYST

The major constraint of ZnO as a photocatalyst, however, is the rapid recombination rate of photogenerated electron-hole pairs, which perturbs the photodegradation reaction. Moreover, charge separation efficiency of ZnO is very low. Additionally, it has also been noted that the solar energy conversion performance of ZnO is affected by its optical absorption ability, which has been associated with its large band gap energy.

Therefore, intense efforts have been made to improve the optical properties of ZnO by decreasing the band gap energy and inhibiting the recombination of photogenerated electron-hole pairs. ZnO synthesis methods and the effect of various modification methods (such as tuning the microstructure, doping and coupling two semiconductors) are studied extensively over the world to improve the performance of ZnO in photocatalysis [4-6].

2.10 IMPROVEMENT OF ZnO AS PHOTOCATALYST

2.10.1 Metal/non-metal Doping

For using ZnO NPs in advanced and sophisticated industrial applications, numerous studies are taking place by researchers to find the optimum solution for enhancing the performance properties of ZnO without changing its physiochemical properties. Thus, modifications are taking place for improving its performance properties. For enhancing the properties of ZnO nanostructures, addition of impurity or defect is needed at the time of synthesis of nanoparticles. The addition of foreign atoms or impurities to a compound by creating defect for enhancing its physical properties is termed as doping. Here, doping is required to modify the physical properties of nanostructures [11]. The incorporation of defects or impurities into the semiconductor lattices is the primary means of controlling electrical conductivity, optical, luminescent, magnetic and other physical properties.

The pure ZnO is an insulator and the conductivity of ZnO can be observed over 10 orders of magnitude with the small change in the concentrations of native or non-native defects. At this magnitude, the electrical devices would not operate without having impurities. So, for using ZnO in different devices, the doping is required.

In ZnO nanostructures, there are two types of defects:

- Intrinsic defects
- Extrinsic defects

The intrinsic or native point defects concerned with ZnO NPs are the interstitial of zinc and oxygen and vacancies at the bonding between zinc and oxygen. The oxygen vacancies and zinc interstitials are dominant native or relevant donor. And in this, the formation of donor levels may probable, if the Fermi energy band is equal to the valence band. The main native acceptor in ZnO is the zinc vacancies. Its transition level energy is with 0.11 eV or 0.8 eV above EV depending on its transition state. Among the native point defects of ZnO NPs, oxygen anti-sites have the highest defect formation energy even for oxygen rich conditions and may be considered as deep acceptors.

Extrinsic defects are classified into two types: n-type and p-type. The n-type ZnO are obtained by doping with Group III elements as Al, In etc., transition metal elements as Pb, Mn, Fe, Sn, Co and rare earth metals as Eu, Y, Gd, Ho, Sm etc. These elements incorporate on the zinc lattice site and become shallower effective mass donors. The free electron concentration of n-type ZnO can be formed with the help of hydrogen. The formation of p-type ZnO for practical as well as industrial applications has proven very difficult and become the bottleneck in the development of ZnO-based devices due to the asymmetric doping limitations in ZnO nanostructures [57-59].

Non- metals like C, F, O and N can diffuse through the lattice interstices and bind to the atoms via oxidation process owing to their extremely small sizes. Carbon is a prominent candidate for a non-metal dopant for in semiconductors owing its high mechanical strength, good chemical resistance and special electronic properties. In addition, doping also can contribute to a greater production of OH^{*} radicals, thus, lead to a higher degradation efficiency of organic pollutants [60-62].

2.10.1.1 Potential Dopants: Rare-Earth Elements

For doping of ZnO, rare earth elements are more likely to be considered as dopants due to their optical and high conductivity properties. Rare earth metals doping for providing wide bandgap

semiconductors continues to be of interest for display applications involving UV, visible, and infrared light emission. Wide band gap exhibits less thermal quenching of emissions than narrow gap semiconductors. The studies of green luminescence from Tb-doped ZnO and red luminescence from Eu-doped ZnO suggest that these materials may prove useful in optoelectronic applications. The Gd-doped ZnO NPs shows the ferromagnetism which can be applied in spintronic applications. The properties of ZnO nanostructures depend on their crystal structure, morphology, size, and surface defects [63-65].

It has been extensively proven that modifications of ZnO Nanostructures such as doping of rare earth metals could improve their properties. The photocatalytic properties of ZnO NPs can significantly increase and improve when modified with the incorporation of rare earth dopant ions. Moreover, rare-earth doped ZnO samples with a high concentration of oxygen defects will exhibit excellent photodegradation of organic pollutants. Rare-earth dopants act as electron scavengers and prevent recombination of electron-hole pairs. The dopants increase trapping sites for photo-induced charge carriers leading to the reduced recombination rate. Hence, the photocatalytic activity of ZnO is enhanced. Moreover, rare-earth dopants narrow down band gap energy and make ZnO active in more region of solar spectrum. The doping of rare-earth ions in ZnO nanostructures can lead to effects such as an enhancement/decrease in fluorescence and controlling concentration of surface defects. The energy level or charge transfer between states helps in determining the intrinsic ferromagnetic properties of rare earth-doped ZnO [66-68].

2.10.2 Coupling with Other Semiconductors

Nanocomposites are preferable in several applications, especially for photocatalysis, because of their higher light absorption, better suppression of photoinduced electronhole pair recombination and increased charge separation. Coupling two semiconductors having different band gaps can become a highly active photocatalyst. ZnO coupled with other semiconductors, TiO_2/ZnO , SnO_2/ZnO , $\text{SnO}_2/\text{ZnO}/\text{TiO}_2$ and $\text{Co}_3\text{O}_4/\text{ZnO}$ are the most investigated materials for photocatalytic processes [69-72].

2.10.3 Crystal Growth and Shape Control

To improve the photocatalytic activity, various methods have been used to modify the morphology, size and growth of ZnO. By changing capping agent morphology of ZnO nanoparticles can be altered. The morphology of ZnO can be altered by manipulating the molar ratios of precursors [73-74].

2.10.4 Surface Modification of ZnO

Owing to the existence of Zn–O–Zn bonds in ZnO nanoparticles, agglomeration occurs readily, thus strongly limiting ZnO nanoparticle applications [75]. Surface modification may be the best approach for ensuring better dispersion by preventing the agglomeration of ZnO. In addition, surface modification has also been used to tune the ultraviolet and visible light photoluminescence, as the chemical and physical properties of ZnO nanoparticles can be modified via chemical surface modification through chemical treatment [76], coating [75], grafting polymerization [77], ligand exchange [78] and self-assembly techniques [79]. Chemical treatment is an approach that utilizes coupling agents (e.g. trimethoxyvinyl silane and oleic acid) to modify the surface of nanoparticles [80].

2.11 METHODS OF ZnO NANOPARTICLES PRODUCTION

2.11.1 Mechanochemical Process

The mechanochemical process is a cheap and simple method of obtaining nanoparticles on a large scale. It involves high-energy dry milling, which initiates a reaction through ball–powder impacts in a ball mill, at low temperature. A “thinner” is added to the system in the form of a solid, usually NaCl, which acts as a reaction medium and separates the nanoparticles being formed. A fundamental difficulty in this method is the uniform grinding of the powder and reduction of grains to the required size, which decreases with increasing time and energy of milling. Unfortunately, a longer milling time leads to a greater quantity of impurities. The

advantages of this method are the low production costs, small particle sizes and limited tendency for particles to agglomerate, as well as the high homogeneity of the crystalline structure and morphology [81-83].

The starting materials used in the mechanochemical method are mainly anhydrous ZnCl_2 and Na_2CO_3 . NaCl is added to the system; this serves as a reaction medium and separates the nanoparticles. The zinc oxide precursor formed, ZnCO_3 , is calcined at a temperature of 400–800 °C [81]. The process as a whole involves the following reactions (15) and (16):

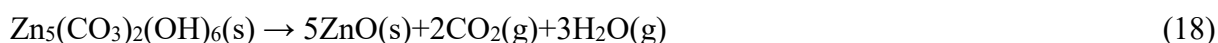
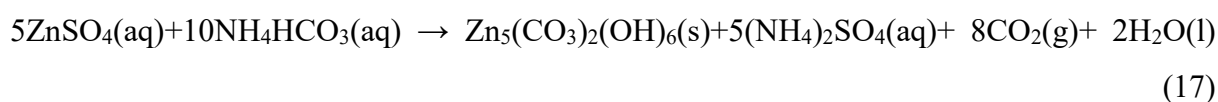


The size of the ZnO crystallites depends on the milling time and calcination temperature.

2.11.2 Controlled Precipitation

Controlled precipitation is a widely used method of obtaining zinc oxide, since it makes it possible to obtain a product with repeatable properties. The method involves fast and spontaneous reduction of a solution of zinc salt using a reducing agent, to limit the growth of particles with specified dimensions, followed by precipitation of a precursor of ZnO from the solution. At the next stage this precursor undergoes thermal treatment, followed by milling to remove impurities. It is very difficult to break down the agglomerates that form, so the calcined powders have a high level of agglomeration of particles. The process of precipitation is controlled by parameters such as pH, temperature and time of precipitation [84-85].

Zinc oxide has been precipitated from aqueous solutions of zinc chloride and zinc acetate. Controlled parameters in this process include the concentration of the reagents, the rate of addition of substrates, and the reaction temperature [85]. Zinc oxide NPs can be obtained by precipitation from aqueous solutions of NH_4HCO_3 and $\text{ZnSO}_4 \cdot 7\text{H}_2\text{O}$ (eqs. (17) - (18)).



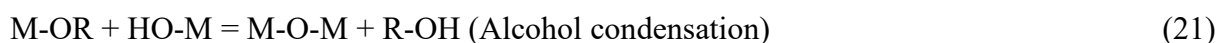
In processes of synthesis of nanopowders based on precipitation, it is increasingly common for surfactants to be used to control the growth of particles. The presence of these compounds affects not only nucleation and particle growth, but also coagulation and flocculation of the particles. The surfactant method involves chelation of the metal cations of the precursor by surfactants in an aqueous environment.

2.11.3 Sol-Gel Method

The obtaining of ZnO nanopowders by the sol-gel method is the subject of much interest, in view of the simplicity, low cost, reliability, repeatability and relatively mild conditions of synthesis, which are such as to enable the surface modification of zinc oxide with selected organic compounds. This changes in properties and extends its range of applications. The favourable optical properties of nanoparticles obtained by the sol-gel method have become a common topic of research, as reflected in numerous scientific publications [86-88].

The sol is a name of a colloidal solution made of solid particles few hundred nm in diameter, suspended in a liquid phase. Sol-gel process consists in the chemical transformation of a liquid (the sol) into a gel state and with subsequent post-treatment and transition into solid oxide material.

This process occurs in liquid solution of organometallic precursors (TMOS, TEOS, Zr(IV)-Propoxide, Ti(IV)-Butoxide, etc.), which, by means of hydrolysis and condensation reactions, lead to the formation of a new phase (SOL) (eqs.(19)-(21)).



Then the sol is converted to gel. The gel consists of loosely bonded material and a water-alcohol mixture. The jelly like material is heated to 200-500°C and is slowly dried to remove the liquid [89-91]. Figure 2.11 shows two examples of synthesis by the sol-gel method: films from a colloidal sol (Figure 2.11 (a)), and powder from a colloidal sol transformed into a gel (Figure 2.11 (b)).

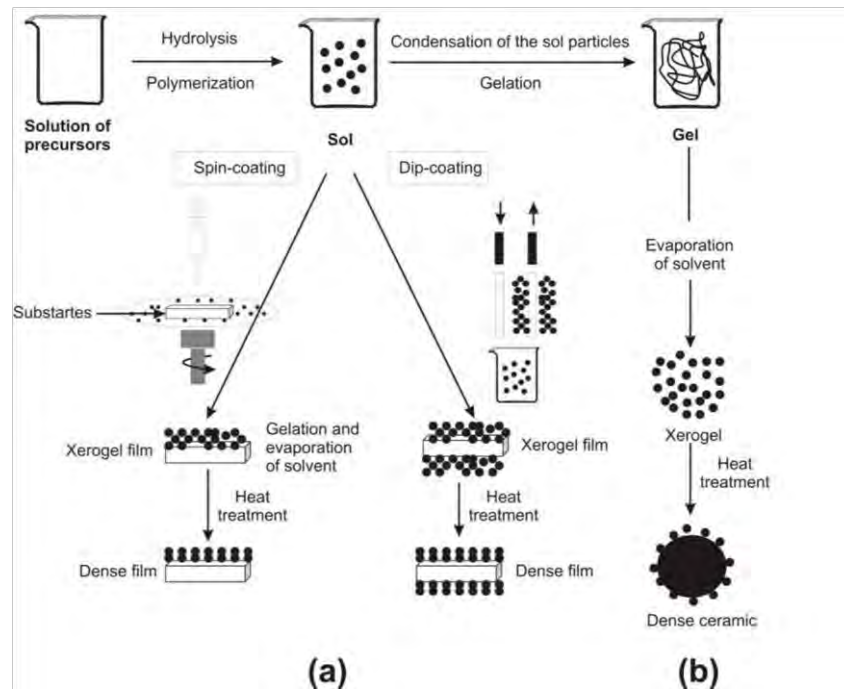


Figure 2.11 Overview showing two examples of synthesis by the sol-gel method: (a) films from a colloidal sol; (b) powder from a colloidal sol transformed into a gel

There are several variables in the sol-gel process:

- Rates of hydrolysis and condensation (relative differences in the rates can be used to modify the microstructure of the powder)
- Type of alkoxide (mixing of the alkoxides in the solution is achieved at a molecular level giving the powders a high degree of chemical homogeneity)
- Reaction temperature (affects the degree of polymerization of the gel)
- Amount of water added (affects the degree of polymerization of the gel)
- Solution pH (rates of hydrolysis and condensation can be increased by the addition of acids or bases, respectively)

The main benefits of sol-gel processing are:

- The high purity and uniform nanostructure achievable at low temperatures
- The idea behind sol-gel synthesis is to “dissolve” the compound in a liquid in order to bring it back as a solid in a controlled manner
- Multi component compounds may be prepared with a controlled stoichiometry by mixing sols of different compounds

- The sol-gel method prevents the problems with co-precipitation, which may be inhomogeneous, be a gelation reaction
- Enables mixing at an atomic level
- Results in small particles, which are easily sinterable
- Precise control over physical characteristics and morphology of NPs

2.11.3.1 Modified Sol-gel Method

Modified Sol-gel route involves only aqueous solvent unlike conventional sol-gel method. So, it leads to simplified chemical reactions and easy process control. Moreover, production cost is minimized as de-ionized water is used [92].

2.11.4 Solvothermal and Hydrothermal Method

The hydrothermal method does not require the use of organic solvents or additional processing of the product (grinding and calcination), which makes it a simple and environmentally friendly technique. The synthesis takes place in an autoclave, where the mixture of substrates is heated gradually to a temperature of 100–300°C and left for several days as shown in Figure 2.12. As a result of heating followed by cooling, crystal nuclei are formed, which then grow. This process has many advantages, including the possibility of carrying out the synthesis at low temperatures, the diverse shapes and dimensions of the resulting crystals depending on the composition of the starting mixture and the process temperature and pressure, the high degree of crystallinity of the product, and the high purity of the material obtained [92-94].

An example of a hydrothermal reaction is the synthesis of zinc oxide using the reagents ZnCl₂ and NaOH in a ratio of 1:2, in an aqueous environment (eq. (22)) [95]



The white Zn(OH)₂ precipitate underwent filtration and washing, and then the pH was corrected to a value of 5–8 using HCl. In the autoclave hydrothermal heating takes place at a programmed temperature for a set time, followed by cooling. The end product of the process is zinc oxide (eq. (23))



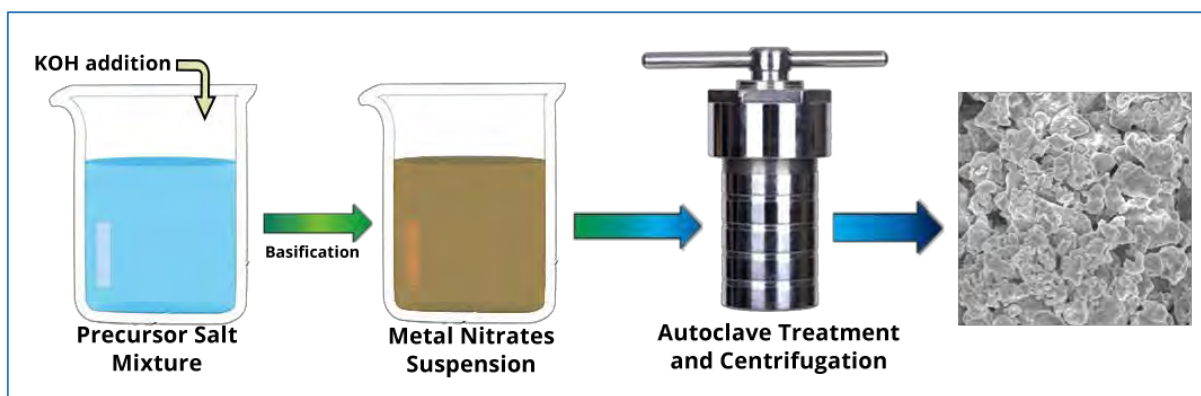


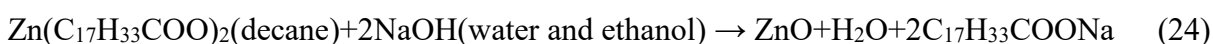
Figure 2.12 Overview of synthesis by the hydrothermal method

Solvothermal synthesis is very similar to the hydrothermal route (where the synthesis is conducted in a stainless steel autoclave), the only difference being that the precursor solution is usually non-aqueous using the solvothermal route gains one the benefits of both the sol-gel and hydrothermal routes. Thus, solvothermal synthesis allows for the precise control over the size, shape distribution, and crystallinity of metal oxide nanoparticles or nanostructure products. These characteristics can be altered by changing certain experimental parameters, including reaction temperature, reaction time, solvent type, surfactant type, and precursor type [96].

2.11.5 Method Using an Emulsion or Microemulsion Environment

The classic definition of an emulsion as a continuous liquid phase in which is dispersed a second, discontinuous, immiscible liquid phase is far from complete. One very convenient way to classify emulsions is first to divide them into two large groups based on the nature of the external phase. The two groups are usually called oil-in-water (O/W) and water-in-oil (W/O) emulsions. The terms “oil” and “water” are very general; almost any highly polar, hydrophilic liquid falls into the “water” category in this definition, while hydrophobic, nonpolar liquids are considered “oils” [97].

Zinc oxide precipitates in an interphase reaction of zinc oleate (dissolved in decane) with sodium hydroxide (dissolved in ethanol or water) (eq. (24)) [98].



Emulsions and microemulsions differ markedly from each other, which makes it relatively easy to identify the areas of their application. Microemulsions are stable, transparent, isotropic liquids consisting of an aqueous layer, and oil layer and a surfactant. The drop size in a microemulsion is significantly smaller than in an emulsion, and lies in the range 0.0015–0.15 μm . In contrast to emulsions, microemulsions form spontaneously in appropriate conditions.

2.11.6 Other Methods

There also exist many other methods of obtaining zinc oxide, including growing from a vapour phase, pyrolysis spray method, sonochemical method, synthesis using microwaves, and many others. Vapor phase approaches have also been used to produce nanostructured materials; these processes include thermal evaporation, pulsed laser deposition, physical vapor deposition (PVD), chemical vapor deposition (CVD), metal-organic chemical vapor deposition (MOCVD), plasma enhanced chemical vapor deposition (PECVD) and molecular beam epitaxy (MBE) [99-106].

2.12 APPLICATIONS OF ZnO

Because of its diverse properties, both chemical and physical, zinc oxide is widely used in many areas. It plays an important role in a very wide range of applications, ranging from tires to ceramics, from pharmaceuticals to agriculture and from paints to chemicals.

2.12.1 Rubber Industry

Global production of zinc oxide amounts to about 10^5 tons per year, and a major portion is consumed by the rubber industry to manufacture various different cross-linked rubber products [107]. The thermal conductivity of typical pure silicone rubber is relatively low; however, it can be improved by adding ZnO nanoparticles as thermal conductivity filler. In order to prepare the silicone rubber with high thermal conductivity, pristine and surface-modified ZnO

nanoparticles containing the vinyl silane group are incorporated into the silicone rubber via a hydrosilylation reaction during the curing process. Zinc oxide is a very effective and commonly used cross linking agent for carboxylated elastomers. It can be used to produce vulcanizates with high tensile strength, tear resistance, hardness and hysteresis. The improved mechanical properties of ionic elastomers mainly result from their high capacity for stress relaxation, due to elastomer chain slippage on the ionic cluster surface and reformation of ionic bonds upon external deformation of the sample [108].

2.12.2 The Pharmaceutical and Cosmetic Industries

Due to its antibacterial, disinfecting and drying properties, zinc oxide is widely used in the production of various kinds of medicines. It was formerly used as an orally administered medicine for epilepsy and later for diarrhoea. At the present time it is applied locally, usually in the form of ointments and creams, and more rarely in the form of dusting powders and liquid powders. ZnO has properties which accelerate wound healing, and so it is used in dermatological substances against inflammation and itching. In higher concentrations it has a peeling effect. It is also used in suppositories. In addition it is used in dentistry, chiefly as a component of dental pastes, and also for temporary fillings. ZnO is also used in various types of nutritional products and diet supplements, where it serves to provide essential dietary zinc. For many years, before sun creams began to contain nanoparticles of ZnO, they contained thick preparations which did not rub easily into the skin and which were cosmetically unattractive. Due to their ability to absorb UVA and UVB radiation, these products began to be used in creams. A new cream formula, containing a combination of ZnO and TiO₂, solved the problem of an insufficiently white layer and produced a new medium which is more transparent, less adhesive and much more easily rubbed into the skin. A number of studies have shown that titanium and zinc oxides are extremely good media in sun creams, since they absorb UV radiation, do not irritate the skin, and are easily absorbed into the skin [109-112].

2.12.3 The Textile Industry

For textile applications, not only is zinc oxide biologically compatible, but also nanostructured ZnO coatings are more air-permeable and efficient as UV-blockers compared with their bulk

counterparts. Therefore, ZnO nanostructures have become very attractive as UV-protective textile coatings. Different methods have been reported for the production of UV-protecting textiles utilizing ZnO nanostructures. For instance, hydrothermally grown ZnO nanoparticles in SiO₂-coated cotton fabric showed excellent UV-blocking properties. Synthesis of ZnO nanoparticles elsewhere through a homogeneous phase reaction at high temperatures followed by their deposition on cotton and wool fabrics resulted in significant improvement in UV-absorbing activity. Zinc oxide nanowires shown self-cleaning, superhydrophobicity and ultraviolet (UV) blocking properties [113-115].

2.12.4 The Electronics and Electrotechnology Industries

Zinc oxide is a new and important semiconductor which has a range of applications in electronics and electrotechnology. Its wide energy band (3.37 eV) and high bond energy (60 meV) at room temperature mean that zinc oxide can be used in photoelectronic and electronic equipment, in devices emitting a surface acoustic wave, in field emitters, in sensors, in UV lasers, and in solar cells [116-118].

ZnO also exhibits the phenomenon of luminescence (chiefly photoluminescence—emission of light under exposure to electromagnetic radiation). Because of this property it is used in FED (field emission display) equipment, such as televisions. It is superior to the conventional materials, sulfur and phosphorus (compounds exhibiting phosphorescence), because it is more resistant to UV rays, and also has higher electrical conductivity. The photoluminescent properties of zinc oxide depend on the size of crystals of the compound, defects in the crystalline structure, and also on temperature [119-120].

ZnO is a semiconductor, and thin films made of that material display high conductivity and excellent permeability by visible rays. These properties mean that it can be used for the production of light-permeable electrodes in solar batteries. It also has potential uses as a transparent electrode in photovoltaic and electroluminescent equipment, and is a promising material for UV-emitting devices [121-122].

Zinc oxide is also used in gas sensors. It is a stable material whose weak selectivity with respect to particular gases can be improved by adding other elements. The working temperature of ZnO is relatively high (400–500°C), but when nanometric particles are used this can be reduced to around 300 °C. The sensitivity of such devices depends on the porosity and grain size of the material; sensitivity increases as the size of zinc oxide particles decreases. It is most commonly used to detect CO and CO₂ (in mines and in alarm equipment), but can also be used for the detection of other gases (H₂, SF₆, C₄H₁₀, C₂H₅OH). The zinc oxide used in the production of such equipment is obtained by a variety of methods (chemical vapour deposition, aerosol pyrolysis or oxidation of metallic zinc); it is important to control the process temperature, since this determines the properties of the product [123-124].

One of the most important applications of zinc oxide in electronics is in the production of varistors. These are resistors with a non-linear current-voltage characteristic, where current density increases rapidly when the electrical field reaches a particular defined value. They are used, among other things, as lightning protectors, to protect high-voltage lines, and in electrical equipment providing protection against atmospheric and network voltage surges. These applications require a material of high compactness, since only such a material can guarantee the stability and repeatability of the characteristics of elements made from it [125].

Certain unique electronic properties of ZnO are exploited in projection processes. The zinc oxide used for this purpose is produced from metallic zinc (from a suitable ore), so as to obtain a high-purity product. The photoconductor and semiconductor properties of ZnO are improved by thermal treatment, and also by the addition of other elements [126].

2.12.5 Miscellaneous Applications

Apart from the applications mentioned above, zinc oxide can also be used in other branches of industry, including for example concrete production. The addition of zinc oxide improves the process time and the resistance of concrete to the action of water. Also, the addition of ZnO to Portland cement slows down hardening and quenching (it reduces the gradual evolution of heat), and also improves the whiteness and final strength of the cement. Zinc oxide reacts with silicates (e.g., sodium silicate) to produce zinc silicates, which are water-

and fire-resistant materials used as binders in paints. These fire-resistant and adhesive substances are used in the binding of cements used in the construction industry. Methanol, the third most-important chemical product of chemical industry, is produced using a Cu/ZnO/Al₂O₃ catalyst, with small Cu particles promoted by their interaction with the ZnO substrate as the active component [127].

ZnO is also used for the production of typographical and offset inks. It imparts good printing properties (high fluidity). The addition of ZnO means that the inks have better covering power, pure shade and high durability, and prevents darkening. Zinc oxide is also used in pigments to produce shine. It is added to many food products, including breakfast cereals. ZnO is used as a source of zinc, which is an essential nutrient. Thanks to their special chemical and antifungal properties, zinc oxide and its derivatives are also used in the process of producing and packing meat products (e.g., meat and fish) and vegetable products (e.g., sweetcorn and peas) [128].

As mentioned above, ZnO and its derivatives suppress the development and growth of fungi and moulds. Zinc oxide is added to fungicides to improve their effectiveness. Zinc oxide is also being used increasingly often as an animal feed additive, as it supports the correct growth of animals. It is also used as an artificial fertilizer [129].

Zinc oxide also has uses in criminology, in mechanical fingerprint analysis. It is also an ingredient in cigarette filters, as it selectively removes certain components from tobacco smoke. Filters are made of charcoal impregnated with ZnO and Fe₂O₃, which remove significant quantities of HCN and H₂S from tobacco smoke without producing a smell. It also removes sulfur and its compounds from various liquids and gases, particularly industrial waste gases. Zinc also removes H₂S from hydrocarbon gas, and desulfurizes H₂S and other sulphur components.

ZnO and its derivatives are also used as an additive to car lubricating oils, reducing consumption and oxygen corrosion. Zinc oxide has also been used in various types of other lubricants, such as those with EP additives, vibration-resistant lubricants and solid lubricants. In the future, advantage may also be taken of the adhesive properties of ZnO. Because the compound is nontoxic, cheap, and chemically stable in the air, nanoparticles of zinc oxide can be used to make new eco-friendly substances for cell marking. Recent advances in

electrochemical biosensing based on a wide variety of nanostructures such as ZnO nanowires, nanotubes and nanoporous materials have attracted great interest in biosensor applications due to their remarkable properties such as non-toxicity, bio-safety, excellent biological compatibility, high electron transfer rates, enhanced analytical performance, increased sensitivity, easy manufacture and low cost. Moreover, ZnO has a high isoelectric point (IEP) of about 9.5, which can be expected to provide a positively charged substrate for immobilization of low-IEP proteins or enzymes such as uricase (IEP ~ 4.6) at a physiological pH of 7.4. In addition, ZnO has high ionic bonding (60%), and it dissolves very slowly at biological pH values [130-131].

3 EXPERIMENTAL

The objective of this research was to synthesize rare-earth element doped ZnO nanoparticles and characterize its photocatalytic activity. So, experimental work of this thesis included

- Synthesis of ZnO nanoparticles by modified sol-gel method
- Doping rare earth element such as Holmium (Ho) and Samarium (Sm) in ZnO nanoparticles
- Studying the effect of doping on structural modification of ZnO nanoparticles and investigating its photocatalytic activity

3.1 RAW MATERIALS

To synthesize undoped and rare-earth doped ZnO NPs by modified sol gel method the following materials were used.

- Precursor of ZnO: **Zinc nitrate hexahydrate, $\text{Zn}(\text{NO}_3)_2 \cdot 6\text{H}_2\text{O}$** (Merck-India). ZnO prepared using Zinc nitrate shows a rapid and random crystallization compared to that prepared using zinc acetate. So, zinc nitrate was used as the precursor material in this thesis.
- Dopant Precursor: **Holmium nitrate pentahydrate, $\text{Ho}(\text{NO}_3)_3 \cdot 5\text{H}_2\text{O}$** (Sigma Adrich-USA) & **samarium nitrate hexahydrate, $\text{Sm}(\text{NO}_3)_3 \cdot 6\text{H}_2\text{O}$** (Sigma Adrich-USA)
- Chelating Agent: **Citric acid, $\text{C}_6\text{H}_8\text{O}_7$** (Merck-India). Chelating agents react with metal ions to form a stable, water soluble complex.
- Chain-transfer Agent: **Ethylene glycol, $\text{C}_2\text{H}_6\text{O}_2$** (Merck-India). Chain-transfer agents create active centers which are transferable to other molecules and fasten the reaction kinetics.
- Solvent: **Deionized water (DI)**. Water solvent gives oxygen which is must for forming ZnO.

3.2 SYNTHESIS OF ZNO NANOPARTICLES

- **Weight Measurement:** At first, weight of the powders according to the target composition were precisely measured using weighting machine.
- **Sol Formation:** After weighting, powders were taken into a 500 ml beaker. 150 mL de-ionized water was added in the beaker to make the precursor solution. Beaker was then placed on a hot plate with magnetic stirrer. The solution was stirred at 300 rpm while solution temperature was maintained at 80°C for 60 minutes. Citric acid and 5ml ethylene glycol were then added to the transparent solution.
- **Gel Formation:** Heating and stirring was continued for further 2 hours. A thick gel formed meanwhile.
- **Drying:** Gel was dried in an oven at 120°C for 18 hours.
- **Grinding:** Dried gel was crushed in a mortar and fine powders were obtained.
- **Annealing:** Pulverized powers obtained after grinding were not crystalized. To achieve crystallization, powders were taken into a 25 mL alumina crucible and annealed for 2 hours at several selected annealing temperature where heating rate was 5°C/min. Pulverized pure ZnO powers were annealed at 400°C, 500°C, 600°C and 700°C. Then the annealing temperature was optimized at 500°C by analyzing the experimental results. Later, doped ZnO powders were annealed at 500°C.

Chelating agent concentration was varied to analyze its impact on nanoparticles morphology. Two different molar ratios of precursor to chelating agent (1:1 and 1:2) were used and by investigating experiment results 1:2 molar ratio (precursor: chelating agent) was selected for doping purpose. Experimental variables and raw material need for different compositions were summarized in Table 3.1.

Table 3.1 Experimental variables and raw materials for different compositions

Composition	Raw Materials	Weight (gm)	Molar Ratio of Precursor to Chelating Agent	Annealing Temperature (°C)
ZnO	Zn(NO ₃) ₂ .6H ₂ O	4.46	1:1	500
	C ₆ H ₈ O ₇	3.165		
ZnO	Zn(NO ₃) ₂ .6H ₂ O	4.46	1:2	400, 500, 600 and 700
	C ₆ H ₈ O ₇	6.33		
Zn _{0.99} Ho _{0.01} O	Zn(NO ₃) ₂ .6H ₂ O	4.418	1:2	500
	C ₆ H ₈ O ₇	6.33		
	Ho(NO ₃) ₃ .5H ₂ O	0.06615		
Zn _{0.97} Ho _{0.03} O	Zn(NO ₃) ₂ .6H ₂ O	4.3285	1:2	500
	C ₆ H ₈ O ₇	6.33		
	Ho(NO ₃) ₃ .5H ₂ O	0.1985		
Zn _{0.95} Ho _{0.05} O	Zn(NO ₃) ₂ .6H ₂ O	4.2392	1:2	500
	C ₆ H ₈ O ₇	6.33		
	Ho(NO ₃) ₃ .5H ₂ O	0.3308		
Zn _{0.99} Sm _{0.01} O	Zn(NO ₃) ₂ .6H ₂ O	4.418	1:2	500
	C ₆ H ₈ O ₇	6.33		
	Sm(NO ₃) ₃ .6H ₂ O	0.0667		
Zn _{0.97} Sm _{0.03} O	Zn(NO ₃) ₂ .6H ₂ O	4.3285	1:2	500
	C ₆ H ₈ O ₇	6.33		
	Sm(NO ₃) ₃ .6H ₂ O	0.2		
Zn _{0.95} Sm _{0.05} O	Zn(NO ₃) ₂ .6H ₂ O	4.2392	1:2	500
	C ₆ H ₈ O ₇	6.33		
	Sm(NO ₃) ₃ .6H ₂ O	0.3334		

3.3 CHARACTERIZATIONS

3.3.1 X-ray Diffractometry (XRD)

Philips x-ray diffractometer [PW 3040-X'Pert PRO] (Figure 3.1) was used for structural and phase analysis of nanoparticles utilizing a Cu x-ray source having wavelength: $K_{\alpha 1} = 1.540598 \text{ \AA}$. The diffraction was performed using Bragg angles between $2\theta = 10^\circ$ to 90° at a scanning rate of $0.2^\circ/\text{min}$. The Rietveld refinement of pristine and doped ZnO nanoparticles was done using Highscore Plus software. X-ray diffraction combined with Rietveld analysis, provides detailed information regarding unit cell dimensions, bond-lengths, bond-angles and the site ordering of crystallites.



Figure 3.1 XRD Machine

3.3.2 Field Emission Scanning Electron Microscopy (FESEM)

Field emission scanning electron microscope (FESEM: JEOL, JSM, 7600F) (Figure 3.2) was used to investigate the size and morphology of the nanoparticles. The attached energy dispersive X-ray spectroscopy (EDS) was used for elemental analysis of the nanoparticles. Grain size was estimated with Image J software.



Figure 3.2 FESEM

3.3.3 Differential Scanning Calorimetry (DSC) & Thermogravimetric Analysis (TGA)

For DSC and TGA, Simultaneous Thermogravimetry-Differential Scanning Calorimetry (STA/TG-DSC) (Figure 3.3) was used. Scanning was done in controlled atmosphere over a temperature range 0-800°C with a heating rate of 10°C/min. DSC measured the difference in

heat flow between sample and inert reference as a function of temperature, which was used to determine crystallization temperature and other endothermic and exothermic reactions. TGA was used to measure the weight change during heating. The analysis of these two plots could potentially explain the sample history and improve the experimental design.



Figure 3.3 STA/TG-DSC

3.3.4 UV-vis Spectroscopy

Reflectance and absorbance spectra were measured using SHIMADZU UV 2600 Spectrophotometer (Figure 3.4). Band gap was calculated using Kubelka-Munk theory from the diffuse reflectance spectra.



Figure 3.4 UV-vis Spectroscopy

3.3.5 Photoluminescence Spectroscopy

Photoluminescence spectra was measured using SHIMADZU RF-6000 Spectrofluorophotometer (Figure 3.5). PL spectra is an effective way to study the electronic structure, optical and photochemical properties of semiconductor materials, by which information such as surface oxygen vacancies and defects, as well as the efficiency of charge carrier trapping, immigration and transfer can be obtained. PL spectra was used to monitor near band gap emission and recombination rate of undoped and doped ZnO nanoparticles.

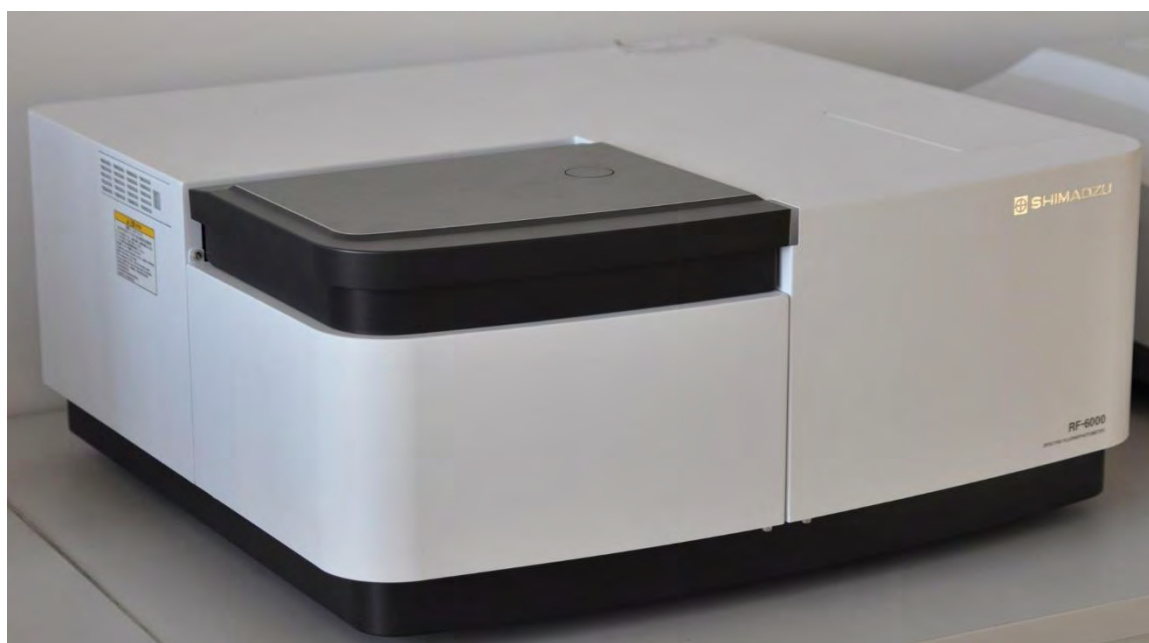


Figure 3.5 Spectro-fluorophotometer

3.3.6 Photocatalytic Activity Measurement

The photocatalytic activities of ZnO nanoparticles annealed at 500°C and 600°C were investigated using Methylene Blue (MB) in aqueous solution as a probe molecule for photodegradation under UV light irradiation. 100 ml 10 mg/L MB solution was taken in a 250 ml quartz beaker. To adjust its pH around 10, ammonium hydroxide (NH₄OH) solution was added dropwise. 80 mg photocatalyst was then added in the solution to create a suspension. Prior to photoreaction, the suspension was magnetically stirred in a dark box for 30 minutes to establish an adsorption/desorption equilibrium condition. Two ultraviolet bulbs (UV A, 20 W)

were employed as the radiation source. The solution was irradiated with UV light, and photocatalytic experiment was started. The photocatalytic degradation of MB was monitored by withdrawing 6 mL samples at regular intervals and immediately centrifuged (10,000 rpm) to remove particles for further analysis. The analysis of concentration of MB was carried out by measuring of the absorbance of MB at 665 nm by using a UV spectrometer. Degradation efficiency was calculated from the absorbance data. Total setup is shown in Figure 3.6.

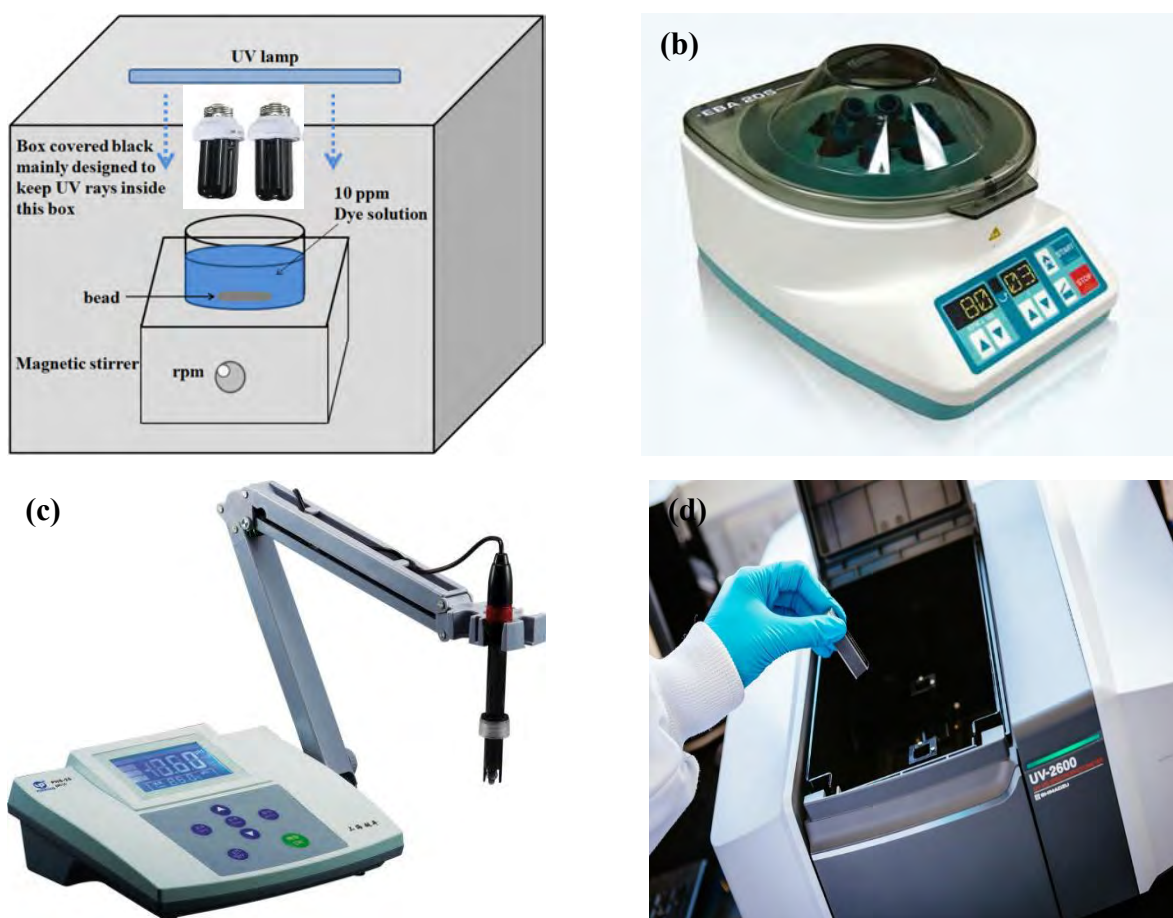


Figure 3.6 Photocatalytic activity measurement setup: (a) dark box with UV light, (b) centrifuge machine, (c) pH meter, (d) UV-vis spectroscopy

For pristine and doped ZnO nanoparticles annealed at 500⁰C, aqueous solution of Rhodamine B (Rh B) was used to investigate photodegradation under UV light radiation. Rhodamine B is a toxic colorant used in textile and medical industry. 12.5 ppm 100 ml solution was taken and pH was adjusted around 10 by adding ammonium hydroxide (NH₄OH) solution dropwise. 80 mg photocatalyst was added to create a suspension. The suspension was magnetically stirred in a dark box for 30 minutes to establish an adsorption/desorption equilibrium condition as like

before. For irradiation Xenon lamp (lump housing E10180, 500 W) (Figure 3.7) was used with a visible light blocking filter. The allowed only UV-radiation to pass through. To monitor photocatalytic degradation of Rhodamine B 6 mL samples at regular intervals was withdrawn and immediately centrifuged (10,000 rpm) to remove particles. The analysis of concentration of Rh B was carried out by measuring of the absorbance of RhB at 555 nm by using a UV spectrometer. Degradation efficiency and kinetics of degradation was investigated by the absorbance data.



Figure 3.7 Photocatalytic activity measurement setup with Xenon lump housing E10180

Rhodamine B and Methylene Blue have different functional groups (Figure 3.8). So absorption peak was found at around 665 nm from MB solution, whereas for Rh B solution it was around 555nm. Photocatalysts reacts with this functional groups and breaks the bond between the groups. By doing so, absorbance of characteristic peaks decreases with increased irradiation.

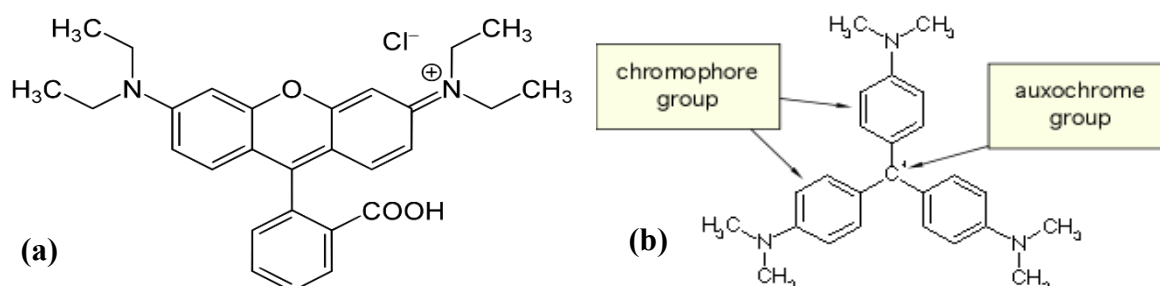


Figure 3.8 Functional group present in dyes: (a) Rhodamine B and (b) Methylene Blue

4 RESULTS AND DISCUSSION

Synthesized pristine and doped ZnO nanoparticles were characterized by XRD, SEM, UV-VIS spectroscopy, PL spectroscopy, DSC and TGA. XRD was employed for structural and phase analysis of the nanoparticles. Morphological and elemental analysis was done by SEM equipped with EDX. Diffuse reflectance spectra obtained from UV-VIS spectroscopy were employed to calculate band gap using Kubelka-Munk formula. PL spectra was used to monitor near band gap emission and recombination rate of undoped and doped nanoparticles. To determine crystallization temperature along with weight changes during heating, simultaneous DSC and TGA was employed. Finally, Photocatalytic activity was investigated by the degradation of dye (Methylene blue and Rhodamine B) in a dark box using Xenon lamp of 500 W.

4.1 OPTIMIZATION OF ANNEALING TEMPERATURE

4.1.1 XRD for Different Annealing Temperatures

Figure 4.1 shows XRD patterns of ZnO nanoparticles annealed at 400^oC, 500^oC, 600^oC and 700^oC. For crystalline ZnO nanoparticles XRD peaks for (100), (002), (101), (102), (110), (103), (200), (112), (201), (004) and (202) planes are found at 2 θ values 31.728, 34.400, 36.212, 47.494, 56.519, 62.803, 66.283, 67.866, 68.992, 72.516 and 76.860 (JCPDS 36-1451). From figure 4.1, as the diffraction data are in good agreement with the JCPDS card for ZnO, it is clearly evident that ZnO annealed at all four temperatures have satisfactory correspondence with hexagonal wurtzite structure [132]. As annealing temperature was increased, intensity of all the planes were increased showing increasing crystallinity with increasing annealing temperature. Crystalline ZnO nanoparticles show preferential growth along (002) plane [133]. As the normalized peak intensity of (002) plane increased with increasing annealing temperature, it is again clearly evident that crystallinity of the annealed ZnO nanoparticles were increased with increasing annealing temperature.

XRD data of all the annealed ZnO Nanoparticles were analyzed and showed in Table 4.1-4.4. Lattice parameters were obtained by rietveld analysis using Highscore Plus software and summarized in Table 4.5. A decrease in the value of full width at half maximum was observed

for the all planes with increasing annealing temperature from 400⁰C to 700⁰C. As FWHM decreased with increasing annealing temperature, crystallite size was increased. Meanwhile, micro-strain of all the planes decreased with increasing annealing temperature. Micro-strain is the root mean square of the variations in the lattice parameters across the structure. A positive (non-zero) value of micro-strain means the distance of the relevant crystal planes are not identical, possibly due to the presence of defects and stress. Crystallite size and micro-strain values were obtained during rietveld analysis and showed in Table 4.1-4.4. Average crystallite size was increased from 26 nm for annealing temperature 400⁰C to 64 nm for annealing temperature 700⁰C. Meanwhile, average micro-strain size was decreased from 0.34 for annealing temperature 400⁰C to 0.14 for annealing temperature 700⁰C.

With increasing annealing temperature, as crystallinity was increased (evident from Figure 4.2), crystallite size was increased by crystal growth. During increasing crystallinity, strain was decreased as increasing annealing temperature resulted in decrease in the distance of relevant crystal planes corresponds to the equilibrium structure. With increasing annealing temperature increase in crystallinity was also confirmed as extent of crystallinity was calculated from the ratio of total area of crystalline peaks to total area under the diffraction curve (crystalline plus amorphous peaks) using origin software. Crystallinity of ZnO nanoparticles were increased from 80.1% for annealing temperature 400⁰C to 84.3% for annealing temperature 700⁰C.

Table 4.5 shows, lattice parameter (a) was increased and (c) was decreased with increasing annealing temperature. (c/a) ratio was decreased from 1.6028 for annealing temperature 400⁰C to 1.6018 for annealing temperature 700⁰C. Decreasing value of (c/a) with increasing annealing temperature is in well agreement with decreasing microstrain of the ZnO nanoparticles annealed at progressively higher temperature.

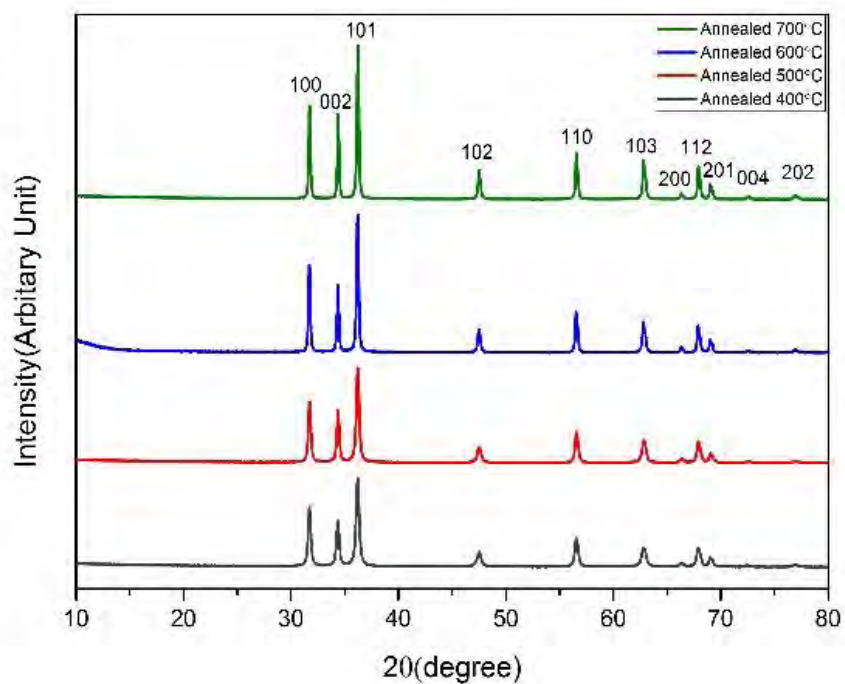


Figure 4.1 XRD patterns showing crystalline structure of ZnO nanoparticles annealed at different temperatures

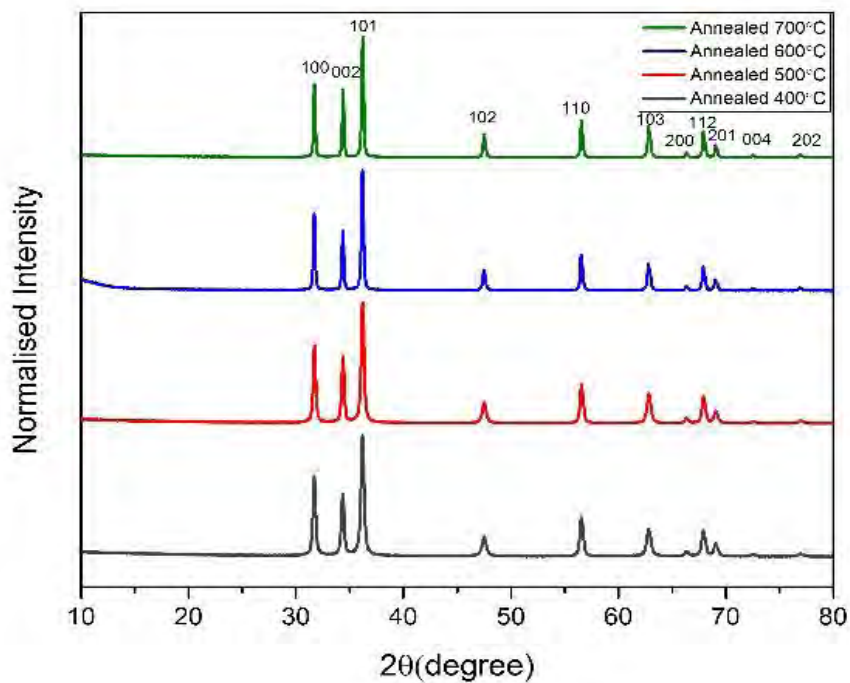


Figure 4.2 XRD patterns showing increasing crystallinity of ZnO nanoparticles with increasing annealing temperature (normalized XRD patterns)

Table 4.1 XRD data analysis for annealing temperature 400°C

Peak No	Peak position(2θ) (degree)	d-spacing (Å)	FWHM (degree)	Crystallite size (nm)	Micro-strain (%)	hkl
1	31.6942	2.82087	0.3134	27.1	0.5212	100
2	34.3355	2.60968	0.3165	26.9	0.48478	002
3	36.1776	2.48091	0.3187	26.8	0.46255	101
4	47.4607	1.91411	0.3348	26.3	0.36444	102
5	56.5302	1.62664	0.3508	25.9	0.31426	110
6	62.7769	1.47896	0.3638	25.7	0.28823	103
7	66.3155	1.40836	0.372	25.5	0.27567	200
8	67.8805	1.37965	0.3758	25.5	0.27055	112
9	69.0255	1.35954	0.3787	25.5	0.26694	201
10	72.479	1.30303	0.3877	25.4	0.25676	004
11	76.8978	1.23879	0.4004	25.3	0.24508	202

- Average crystallite size 26 nm and average microstrain 0.34
- Crystallinity 80.1%

Table 4.2 XRD data analysis for annealing temperature 500°C

Peak No	Peak position(2θ) (degree)	d-spacing (Å)	FWHM (degree)	Crystallite size (nm)	Micro-strain (%)	hkl
1	31.7089	2.8196	0.2851	30.9	0.45583	100
2	34.3559	2.60817	0.2886	30.7	0.42543	002
3	36.1936	2.47985	0.2912	30.5	0.40699	101
4	47.4795	1.91339	0.3094	29.4	0.32556	102
5	56.5441	1.62627	0.3272	28.6	0.28411	110
6	62.7989	1.4785	0.3415	28.2	0.2626	103
7	66.3291	1.40811	0.3504	27.9	0.25227	200
8	67.8975	1.37935	0.3545	27.8	0.24804	112
9	69.0398	1.35929	0.3576	27.7	0.24507	201
10	72.506	1.30261	0.3675	27.5	0.23665	004
11	76.9142	1.23857	0.381	27.3	0.22704	202

- Average crystallite size 28.8 nm and average microstrain 0.31
- Crystallinity 81.2%

Table 4.3 XRD data analysis for annealing temperature 600°C

Peak No	Peak position(2θ) (degree)	d-spacing (Å)	FWHM (degree)	Crystallite size (nm)	Micro-strain (%)	hkl
1	31.6899	2.82125	0.1886	52.8	0.26704	100
2	34.3465	2.60887	0.1895	52.7	0.24734	002
3	36.1766	2.48097	0.1902	52.7	0.23542	101
4	47.467	1.91387	0.1951	52.7	0.1816	102
5	56.5237	1.62681	0.2	53.1	0.15331	110
6	62.7921	1.47864	0.2041	53.5	0.13815	103
7	66.3082	1.4085	0.2066	53.9	0.13077	200
8	67.8824	1.37962	0.2078	54.0	0.12769	112
9	69.0203	1.35963	0.2087	54.2	0.12553	201
10	72.5079	1.30258	0.2116	54.6	0.11929	004
11	76.8983	1.23878	0.2157	55.2	0.11211	202

- Average crystallite size 53.6 nm and average microstrain 0.17
- Crystallinity 82.8%

Table 4.4 XRD data analysis for annealing temperature 700°C

Peak No	Peak position(2θ) (degree)	d-spacing (Å)	FWHM (degree)	Crystallite size (nm)	Micro-strain (%)	hkl
1	31.7127	2.81927	0.1703	61.8	0.22805	100
2	34.3732	2.6069	0.171	61.8	0.21099	002
3	36.2001	2.47942	0.1715	61.8	0.20067	101
4	47.4917	1.91293	0.1749	62.2	0.15374	102
5	56.5443	1.62627	0.1783	63.1	0.1288	110
6	62.8178	1.4781	0.1811	64.1	0.11529	103
7	66.3276	1.40814	0.1829	64.8	0.10869	200
8	67.9041	1.37923	0.1837	65.1	0.10591	112
9	69.0399	1.35929	0.1843	65.4	0.10397	201
10	72.5361	1.30214	0.1864	66.2	0.09831	004
11	76.9186	1.2385	0.1892	67.5	0.09178	202

- Average crystallite size 64 nm and average microstrain 0.14
- Crystallinity 84.3%

Table 4.5 Rietveld analysis for ZnO nanoparticles annealed at different temperatures

Annealing temperature (°C)	Lattice Parameter			R _w	R _{exp}	χ ² = R _w /R _{exp}
	a (Å)	c (Å)	c/a			
400	3.249466	5.2081	1.6028	8.97	4.93	1.80
500	3.249513	5.2072	1.6024	8.84	4.93	1.79
600	3.249814	5.2062	1.6020	8.33	4.77	1.74
700	3.249847	5.2057	1.6018	8.61	4.86	1.77

Activation energy required for the crystal growth at different temperature was calculated by Scott's equation [132]. Lower activation energy allows to attain high crystallinity with lower energy consumption.

$$\text{Scott's equation: } D = C \exp\left(\frac{-E}{RT}\right) \quad (25)$$

Where,

D = Average crystallite size

C = Constant

E = Activation energy for crystallite growth

R = Gas constant

T = Absolute temperature

Assuming homogenous crystallite growth of ZnO nanoparticles, Scott's formula was used to calculate activation energies for different annealing temperatures. Activation energy (E/R), later multiplied by R, was obtained from the slope of the plot of ln D against 1/T (Figure 4.3). Activation energy was found to be 4.3 kJ/mole, 34.9 kJ/mole and 12.6 kJ/mole for 400-500°C, 500-600°C and 600-700°C temperature range, respectively. Similar trend was also reported by other researchers [134]. Different ZnO crystallite growth rate at different annealing temperatures range, as activation energy was different, resulted in different morphology and crystallite size leading to different photocatalytic activity [132].

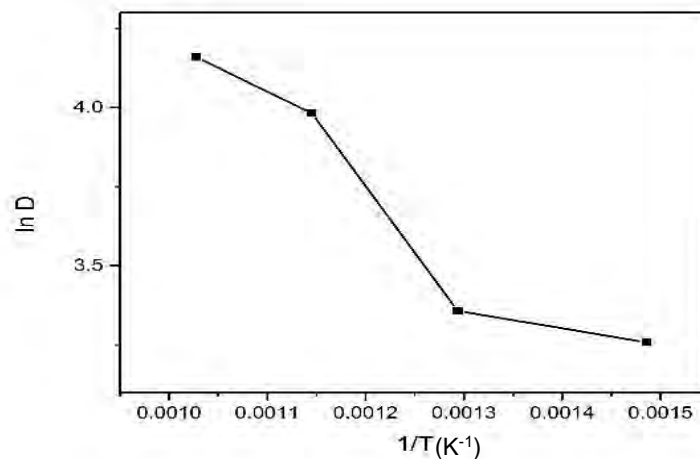


Figure 4.3 Variation of activation energy for ZnO nanoparticles annealed at different temperature change

4.1.2 SEM for Different Annealing Temperatures

Figure 4.4 exhibits morphological images of ZnO nanoparticles annealed at different temperatures. ZnO nanoparticles annealed at 400°C shows nearly spherical particles with average particle size of 31.94 nm due to quantum confinement effect [39]. Particle size was calculated using ImageJ software and particle size distribution was found using OriginPro software. It is evident from the micrographs that ZnO nanoparticles become hexagonal shaped with increasing annealing temperature. Average particle size of ZnO nanoparticles were measured 37.28 nm, 67.75 nm and 98.94 nm for annealing temperatures of 500°C, 600°C, and 700°C, respectively, showing increasing particle size with an increase in annealing temperature. ZnO nanoparticles annealed at 400°C and 500°C, were densely distributed and their surface area were larger compared with the nanoparticles annealed at 600°C and 700°C, as evident from the micrographs (Figure 4.4). With an increase in the annealing temperature, agglomeration of ZnO nanoparticles resulted a decrease in particle surface area. Larger surface area is beneficial for higher photocatalytic activity. With increasing annealing temperature an increase in supersaturation of the reaction products, which accelerated the crystal core forming reaction within a short time, increase nucleation rate of ZnO nanoparticles. With the temperature continuing to rise, the phenomenon of “nuclear- agglomeration” caused by the rapid formation of crystal nucleus results in agglomeration among the crystal nucleus and then is followed by crystal growth. The rate of particle agglomeration is a major factor that controls the morphology and structure of the final products [134].

Elemental compositions and particle size distribution of the ZnO nanoparticles annealed at different temperatures are shown in Figure 4.5. EDX data for ZnO nanoparticles annealed at different temperature, show that ZnO nanoparticles were composed of only Zn and O in all the samples, no evidence of other impurities was found. This observation was in good agreement with XRD results, which confirmed the phase purity of ZnO nanoparticles. From the particle size distribution, it is evident that ZnO nanoparticles annealed at lower temperatures (400^oC and 500^oC) were densely distributed and standard error was found very small. At higher annealing temperatures (600^oC and 700^oC), particles were diffusely distributed and standard error was increased. Highest standard error of 3.58 was observed for ZnO nanoparticles annealed at 700^oC whereas lowest standard error of 0.416 was found for ZnO nanoparticles annealed at 400^oC. Average particle size and standard error was explored by curve fitting by using Originpro software.

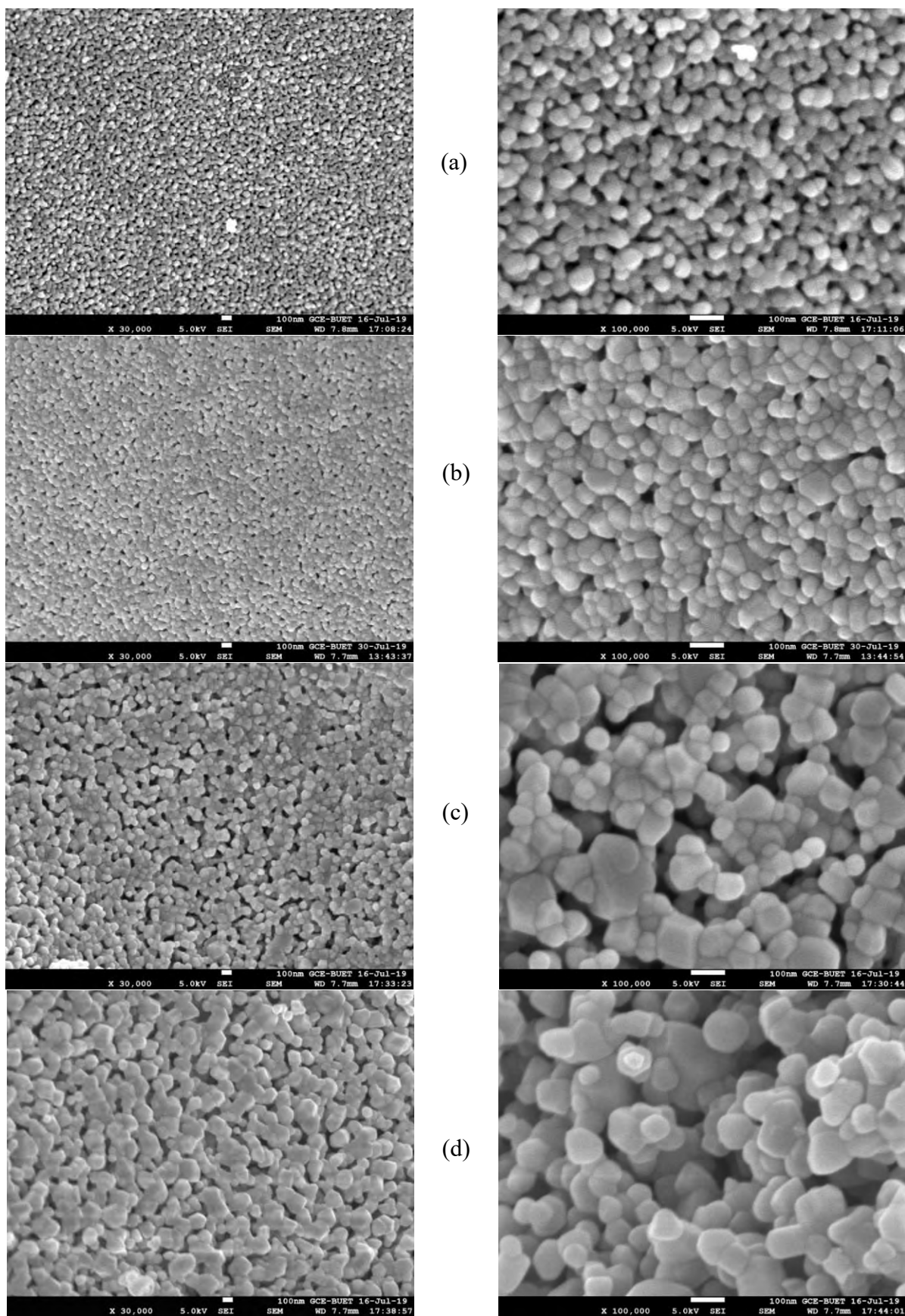
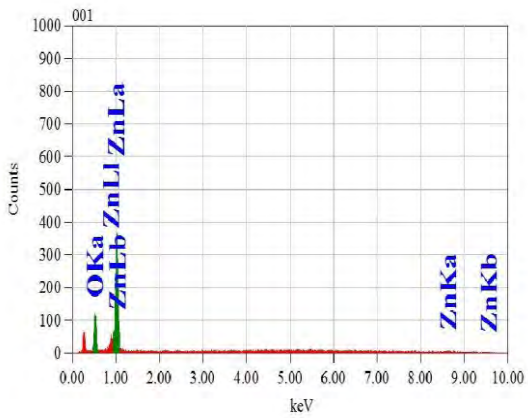
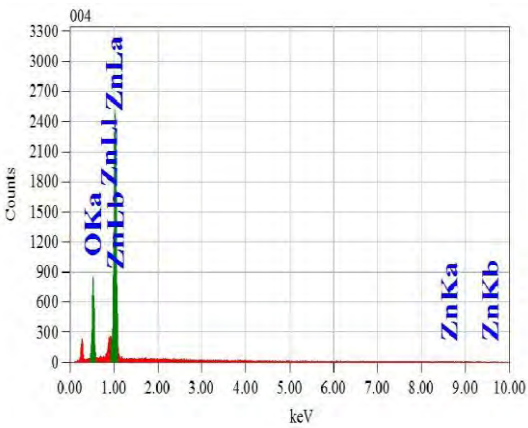
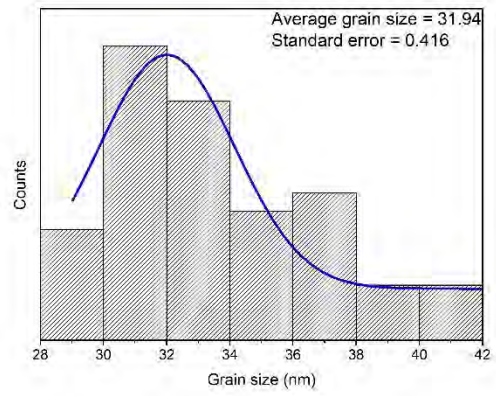


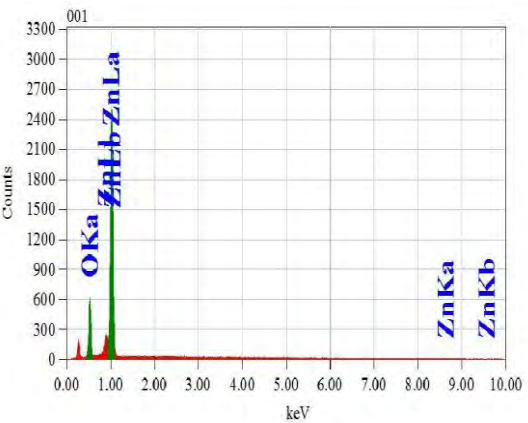
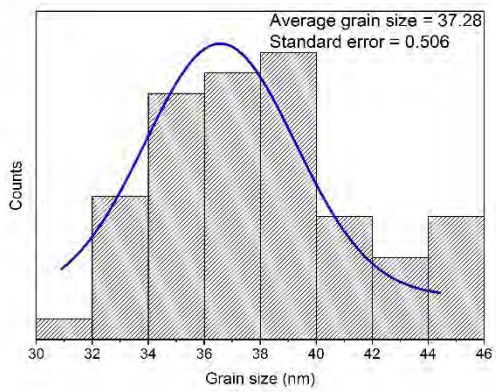
Figure 4.4 Morphology of ZnO nanoparticles (at 30,000X and 1,00,000X) at different annealing temperatures: (a) 400°C, (b) 500°C, (c) 600°C, (d) 700°C



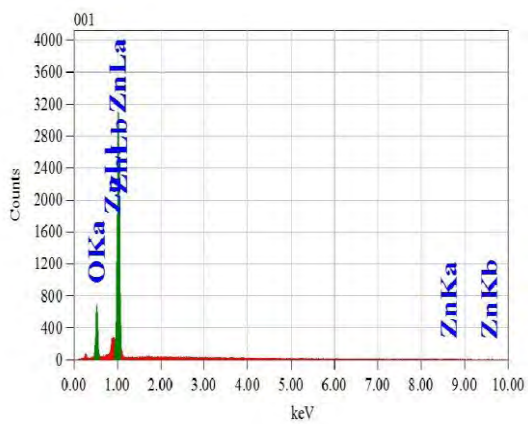
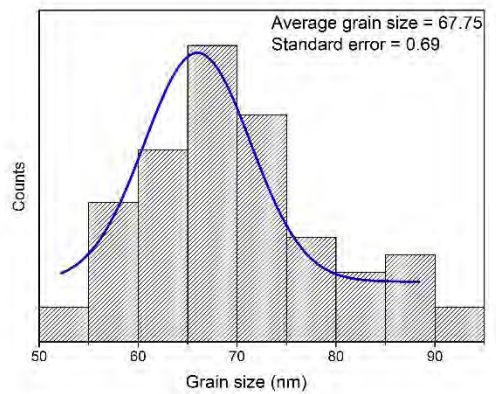
(a)



(b)



(c)



(d)

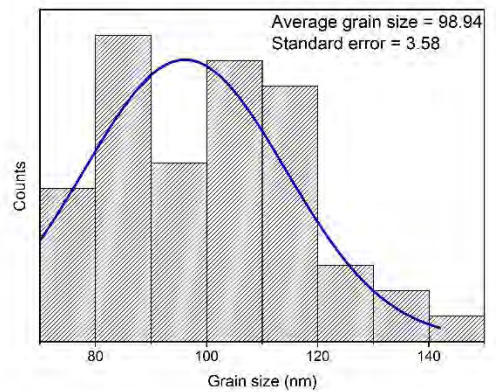


Figure 4.5 Elemental analysis and particle size distribution of ZnO nanoparticles at different annealing temperatures: (a) 400°C, (b) 500°C, (c) 600°C, (d) 700°C

4.1.3 UV-vis DRS Spectra for Different Annealing Temperatures

Figure 4.6 shows diffuse reflectance spectra of ZnO nanoparticles annealed at different temperatures. Average reflectance around 72%, 80%, 86% and 91% was observed in the wavelength region of 370–520 nm for ZnO nanoparticles annealed at 400°C, 500°C, 600°C and 700°C, respectively. Increasing reflectance with increase in annealing temperature can be attributed to the higher scattering ability of larger size particles [135]. So, smaller nanoparticles annealed at lower temperatures (400°C and 500°C) should have better absorbance property. Optical band gap of all the samples was calculated from diffuse reflectance spectra using Kubelka-Muck formula from the eqs. (26-27)

$$F(R_{\infty}) = \frac{A(h\nu - E_g)^n}{h\nu} \quad (26)$$

$$F(R_{\infty}) = \frac{(1 - R_{\infty})^2}{2R_{\infty}} \quad (27)$$

Where,

R_{∞} = Ratio between the diffuse reflectance from the sample and a reference material (in this study, BaSO₄)

A = Constant

$h\nu$ = Incident photon energy

n = 1/2 or 2 for undirected and direct transitions, respectively

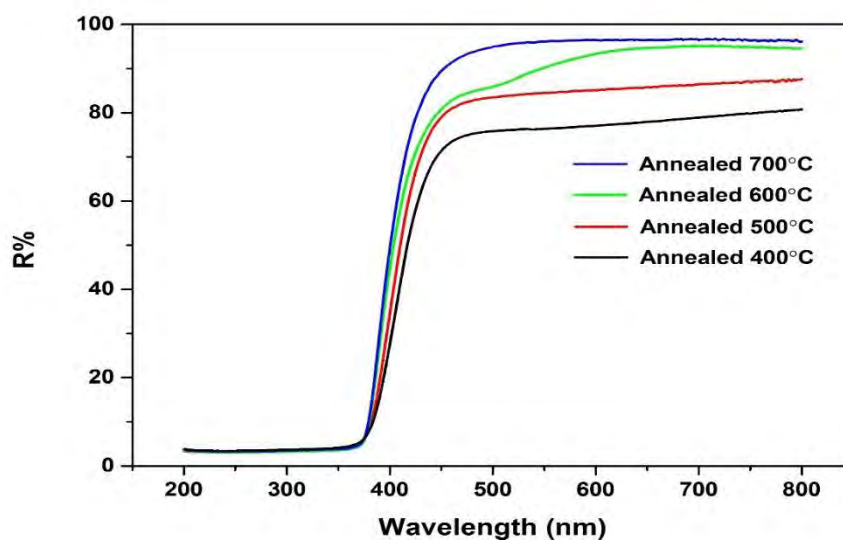


Figure 4.6 Progressive increase in reflectance with increasing annealing temperature

The value of direct band-gap, E_g for each sample was obtained by extrapolating the linear portion of the plot of $\{F(R_\infty) \cdot hv\}^2$ vs. (hv) to intersect hv axis (Figure 4.7). Band gap was calculated 3.257, 3.252, 3.248 and 3.23 eV for ZnO nanoparticles annealed at 400°C, 500°C, 600°C and 700°C, respectively. A decrease in band gap was observed with increasing annealing temperature due to increase in particle size [41].

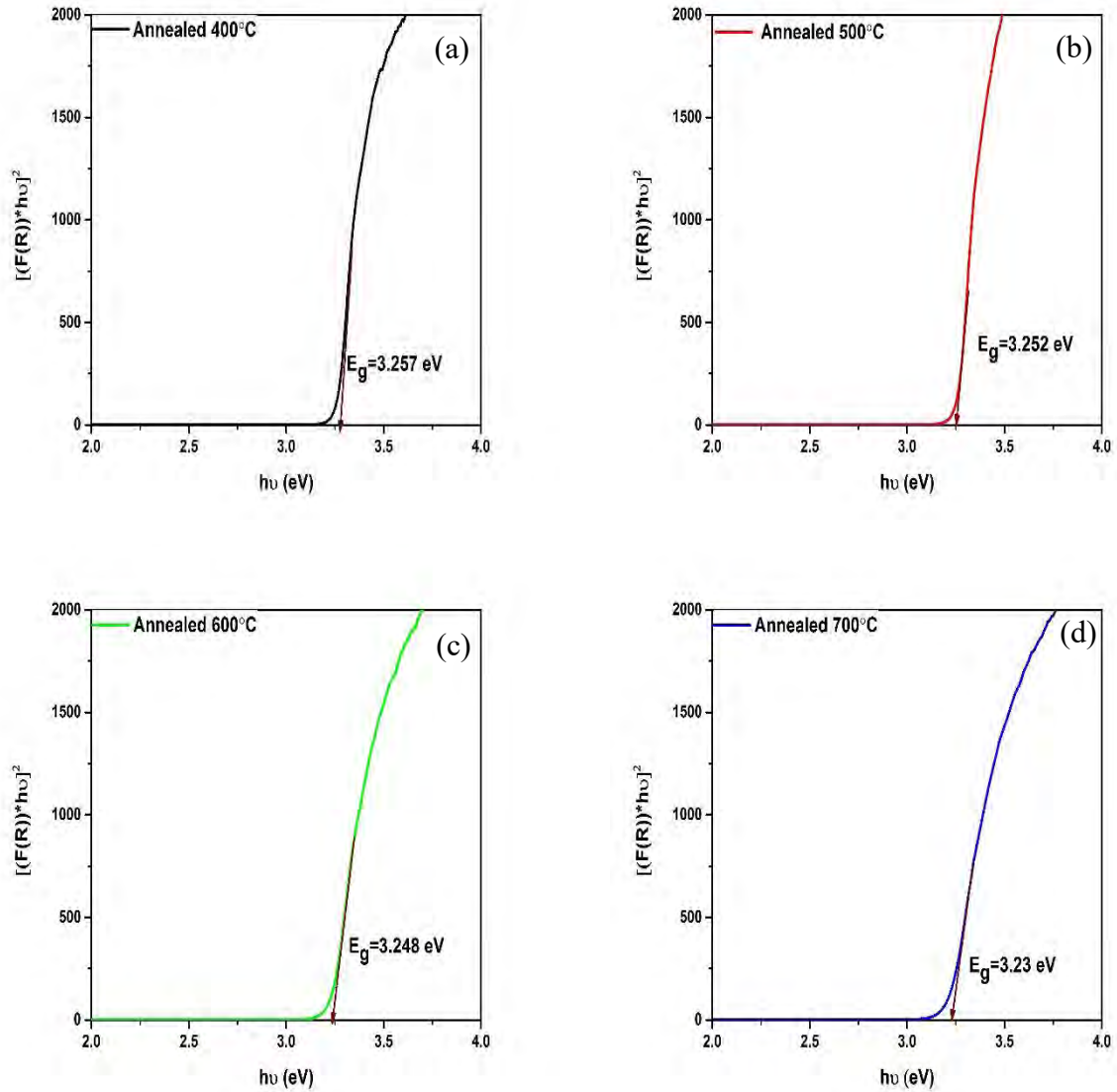


Figure 4.7 Progressive decrease in band gap with increasing annealing temperature: (a) 400°C, (b) 500°C, (c) 600°C, (d) 700°C

4.1.4 Photoluminescence Emission Spectra for Different Annealing Temperatures

Figure 4.8 shows the PL spectra of ZnO nanoparticles annealed at different temperatures using 200 nm UV light as excitation wavelength. In this spectrum, the ZnO nanoparticles contain a UV emission band at around 396 nm, and a strong-broad orange emission band occurs at around 595 nm. The near band emission of 396 nm was due to the recombination of a photogenerated hole with an electron occupying the oxygen vacancies in ZnO nanoparticles. On the other hand, the strong orange emission (595 nm) resulted primarily from intrinsic defects. The intrinsic defects are associated with deep level emissions such as oxygen vacancies or zinc interstitials. Notably, the oxygen vacancies and interstitials were induced by annealing and sol-gel method [135].

The intensity of the UV emission peak increased when the annealing temperature was raised from 400 to 700°C. A low PL spectra intensity at 396 nm for ZnO nanoparticles annealed at lower temperature (400°C and 500°C), indicates the lower rate of the recombination between photogenerated holes and electrons on the surface of the ZnO nanoparticles. So, ZnO nanoparticles annealed at lower temperature are beneficial for the photocatalytic reaction compared to ZnO annealed at higher temperature (600°C and 700°C).

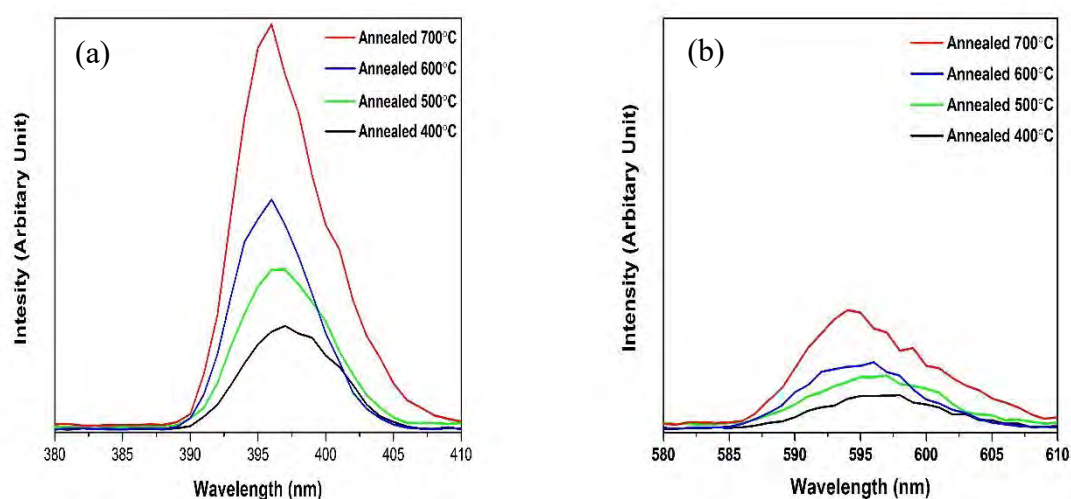


Figure 4.8 PL emission spectra showing (a) near band gap emission and (b) orange band emission at different annealing temperatures

4.1.5 DSC and TGA for Synthesized Non-annealed ZnO

Figure 4.9 shows a combined plot of DSC and TGA for Synthesized Non-annealed ZnO. TGA gives information on the stability of ZnO in the event of the decomposition of several constituents during heating. Whereas, DSC gives information on the structural transformation that occurs in the sample due to changes in heat flow. DSC spectra of the sample consists of two endothermic peaks and two exothermic peaks as observed in the heating profile. First endothermic peak at 110°C corresponds to the evaporation of water. Around 14.4% weight was lost due to evaporation of water. Second endothermic peak at 207°C was attributed to the decomposition of citric acid. Due to this decomposition, around 4.1 % weight was lost. Multistage decomposition of Zinc nitrate occurred till 480°C. Exothermic peaks around 308°C was attributed to this decomposition process. Further 61.5% weight was lost during that period. Exothermic peaks around 427°C corresponded to crystallization of ZnO nanoparticles. After 480°C a stable plateau was observed. The stable plateau at the final heating was indicative of the crystallization of ZnO.

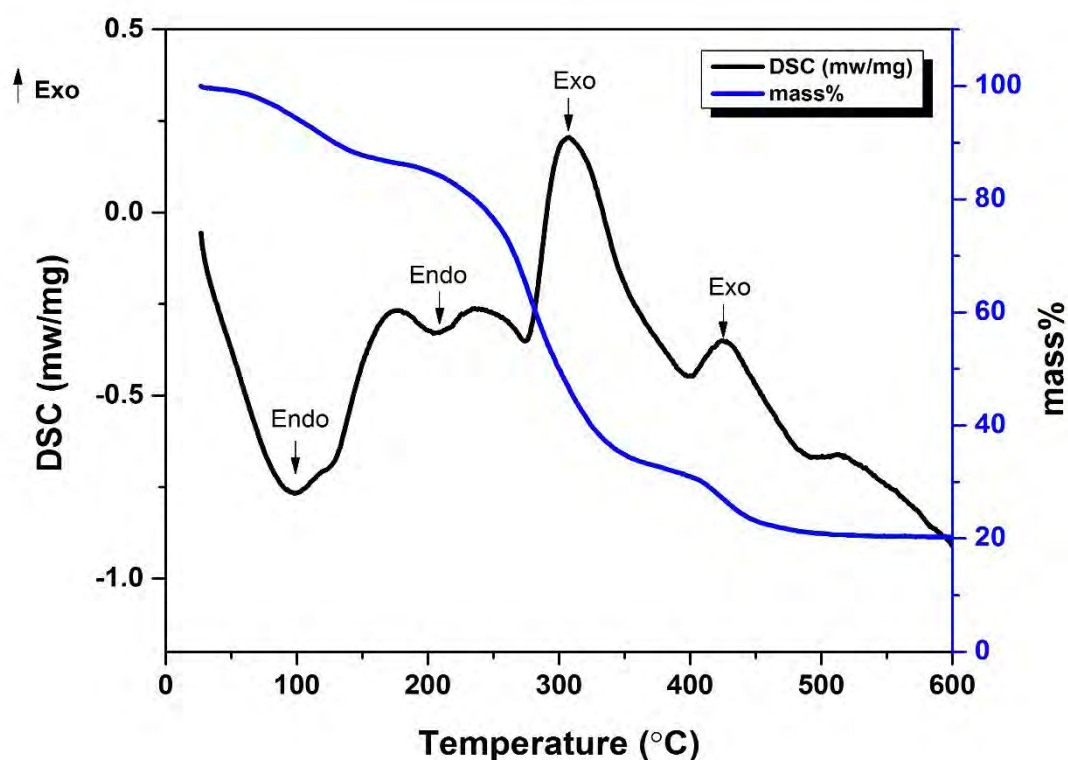


Figure 4.9 Combined DSC and TGA plot showing exothermic and endothermic reactions along with weight changes during heating

4.1.6 Photocatalytic Activity Measurement for Different Annealing Temperatures

Figure 4.10 shows absorption spectra of methyl blue in different time intervals under radiation of UV light for ZnO nanoparticles annealed at 500°C and 600°C. It is evident that the strong absorption peak of chromophoric group of MB solution at 665 nm steadily decreased under UV radiation in both cases. The decrease in absorbance intensity of MB by ZnO nanoparticles annealed at 500°C was faster than that of ZnO nanoparticles annealed at 600°C. ZnO nanoparticles annealed at 500°C showed 89.4% degradation compared to 62.1% degradation for annealing temperature 600°C after 4 hours irradiation. So, it is evident that ZnO nanoparticles annealed at 500°C exhibits better photocatalytic degradation of dye under UV illumination. The degradation efficiency was calculated by the Eq. (28)

$$\text{Degradation efficiency \%} = \frac{C_0 - C}{C_0} * 100\% = \frac{A_0 - A}{A_0} * 100\% \quad (28)$$

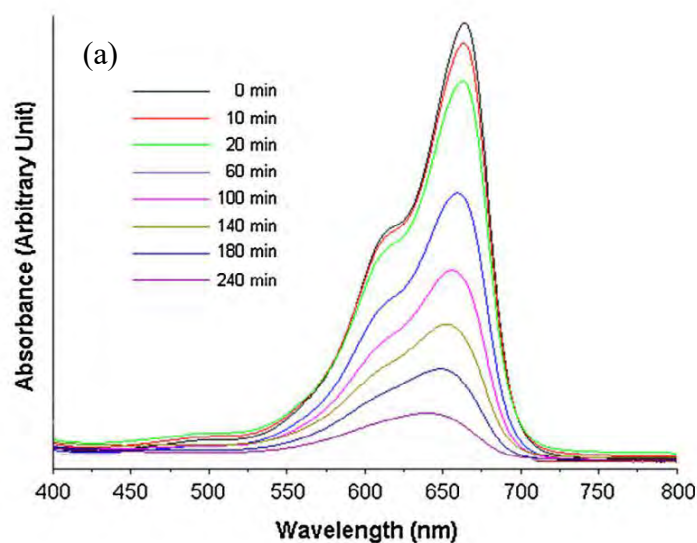
Where,

C_0 = Initial concentrations of dye

C = Final concentrations of dye

A_0 = Initial absorptions of dye

A = Final absorption of dye



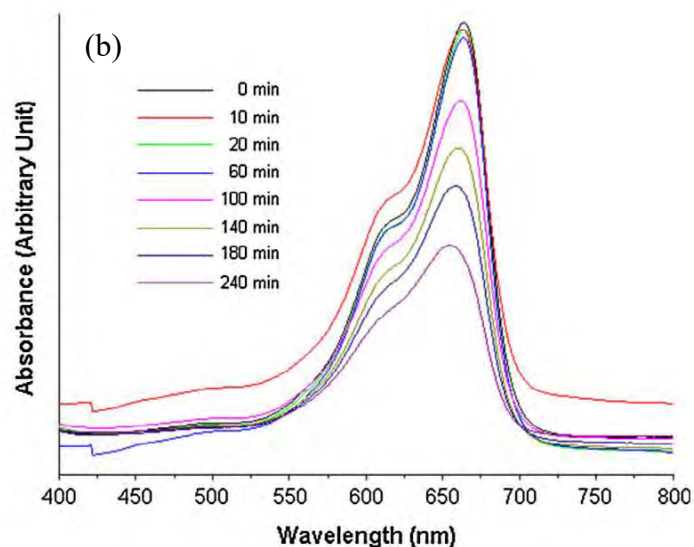


Figure 4.10 Variation of the absorption spectra for MB solution in the presence of ZnO annealed at (a) 500^oC and (b) 600^oC under UV light at different time intervals

Better photocatalytic activity was observed for ZnO nanoparticles annealed at 500^oC. Larger surface area of the nanoparticles 500^oC results greater adsorption of MB molecules at surface of the finer particles leading to higher photocatalytic activity. High photocatalytic activity of ZnO nanoparticles annealed at 500^oC can also be attributed to the lower rate of electron-hole recombination as obtained for PL spectra (Figure 4.8). As particle size increases, electron-hole recombination occurs before electron jumps to the particle surface [135].

4.1.7 Selection of Annealing Temperature

Synthesized non-annealed ZnO showed crystallization peak around 427^oC and weight loss was continued till 480^oC (evident from DSC and TGA). So, annealing temperature of 400^oC cannot be selected. ZnO nanoparticles annealed at higher temperature (600^oC and 700^oC) showed bigger particle size with agglomeration (evident from SEM micrographs) resulted in reducing effective surface area which is unfavorable for photocatalytic activity. Moreover, higher reflectance and recombination rate (evident from DRS spectra and PL spectra) were observed in ZnO nanoparticles annealed at higher temperature (600^oC and 700^oC), which is again not suitable for photocatalytic activity. Lastly, from the photocatalytic activities of ZnO nanoparticles annealed at 500^oC and 600^oC, it is clearly evident that ZnO nanoparticles annealed at 500^oC showed better photodegradation ability due to smaller size, better dispersion

and lower electron-hole combination rate. By considering above facts, annealing temperature of 500°C was selected for doping purpose.

4.2 OPTIMIZATION OF CHELATING AGENT

4.2.1. XRD for Different Chelating Agent Ratios

Figure 4.11 shows XRD patterns of ZnO nanoparticles annealed at 500°C having different precursor to citric acid ratios. As no significant change in peak position was observed, so the diffraction data are in good agreement with the JCPDS card for ZnO. Major diffraction peak (002) plane increased slightly with increasing precursor to acid ratio, which resulted in a slight increase in the crystalline quality (evident from figure 4.12).

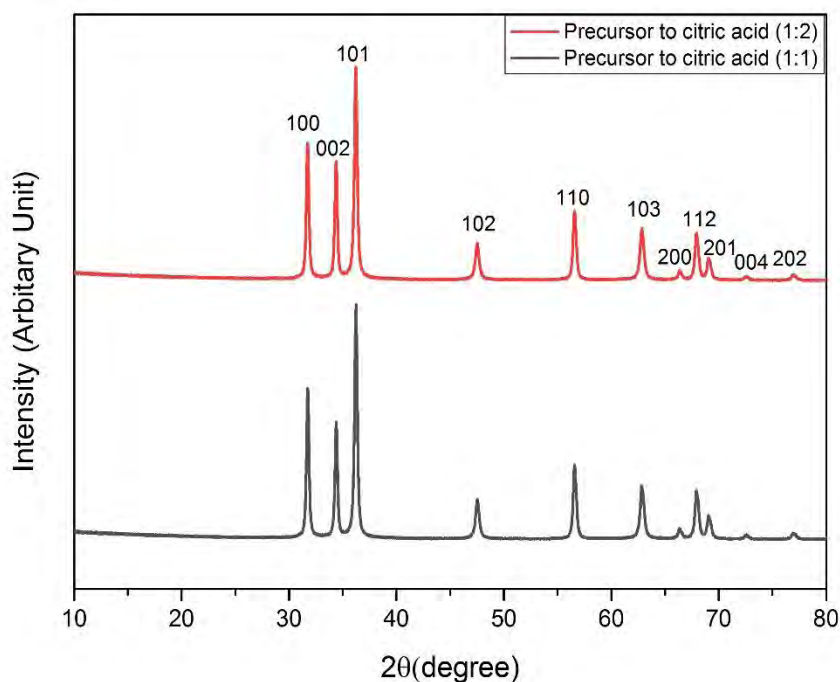


Figure 4.11 XRD patterns showing crystalline structure of ZnO nanoparticles at different precursor to citric acid ratios

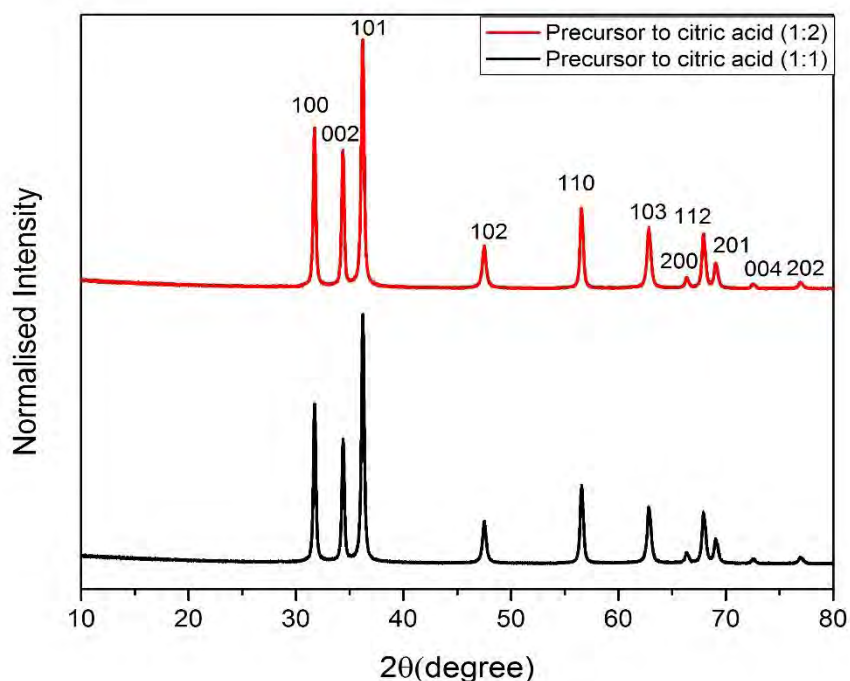


Figure 4.12 XRD patterns showing increasing crystallinity of ZnO nanoparticles at different precursor to citric acid ratios (normalized XRD patterns)

4.2.2. SEM for Different Chelating Agent Ratios

Figure 4.13 exhibits morphological images of ZnO nanoparticles at different precursor to citric acid ratios. Bimodal particles were observed for ZnO nanoparticles having precursor to citric acid ratio of 1:1 (evident from Figure 4.13). Average size of large particles was around 183.43 nm and average size of small particles was 37.03 nm for ZnO nanoparticles having precursor to citric acid ratio of 1:1. Whereas, the average particle size 37.28 nm was found for ZnO nanoparticles having precursor to citric acid ratio of 1:2. Particle size distribution of ZnO nanoparticles at different precursor to citric acid ratios is shown in Figure 4.14. Randomly distributed particles was observed for precursor to citric acid ratio of 1:1, which might not be favorable for photocatalytic activity. So, precursor to citric acid ratio of 1:2 was selected due its homogenous distribution of particles.

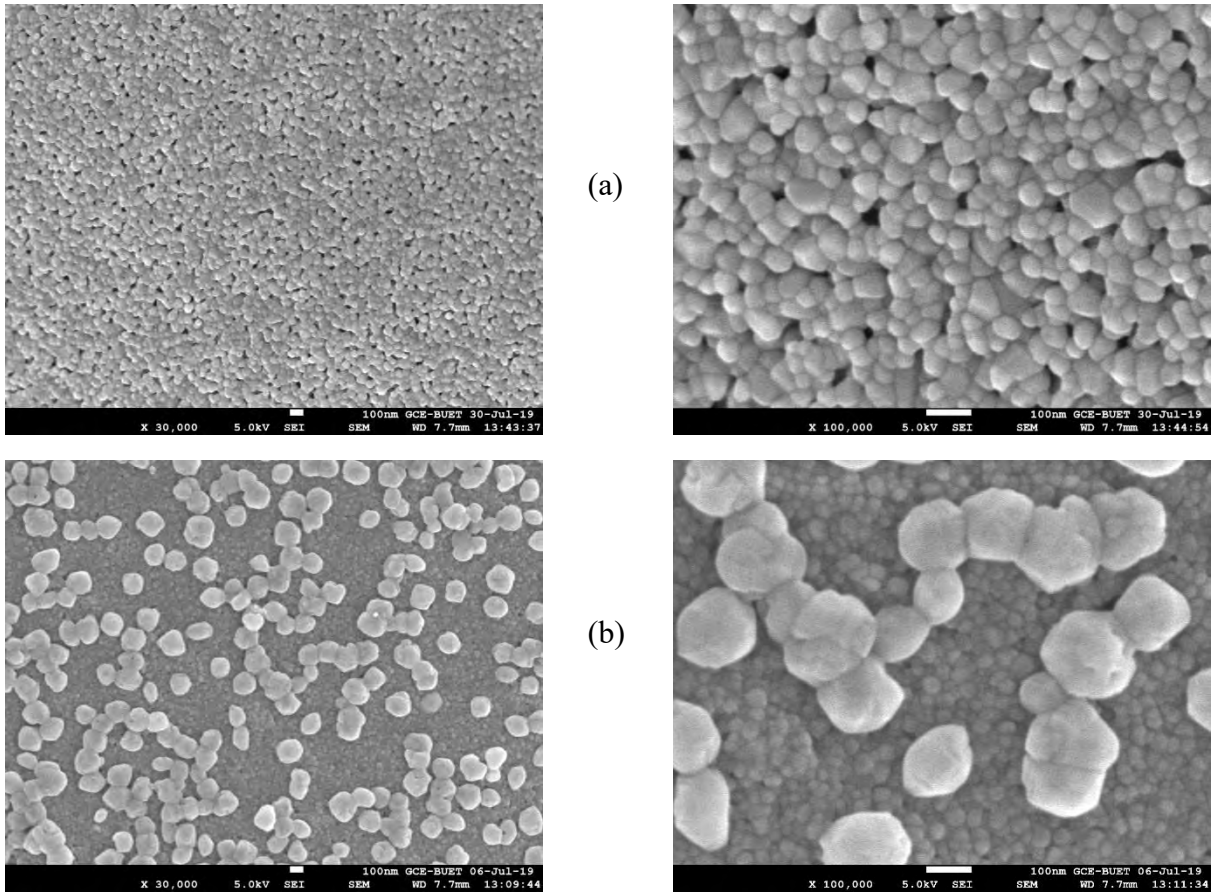


Figure 4.13 Morphology of ZnO nanoparticles (at 30,000X and 1,00,000X) at different precursor to citric acid ratios: (a) 1:1 and (b) 1:2

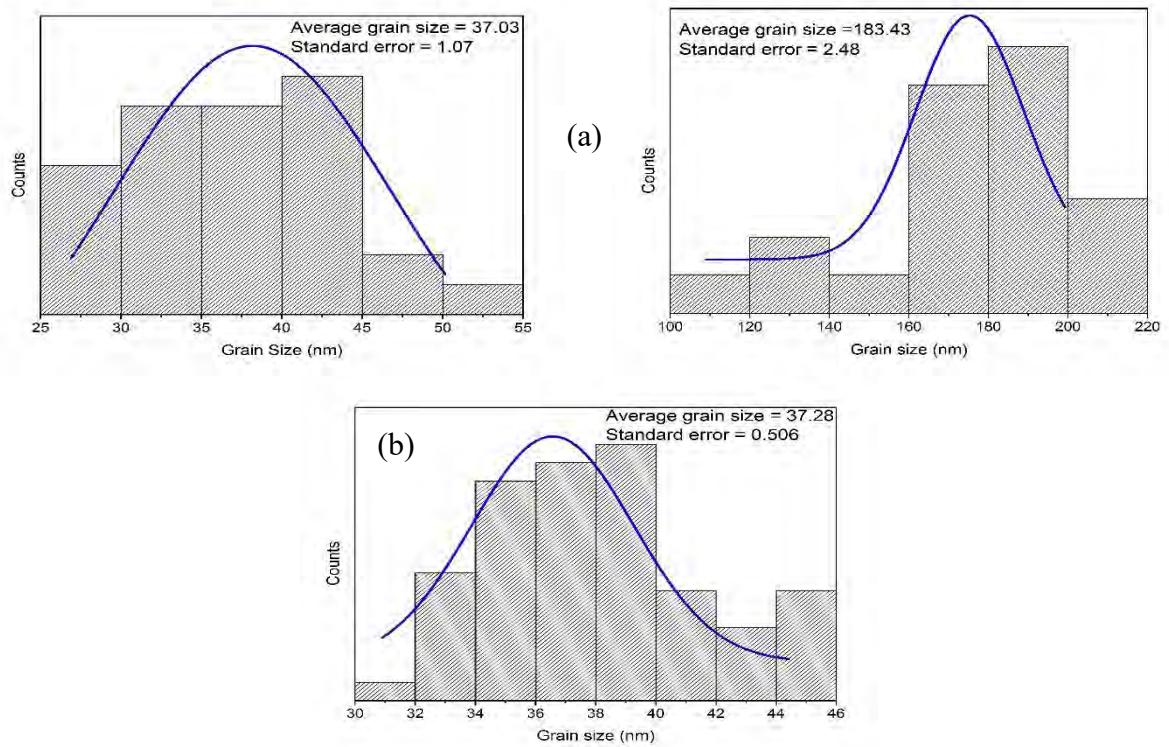


Figure 4.14 Particle size distribution of ZnO nanoparticles at different precursor to citric acid ratios: (a) 1:1 and (b) 1:2

4.3 EFFECT OF RARE-EARTH DOPANTS

4.3.1 XRD for Doped ZnO Nanoparticles

Figure 4.15 and 4.16 show XRD patterns of ZnO nanoparticles annealed at 500°C having different Ho concentrations (Ho = 1-5 mol%) and Sm concentrations (Sm = 1-5 mol%), respectively. No diffraction peaks of secondary phases such as Ho₂O₃ and Sm₂O₃ were observed in the diffraction patterns suggesting complete incorporation of Ho³⁺ and Sm³⁺ ions into ZnO matrix. From normalized XRD patterns (Figure 4.17 and 4.18), it is evident that the major diffraction peak (002) decreased with increasing doping concentration in both the cases which indicates decreased in crystallinity due to Ho and Sm doping. Decrease in crystallinity was resulted from the substitute of Zn²⁺ (ionic radius of 0.74 Å) by Ho³⁺ (ionic radius of 1.04 Å) and Sm³⁺ (ionic radius of 1.09 Å) which created lattice disorder in crystal [66-67]. Crystallinity was decreased from 81.2% for pristine ZnO nanoparticles to 68.6% for 5 mol% Ho doping. Meanwhile, for Sm-doped nanoparticles crystallinity was decreased to 70% for 5 mol% doping. The position of the (002) peak of Ho- and Sm-doped ZnO nanoparticles were shifted towards lower angle with respect to that of pure ZnO nanoparticles (Figure 4.19 and 4.20). Since the ionic radius of both the Ho and Sm are larger than that of Zn, doping of Ho and Sm into ZnO lattice increased the lattice constant (c/a) and, therefore, lead the diffraction peak (002) towards a lower diffraction angle.

XRD data of all doped ZnO Nanoparticles were analyzed and showed in Table 4.6-4.11. Lattice parameters were obtained by rietveld analysis using Highscore Plus software and summarized in Table 4.12 and 4.13. An increase in the value of full width at half maximum was observed for the all planes with increasing doping concentration in both the cases. As FWHM increased with increasing doping concentration, crystallite size was decreased. Meanwhile, large amount of dopants resulted in lattice disorder, which was associated with the stress generation and thus micro-stain increases with increasing doping concentration in both the cases. Crystallite size and micro-strain values were obtained during rietveld analysis and showed in Table 4.6-4.11. Average crystallite size was decreased from 28.8 nm for undoped ZnO to 11.7 nm for 5 mol% Ho doping. Similarly, for Sm-doped ZnO nanoparticles average crystallite size was decreased to 13 nm for 5 mol% doping. The decrease in the crystallite size of Ho- and Sm-doped ZnO nanoparticles is mainly attributed to the formation of Ho–O–Zn and Sm–O–Zn, respectively, on the surface of the doped products, which inhibited the growth of crystal grains. Similar

inhibitory effect was also reported in ZnO doped with various rare earth elements [68]. Meanwhile, for Ho-doped ZnO nanoparticles average micro-strain was increased from 0.31 for undoped to 0.77 for 5 mol% doping. Whereas, average micro-strain was increased to 0.69 for 5 mol% Sm doping.

Table 4.13 and 4.14 show, (c/a) ratio was increased from 1.6024 for undoped ZnO to 1.6041 after 5 mol% Ho doping. For Sm-doped ZnO nanoparticles (c/a) ratio was increased to 1.6037. Increasing the value of (c/a) with increasing doping concentration is in well agreement with increasing micro-strain of the progressively higher doped ZnO nanoparticles. Increasing Ho and Sm concentrations exhibit almost similar changes in crystal structure, crystallite size and lattice parameters to a slightly different extent due to difference in ionic radius of Ho^{3+} and Sm^{3+} ions.

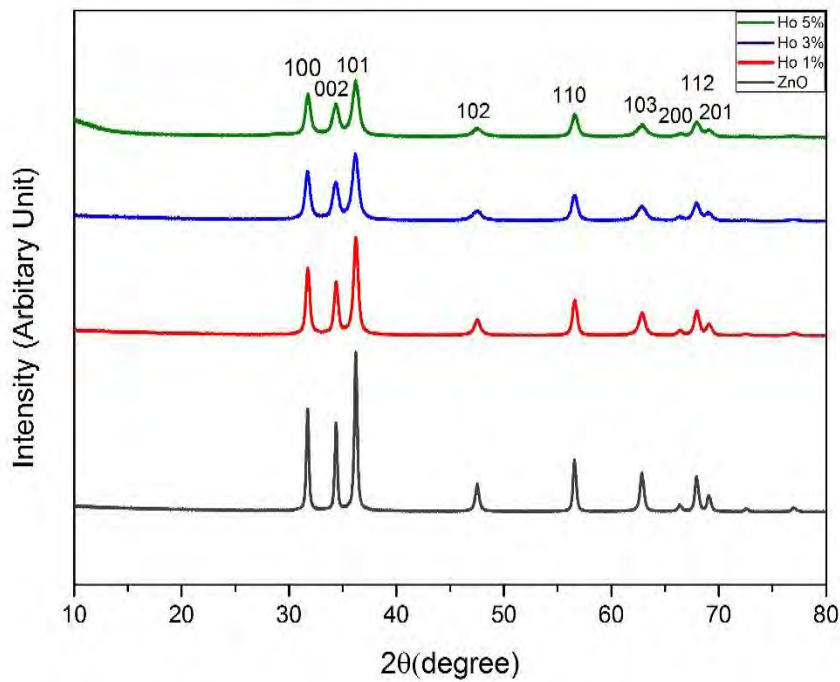


Figure 4.15 XRD patterns showing crystalline structure of ZnO nanoparticles at different Ho concentrations

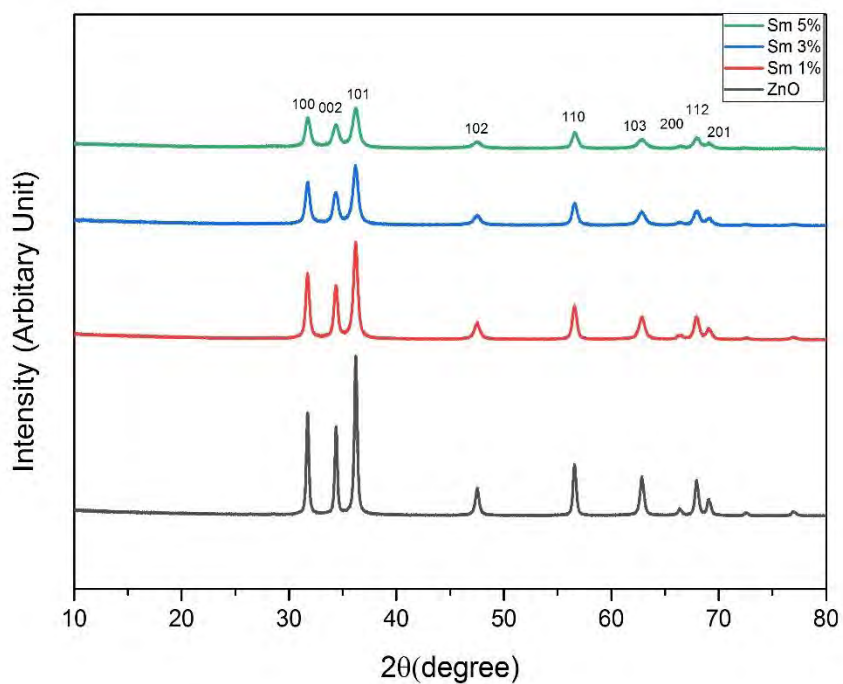


Figure 4.16 XRD patterns showing crystalline structure of ZnO nanoparticles at different Sm concentrations

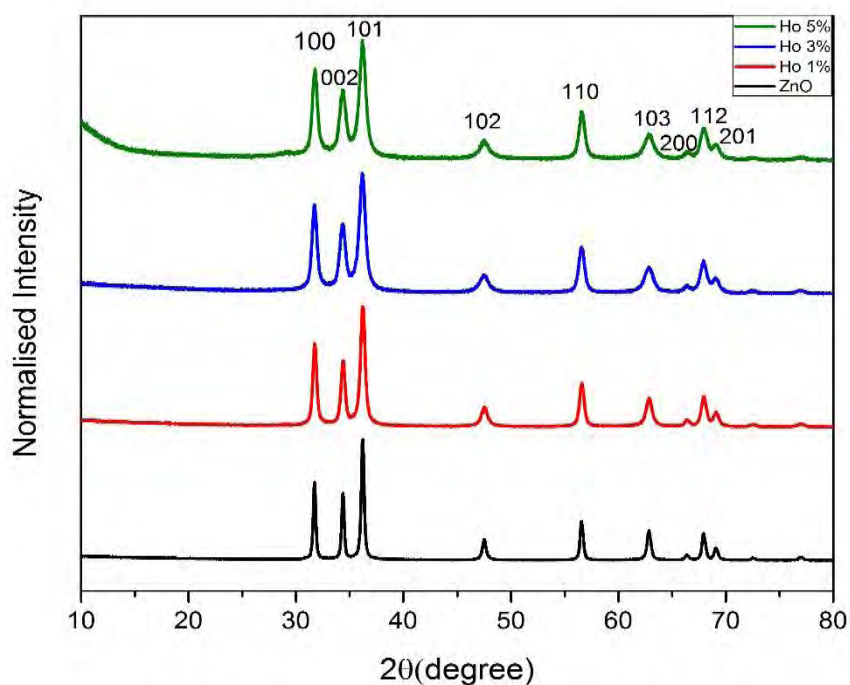


Figure 4.17 XRD patterns showing decreasing crystallinity of ZnO nanoparticles at different Ho concentrations (normalized XRD patterns)

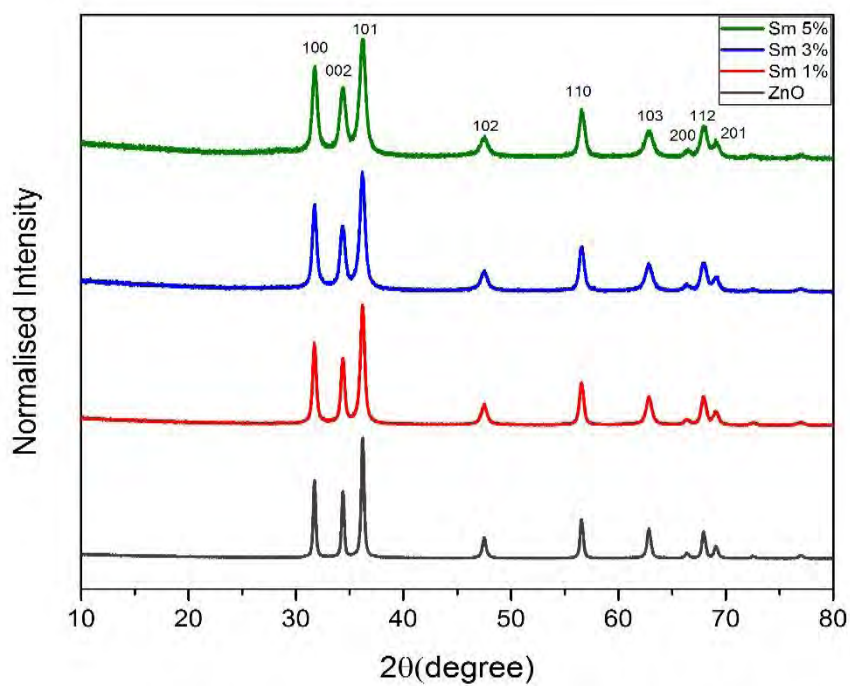


Figure 4.18 XRD patterns showing decreasing crystallinity of ZnO nanoparticles at different Sm concentrations (normalized XRD patterns)

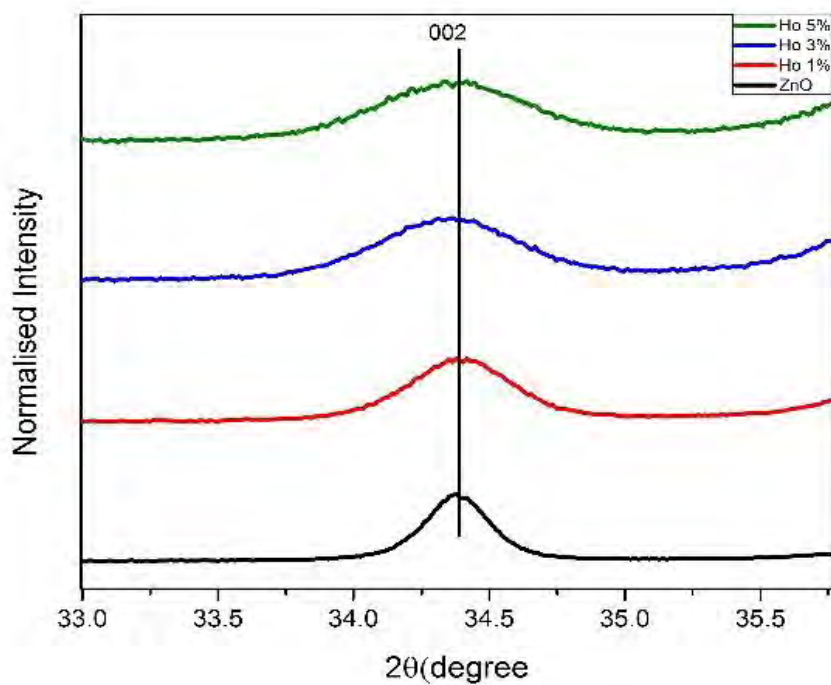


Figure 4.19 XRD patterns showing peak shift of (002) plane of ZnO nanoparticles at different Ho concentrations (normalized XRD patterns)

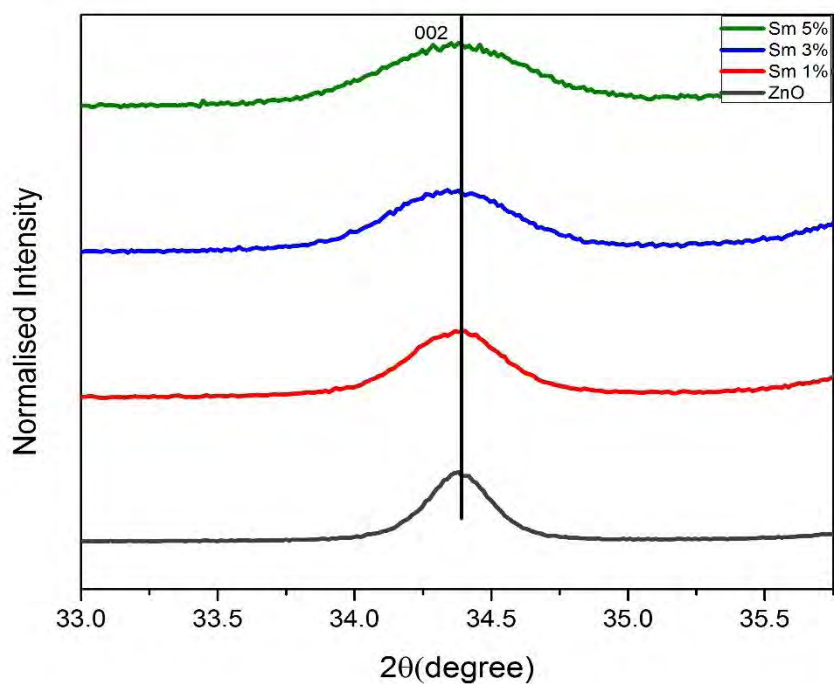


Figure 4.20 XRD patterns showing peak shift of (002) plane of ZnO nanoparticles at different Sm concentrations (normalized XRD patterns)

Table 4.6 XRD data analysis 1 mol% Ho-doping

Peak No	Peak position(2θ) (degree)	d-spacing (Å)	FWHM (degree)	Crystallite size (nm)	Micro-strain (%)	hkl
1	31.7228	2.81839	0.4693	17.4	0.81167	100
2	34.3609	2.60781	0.474	17.3	0.75438	002
3	36.2044	2.47914	0.4775	17.2	0.71935	101
4	47.4825	1.91328	0.502	16.9	0.56476	102
5	56.5506	1.6261	0.5264	16.7	0.48559	110
6	62.7912	1.47866	0.546	16.6	0.44453	103
7	66.332	1.40805	0.5583	16.6	0.4247	200
8	67.8947	1.3794	0.564	16.6	0.41661	112
9	69.0404	1.35928	0.5683	16.5	0.41092	201
10	72.4868	1.3029	0.5819	16.5	0.39488	004
11	76.9079	1.23865	0.6008	16.5	0.37644	202

- Average crystallite size 16.6 nm and average microstrain 0.53
- Crystallinity 79.2%

Table 4.7 XRD data analysis 3 mol% Ho-doping

Peak No	Peak position(2 θ) (degree)	d-spacing (Å)	FWHM (degree)	Crystallite size (nm)	Micro-strain (%)	hkl
1	31.6882	2.82139	0.6271	12.9	1.09117	100
2	34.3164	2.61108	0.6323	12.9	1.01195	002
3	36.1687	2.4815	0.6362	12.9	0.963	101
4	47.4454	1.91469	0.6628	12.8	0.74697	102
5	56.5254	1.62677	0.6889	12.8	0.63509	110
6	62.7537	1.47945	0.7096	12.8	0.57679	103
7	66.3114	1.40844	0.7227	12.8	0.5483	200
8	67.8684	1.37987	0.7287	12.9	0.53675	112
9	69.0196	1.35964	0.7332	12.9	0.52853	201
10	72.4441	1.30357	0.7475	12.9	0.50559	004
11	76.8868	1.23894	0.7676	12.9	0.47879	202

- Average crystallite size 12.9 nm and average microstrain 0.69
- Crystallinity 74.6%

Table 4.8 XRD data analysis 5 mol% Ho-doping

Peak No	Peak position(2 θ) (degree)	d-spacing (Å)	FWHM (degree)	Crystallite size (nm)	Micro-strain (%)	hkl
1	31.7223	2.82139	0.6626	11.5	1.22057	100
2	34.3327	2.61108	0.6664	11.6	1.12956	002
3	36.1981	2.4815	0.6694	11.6	1.07262	101
4	47.464	1.91469	0.6914	11.6	0.82464	102
5	56.5559	1.62677	0.715	11.7	0.69739	110
6	62.758	1.47945	0.7347	11.7	0.63217	103
7	66.34	1.40844	0.7476	11.7	0.60022	200
8	67.886	1.37987	0.7536	11.7	0.58751	112
9	69.0449	1.35964	0.7582	11.8	0.57836	201
10	72.4299	1.30357	0.7724	11.8	0.55341	004
11	76.9029	1.23894	0.7932	11.8	0.52397	202

- Average crystallite size 11.7 nm and average microstrain 0.77
- Crystallinity 68.6%

Table 4.9 XRD data analysis 1 mol% Sm-doping

Peak No	Peak position(2 θ) (degree)	d-spacing (Å)	FWHM (degree)	Crystallite size (nm)	Micro-strain (%)	hkl
1	31.6924	2.82103	0.4321	17.6	0.80309	100
2	34.3345	2.60975	0.4369	17.7	0.73803	002
3	36.1752	2.48107	0.4405	17.8	0.69812	101
4	47.4564	1.91427	0.4609	18.5	0.5184	102
5	56.5224	1.62685	0.4717	19.2	0.42296	110
6	62.7695	1.47912	0.4825	19.9	0.37178	103
7	66.3051	1.40856	0.4935	20.3	0.34656	200
8	67.8704	1.37983	0.5046	20.5	0.33612	112
9	69.0145	1.35973	0.5089	20.7	0.32874	201
10	72.47	1.30316	0.5321	21.2	0.30763	004
11	76.8848	1.23896	0.5489	21.9	0.28294	202

- Average crystallite size 19.6 nm and average microstrain 0.47
- Crystallinity 79.3%

Table 4.10 XRD data analysis 3 mol% Sm-doping

Peak No	Peak position(2 θ) (degree)	d-spacing (Å)	FWHM (degree)	Crystallite size (nm)	Micro-strain (%)	hkl
1	31.6913	2.82113	0.5732	14.4	0.98064	100
2	34.315	2.61119	0.5882	14.5	0.90167	002
3	36.1709	2.48135	0.6092	14.6	0.85249	101
4	47.4458	1.91467	0.6281	15.1	0.6332	102
5	56.5301	1.62665	0.6451	15.7	0.51667	110
6	62.7521	1.47949	0.6535	16.3	0.45464	103
7	66.3168	1.40834	0.6643	16.6	0.42374	200
8	67.871	1.37982	0.6767	16.8	0.41115	112
9	69.0244	1.35955	0.6805	16.9	0.40211	201
10	72.4388	1.30365	0.6912	17.3	0.3768	004
11	76.8903	1.23889	0.7014	17.9	0.34662	202

- Average crystallite size 16.1 nm and average microstrain 0.57
- Crystallinity 75%

Table 4.11 XRD data analysis 5 mol% Sm-doping

Peak No	Peak position(2 θ) (degree)	d-spacing (Å)	FWHM (degree)	Crystallite size (nm)	Micro-strain (%)	hkl
1	31.703	2.82011	0.6109	12.8	1.10165	100
2	34.3248	2.61047	0.6149	12.8	1.01976	002
3	36.1834	2.48052	0.6179	12.8	0.96886	101
4	47.4608	1.9141	0.6391	12.8	0.74496	102
5	56.5504	1.62611	0.6608	12.9	0.62889	110
6	62.771	1.47909	0.6783	13.0	0.56854	103
7	66.3411	1.40788	0.6895	13.1	0.53893	200
8	67.8943	1.37941	0.6947	13.1	0.52699	112
9	69.0495	1.35912	0.6986	13.1	0.51845	201
10	72.4594	1.30333	0.7109	13.2	0.49481	004
11	76.9178	1.23852	0.7286	13.3	0.46697	202

- Average crystallite size 13 nm and average microstrain 0.69
- Crystallinity 70%

Table 4.12 Rietveld analysis for Ho-doped ZnO nanoparticles

Ho concentration (mole %)	Lattice Parameter			R _w	R _{exp}	$\chi^2 = R_w/R_{exp}$
	a (Å)	c (Å)	c/a			
0	3.2495	5.2072	1.6024	8.84	4.93	1.79
1	3.2502	5.2094	1.6028	8.74	4.78	1.82
3	3.2495	5.2099	1.6033	8.24	4.62	1.78
5	3.2496	5.2126	1.6041	8.1	4.47	1.80

Table 4.13 Rietveld analysis for Sm-doped ZnO nanoparticles

Sm concentration (mole %)	Lattice Parameter			R _w	R _{exp}	$\chi^2 = R_w/R_{exp}$
	a (Å)	c (Å)	c/a			
0	3.2495	5.2072	1.6024	8.84	4.93	1.79
1	3.2502	5.2089	1.6026	9.32	4.83	1.92
3	3.2493	5.2103	1.6035	7.63	4.88	1.56
5	3.2483	5.2092	1.6037	6.44	4.90	1.31

4.3.2 SEM for Doped ZnO Nanoparticles

Figure 4.21 and 4.22 show the morphological images of pristine ZnO and doped ZnO nanoparticles annealed at 500⁰C for different Ho and Sm concentrations. It is evident from the micrographs that morphology of the doped ZnO nanoparticles changed from spherical for pristine ZnO nanoparticles to rod shape with increasing doping content upto 3 mol% in both cases. Charge anisotropy is the main reason behind this change in morphology [66]. This results in a higher surface area to volume compared to spherical or hexagonal nanoparticles, which is favorable for higher photocatalytic activity. For Ho-doped ZnO nanoparticles, diameter of rod shaped nanoparticles decreased from 25.8 nm for 1 mol% doping to 18.08 nm for 3 mol% doping and then increased to 20.9 nm for 5 mol% doping. Meanwhile, for Sm-doped ZnO nanoparticles, diameter of rod shaped nanoparticles decreased from 26.26 nm for 1 mol% doping to 21.7 nm for 3 mol% doping and then increased to 25.33 nm for 5 mol% doping. So, the diameter of rod shaped nanoparticles decreased with increase in the doping content upto 3 mol% in both cases due differential anisotropic growth rate with increasing doping concentration. When doping concentration was 5 mol%, agglomeration of nanoparticles was observed and effective surface area was reduced. The shape of nanoparticles slightly changed to near spherical nanoparticles at that doping concentration.

Elemental compositions and particle size distribution of Ho- and Sm-doped ZnO nanoparticles along with pristine ZnO nanoparticles are shown in Figure 4.23 and 4.24, respectively. EDX data for Ho-doped ZnO nanoparticles only showed peaks for Zn, O and Ho, no evidence of other impurities was found. Similarly, Sm- doped ZnO nanoparticles only showed peaks for Zn, O and Sm. This observation was in good agreement with XRD results, which confirmed the phase purity of doped ZnO nanoparticles. From the particle size distribution, it is evident that all the doped ZnO nanoparticles were densely distributed.

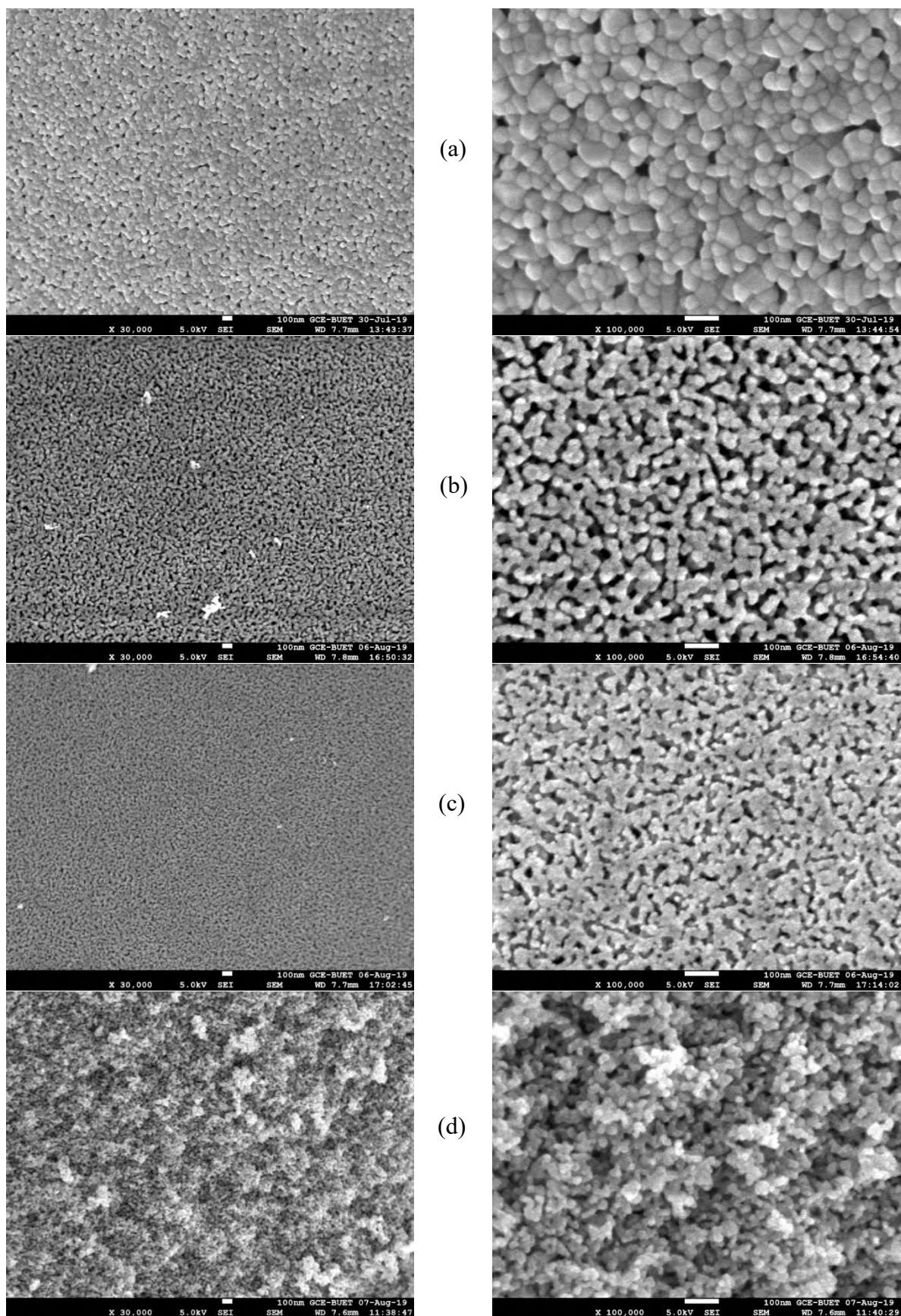


Figure 4.21 Morphology of ZnO nanoparticles (at 30,000X and 1,00,000X) at different Ho Concentrations: (a) pristine, (b) 1 mol% (c) 3 mol% and (d) 5 mol%

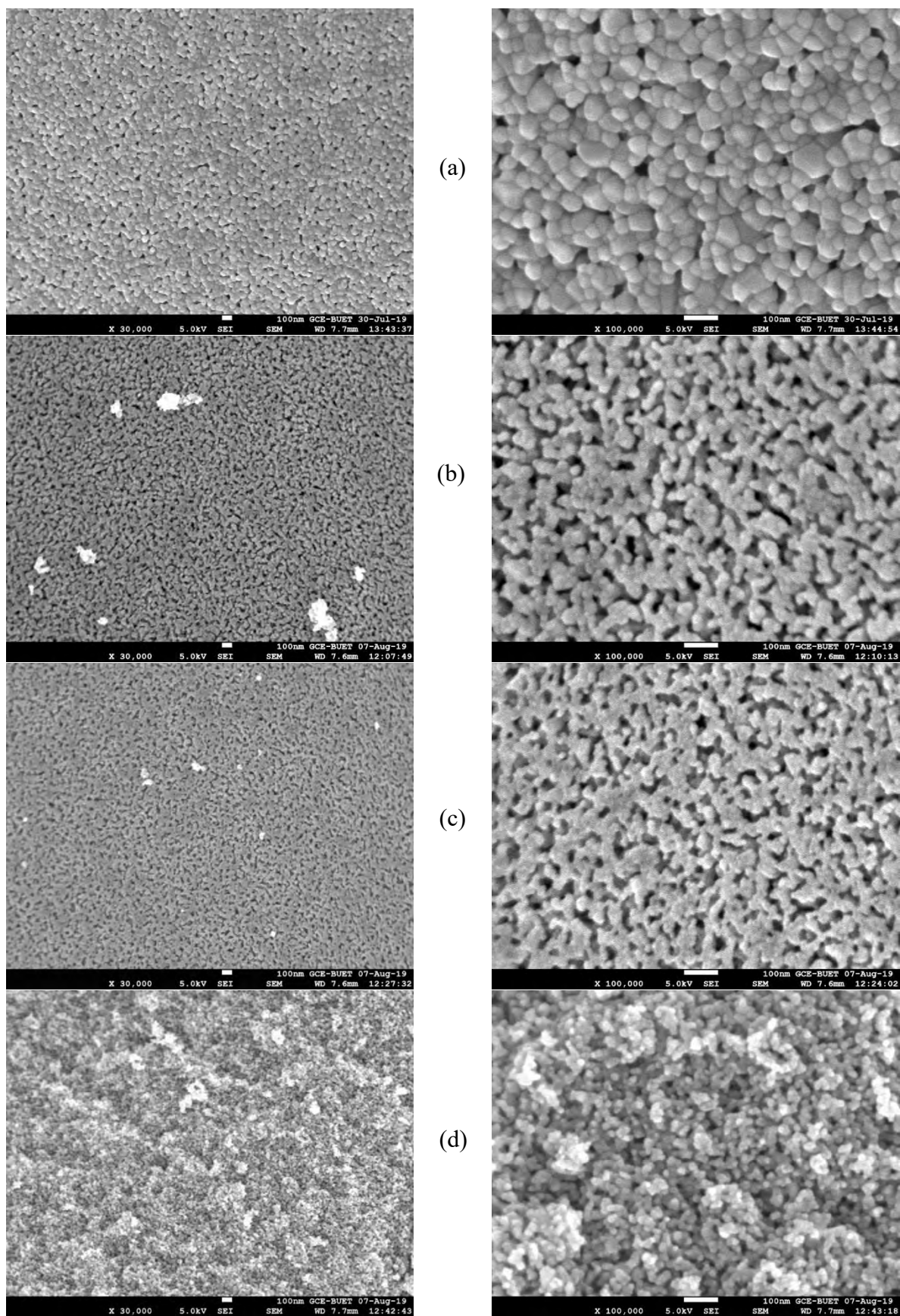
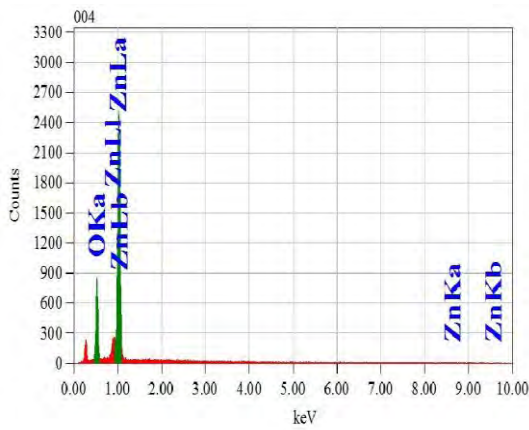
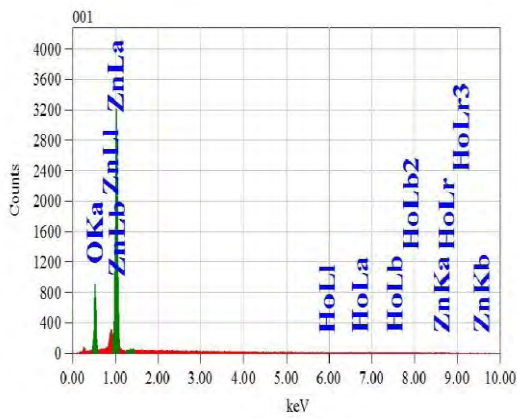
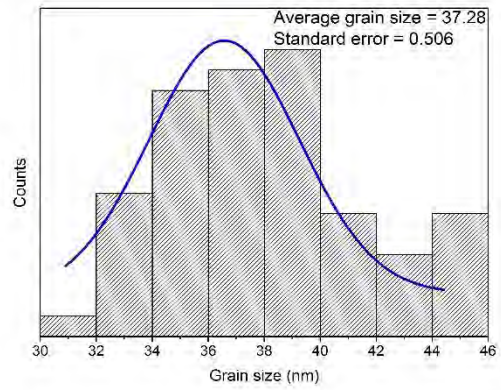


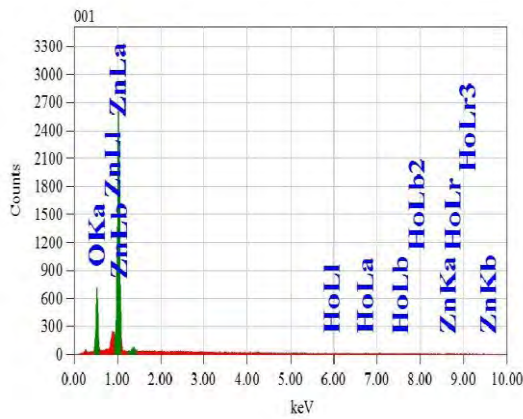
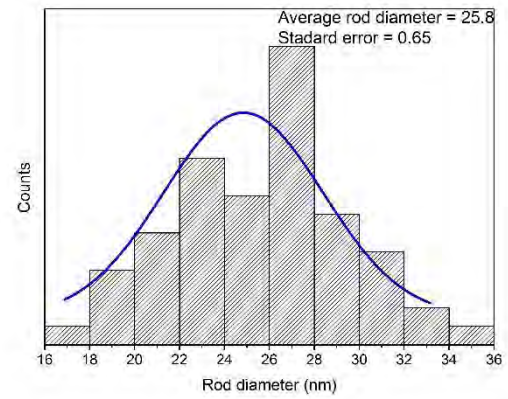
Figure 4.22 Morphology of ZnO nanoparticles (at 30,000X and 1,00,000X) at different Sm Concentrations: (a) pristine, (b) 1 mol% (c) 3 mol% and (d) 5 mol%



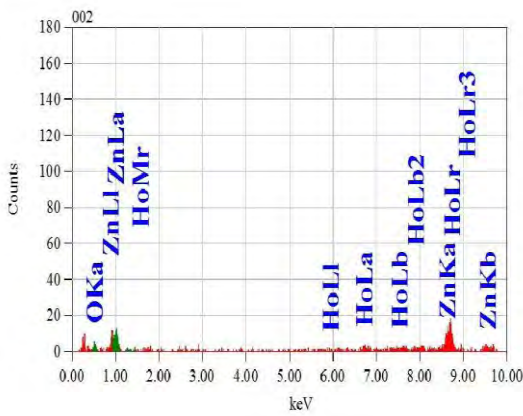
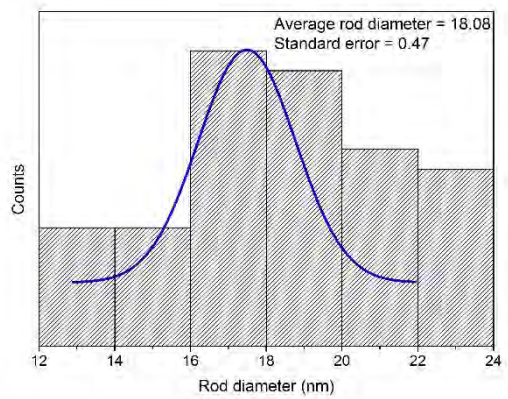
(a)



(b)



(c)



(d)

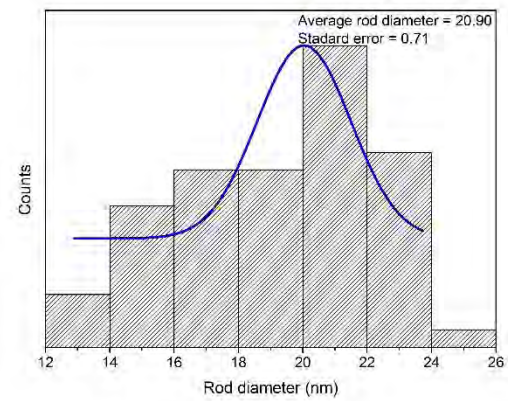
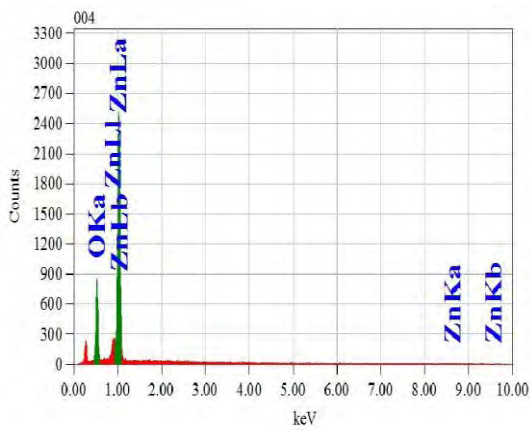
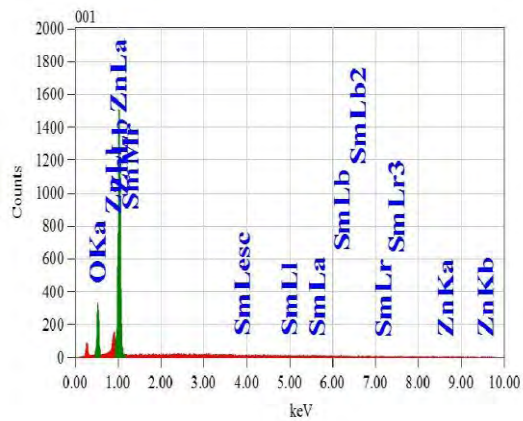
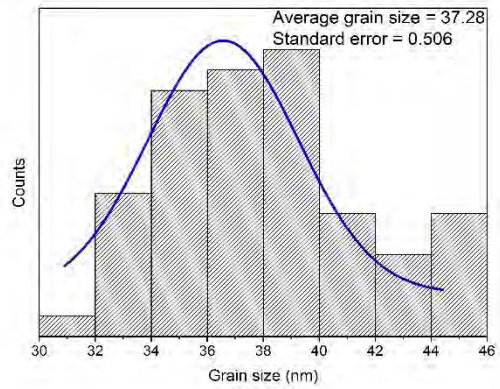


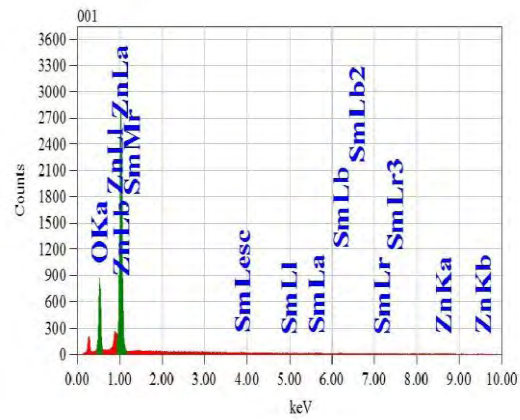
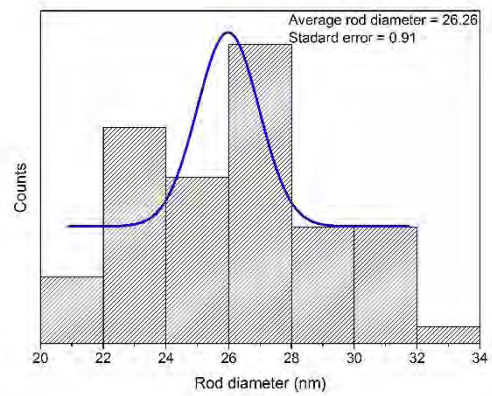
Figure 4.23 Elemental analysis and particle size distribution of ZnO nanoparticles at different Ho concentrations: (a) pristine, (b) 1 mol%, (c) 3 mol% and (d) 5 mol%



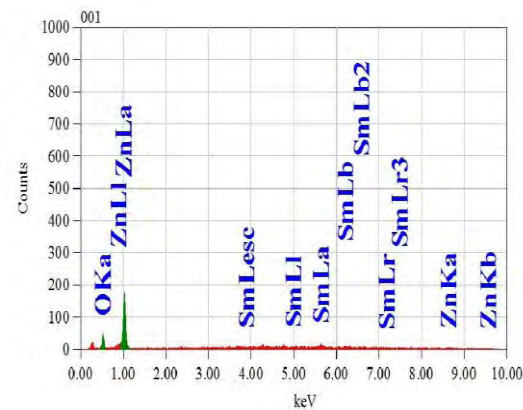
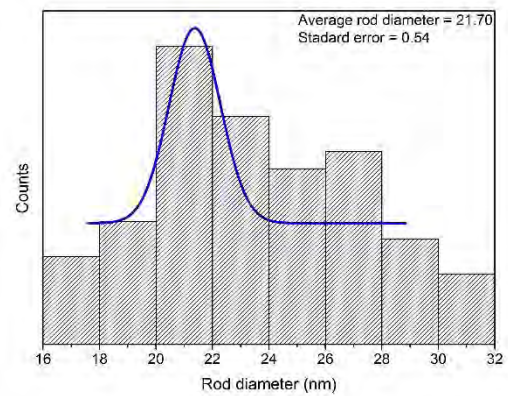
(a)



(b)



(c)



(d)

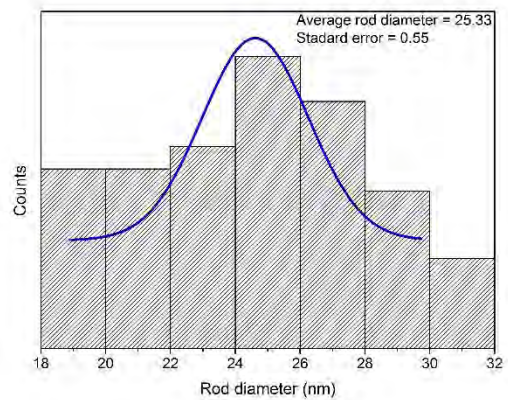


Figure 4.24 Elemental analysis and particle size distribution of ZnO nanoparticles at different Sm concentrations: (a) pristine, (b) 1 mol%, (c) 3 mol% and (d) 5 mol%

4.3.3 UV-vis DRS spectra for Doped ZnO Nanoparticles

Band gap for doped ZnO nanoparticles was calculated from diffuse reflectance spectra using Kubelka-Munc formula and shown in Figure 4.25 and 4.26. The value of direct band-gap, E_g for Ho- and Sm-doped ZnO was obtained by extrapolating the linear portion of the plot $\{F(R_\infty) \cdot hv\}^2$ vs. (hv) to intersect hv axis (Figure 4.25 and 4.26). Band gap for Ho-doped ZnO nanoparticles was calculated 3.13, 3.125 and 3.19 eV for 1 mol%, 3 mol% and 5 mol% doping. Whereas, for Sm-doped ZnO nanoparticles, band gap of 3.21, 3.18 and 3.22 eV were found for 1 mol%, 3 mol% and 5 mol% doping. 3 mol% Ho doping showed least band gap due to most effective sideway band which creates an excessive energy surface between conduction and valence bands of ZnO compared to other Ho-doped samples [66]. Similarly, 3 mol% Sm doping showed least band gap among all Sm-doped samples.

Figure 4.27 and 4.28 show diffuse reflectance spectra of pristine ZnO and doped ZnO nanoparticles annealed at 500°C for different Ho and Sm concentrations. All doped samples exhibited lower reflectance than pristine ZnO nanoparticles (evident for Figure 4.27 and 4.28). The absorption threshold of pure ZnO was observed around 370 nm showing a strong absorption band in UV region. Meanwhile, Ho- and Sm-doped ZnO nanoparticles exhibited extended absorption range to visible light region. Red shift of the optical absorption edge was observed for all the doped products compared to pure ZnO. The observed red shift indicated the narrower band gap originated from the charge transfer between the ZnO valence band and the Ho/Sm ion (4f level) [68]. When the doping concentration was increased from 1 to 3 mol%, the visible light absorption ability of the Ho- and Sm-doped ZnO was increased (Figure 4.29 and 4.30). Further increase in doping content (5 mol %) in both the cases resulted in a slight decrease in visible light absorption ability as excessive doping leads to some surface defects that act as the recombination centers for electron-hole and thus decreases the absorbability [68]. Furthermore, Ho-doped ZnO nanoparticles exhibited absorptions band in 448.5, 539.5 and 643 nm (Figure 4.29) which provides satisfactory agreement with the visible-light absorbability. These peaks were attributed to the Ho characteristic of 4f electron transitions. Figure 4.29 reveals that the light absorption of Ho-doped ZnO nanoparticles in the visible light range became more obvious as the Ho content increased from 1 mol% to 5mol%. No such absorption band was observed for Sm doped ZnO nanoparticles (Figure 4.30).

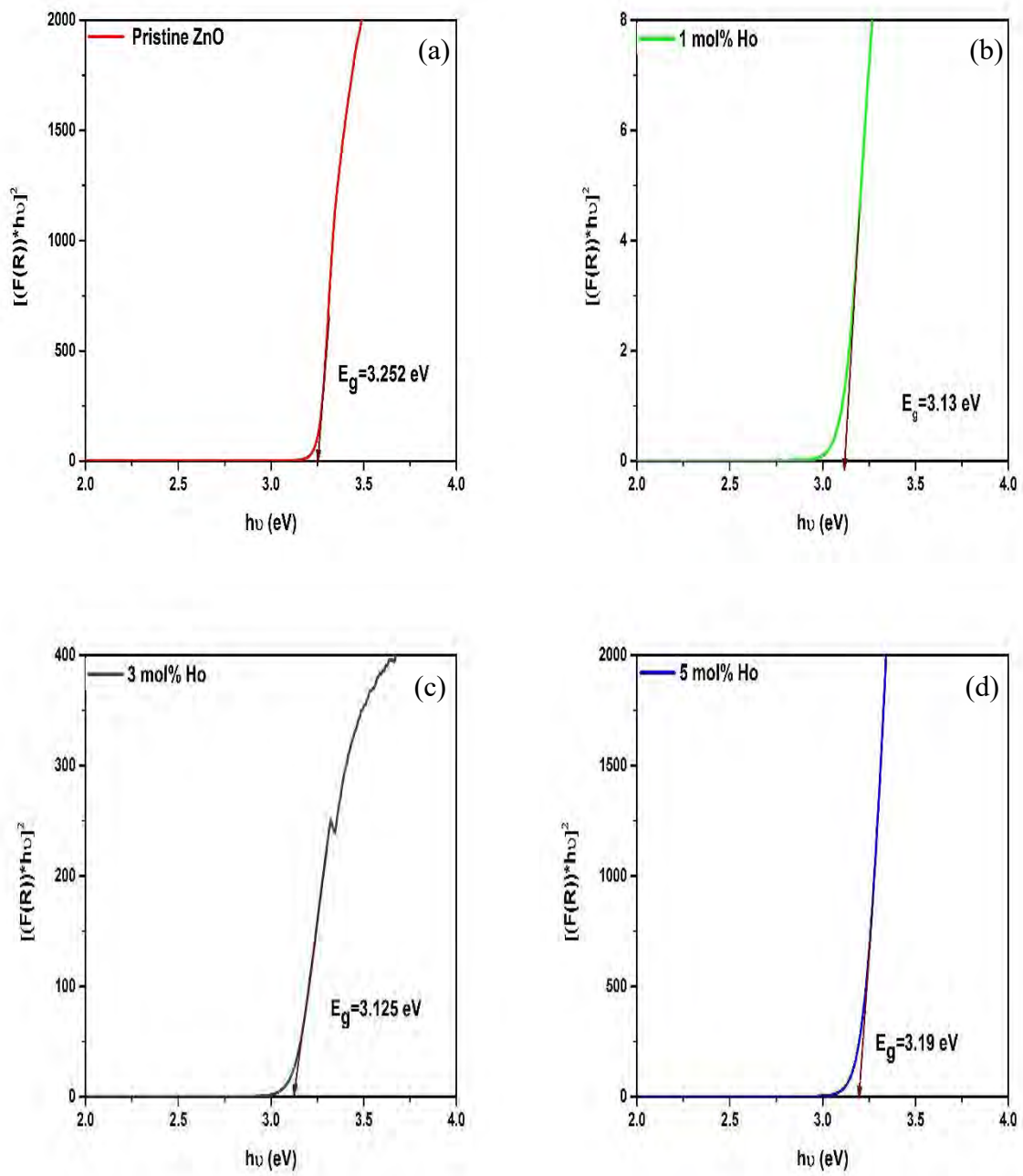


Figure 4.25 Variation in band gap with increasing Ho concentration: (a) pristine, (b) 1 mol%, (c) 3 mol% and (d) 5 mol%

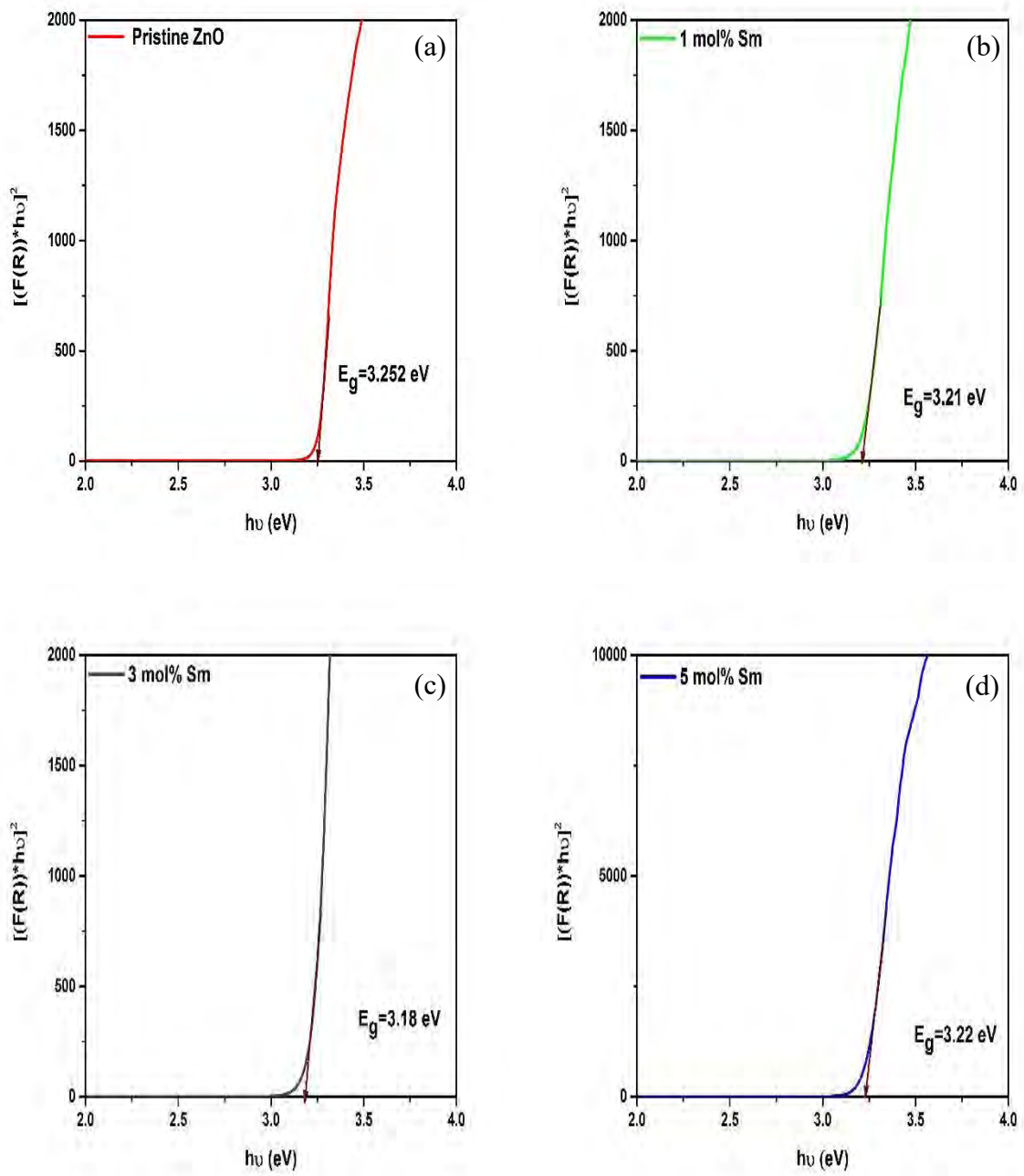


Figure 4.26 Variation in band gap with increasing Sm concentration: (a) pristine, (b) 1 mol%, (c) 3 mol% and (d) 5 mol%

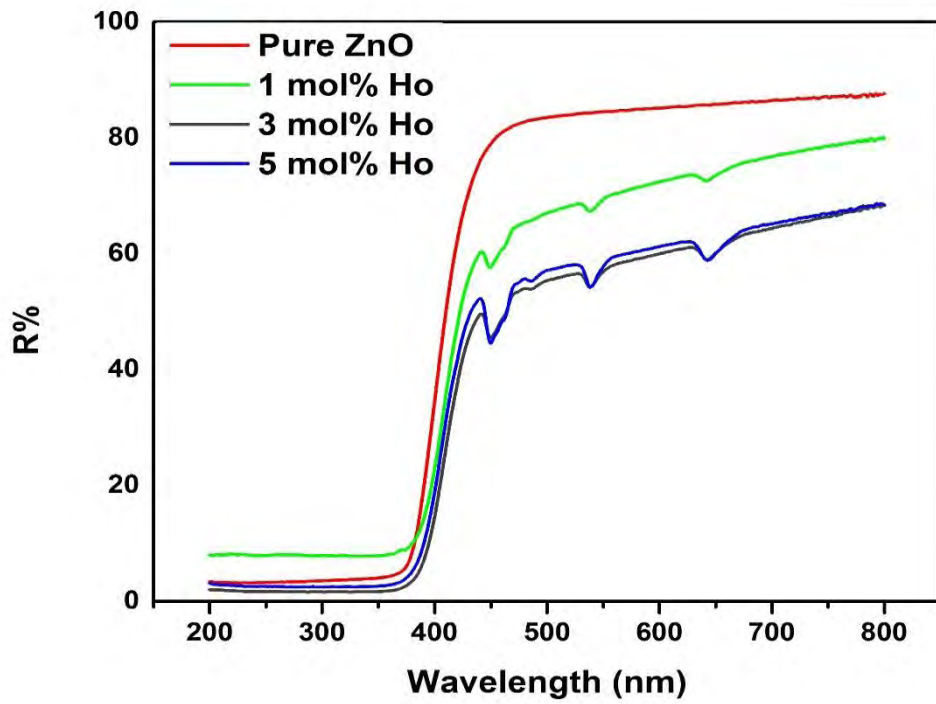


Figure 4.27 Variation in reflectance with increasing Ho concentration

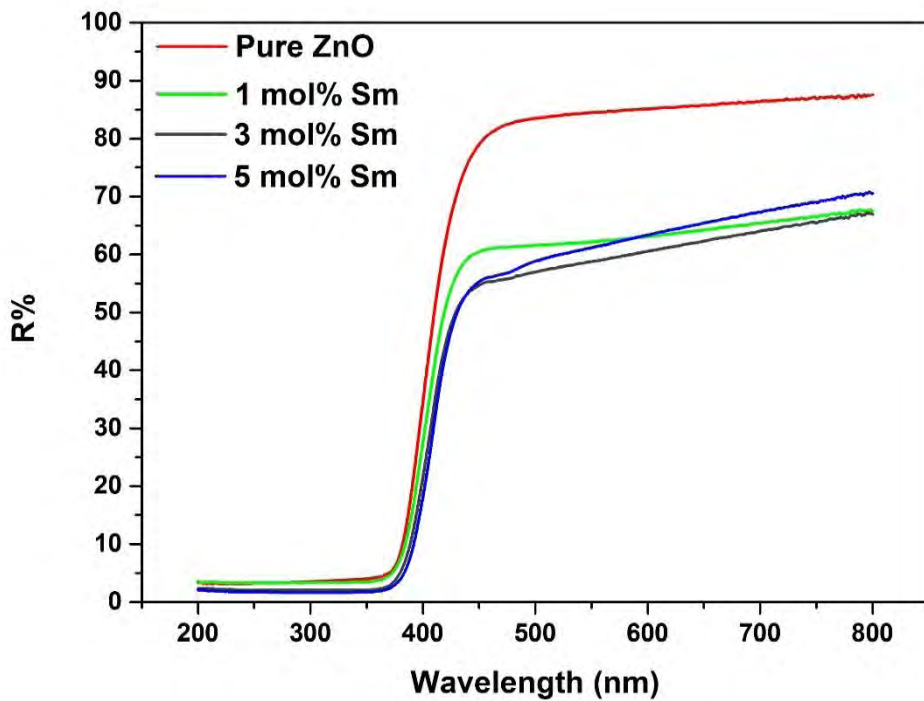


Figure 4.28 Variation in reflectance with increasing Sm concentration

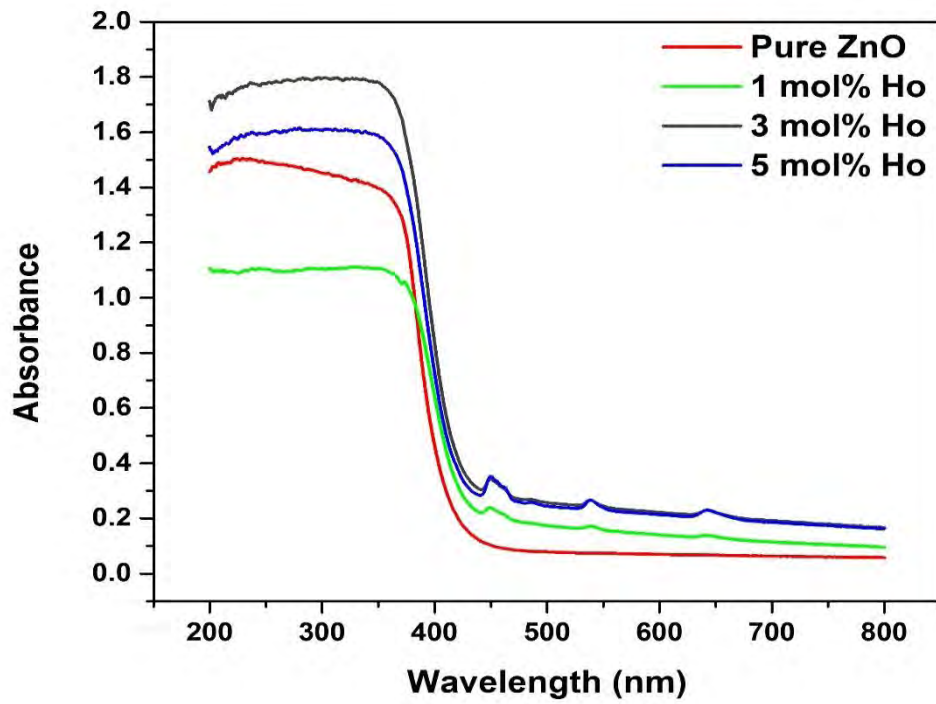


Figure 4.29 Variation in absorbance with increasing Ho concentration

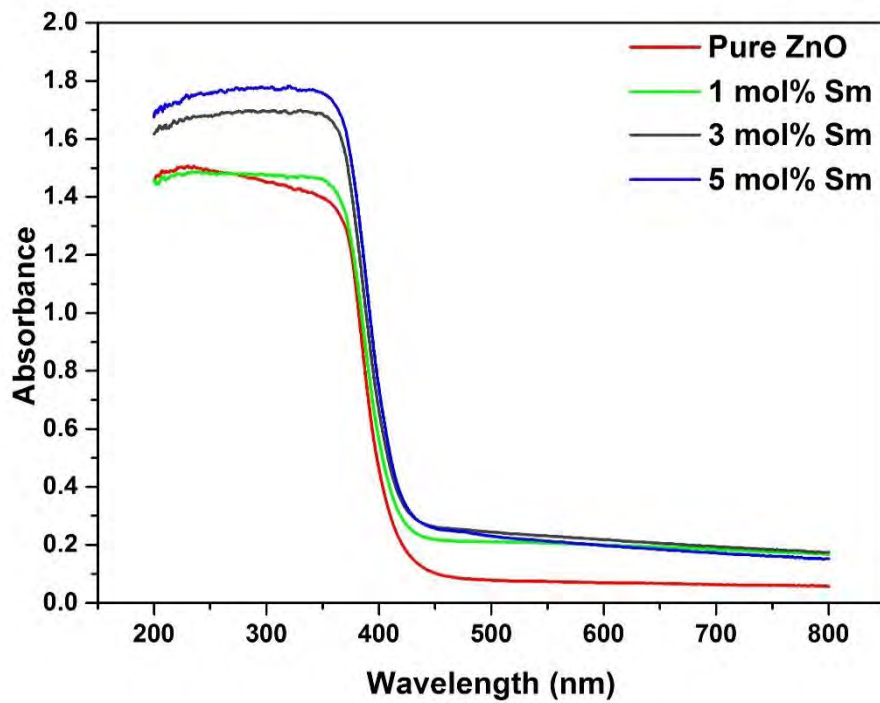


Figure 4.30 Variation in absorbance with increasing Sm concentration

4.3.4 Photoluminescence Emission Spectra for Doped ZnO Nanoparticles

Figure 4.31 and 4.32 show the PL spectra of pristine and doped ZnO nanoparticles annealed at 500°C using 200 nm UV light as excitation wavelength. Doped nanoparticles exhibit a UV emission around 397 nm and a strong orange emission around 600 nm. For both of Ho and Sm doping, the intensity of the UV emission peak of 397 nm decreased continuously upto 3 mol% as radiative recombination was lowered on rare-earth doping by trapping electrons at intermediate discrete energy states [67]. Further doping (5 mol%), in both cases, increased UV emission peak at around 397 nm as excess amount of doped particle may act as recombination center [68]. As minimum PL intensity indicates lowest recombination rate of photogenerated holes and electrons, for 3 mol% doping for both Ho- and Sm-doped ZnO, expected to show highest photocatalytic activity.

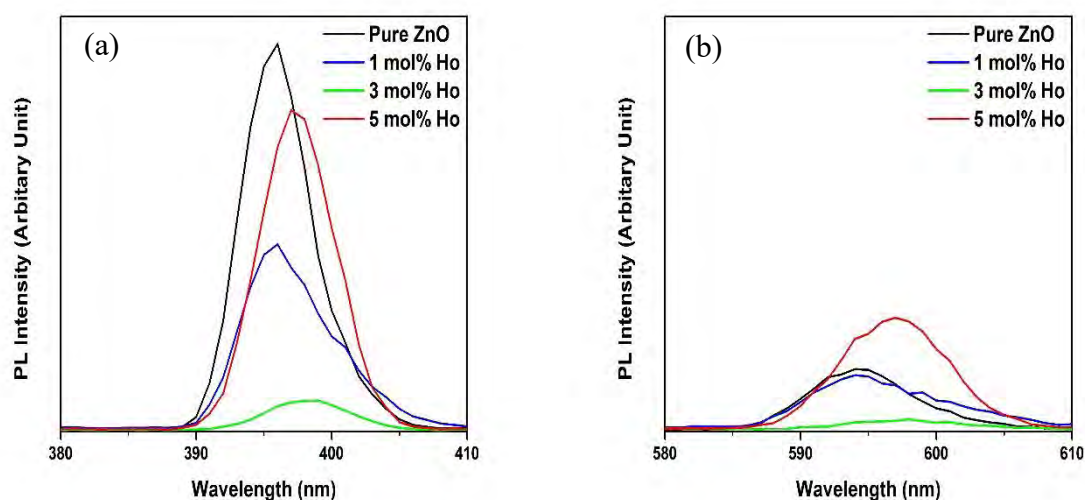


Figure 4.31 PL emission spectra showing (a) near band gap emission and (b) orange band emission at different Ho concentrations

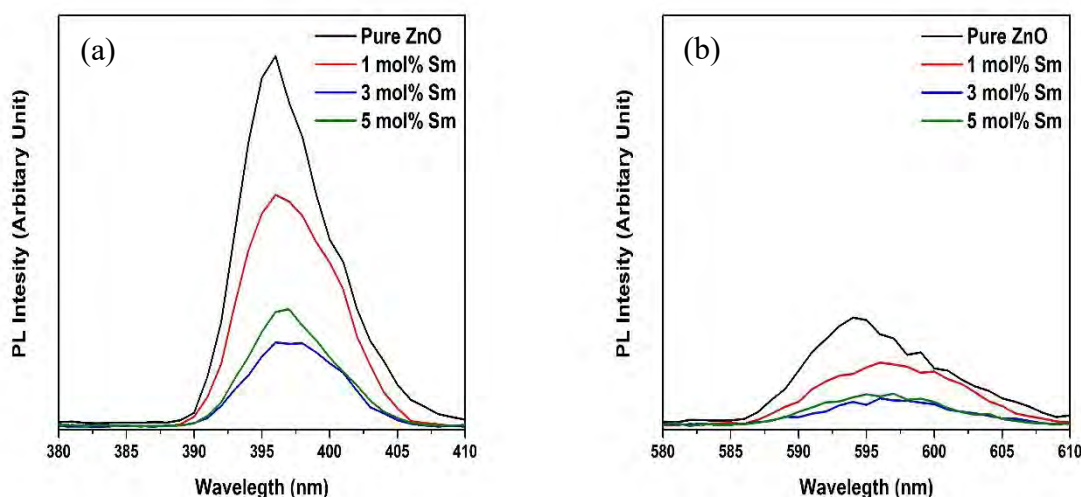


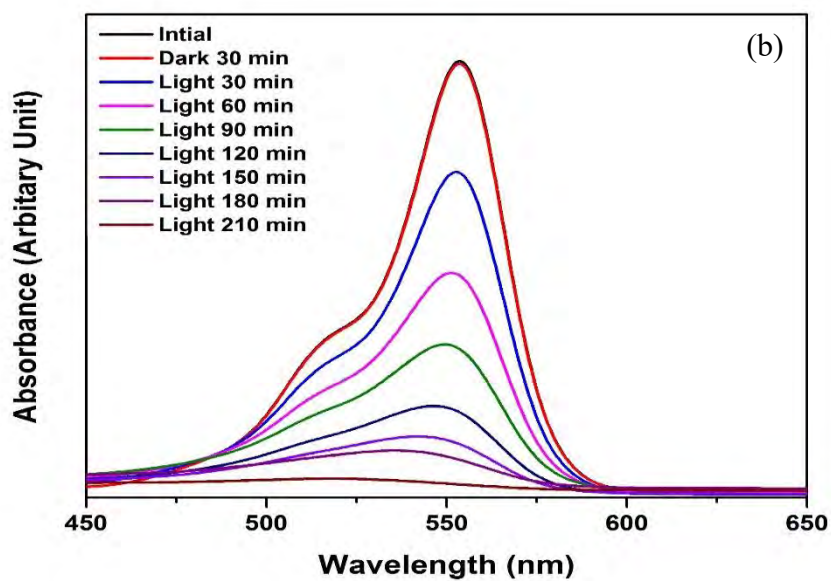
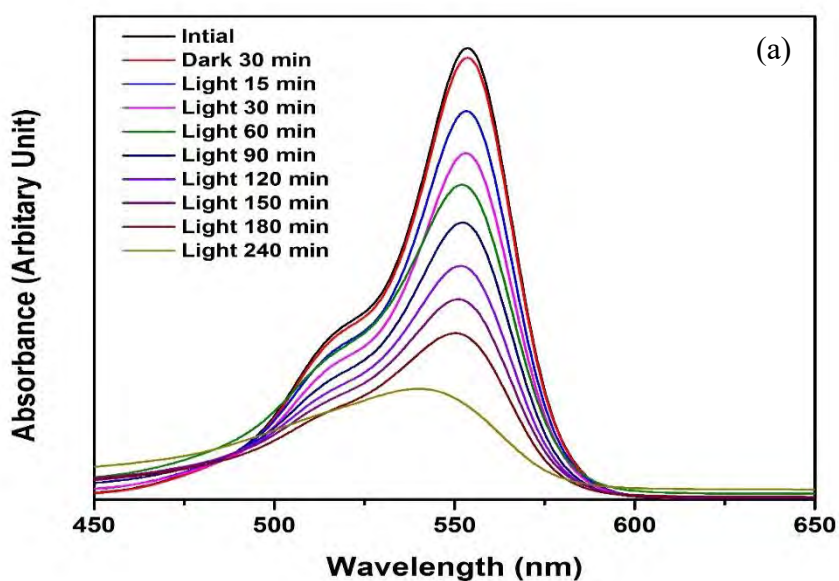
Figure 4.32 PL emission spectra showing (a) near band gap emission and (b) orange band emission at different Sm concentrations

4.3.6 Photocatalytic Activity Measurement of Doped ZnO Nanoparticles

4.3.6.1 Degradation Efficiency of Doped ZnO Nanoparticles

Figure 4.33 shows absorption spectra of Rhodamine B at different time intervals under UV irradiation for pristine and doped (3 mol% Ho and 3 mol% Sm) ZnO nanoparticles. It is evident that the strong absorption peak of Rh B solution at 555 nm steadily decreased with UV irradiation in all cases. The decrease in absorbance intensity of Rh B for doped ZnO nanoparticles was faster than that of pristine ZnO nanoparticles. Pristine ZnO showed 28.8%, 47.1%, 62.4% and 74.9% degradation after 1 hr, 2hr, 3hr and 4hr irradiation under UV-light. For 3% Ho doped ZnO degradation was 48.2%, 78.9%, 89.2% and 95.7% after 1 hr, 2hr, 3hr and 4hr irradiation. Lastly, for 3% Sm doped degradation was found 37.1%, 58.8%, 77.9% and 91.5% after 1 hr., and 2hr, 3hr and 4hr irradiation. C/C_0 was calculated and plotted against time to show the degradation of the dye (Figure 4.34). Degradation efficiency was calculated by eq. (28) and plotted against time as shown in Figure 4.35. Better degradation was observed for 3 mol% doping for both Ho and Sm compared to pristine ZnO nanoparticles. Indeed, Ho doping was found to be more effective as degradation was more for 3 mol% Ho doped ZnO nanoparticles compared to 3 mol% Sm-doped ZnO nanoparticles. This is due to the lowest

electron-hole recombination rate for 3 mol% Ho-doped ZnO nanoparticles (Figure 4.36). Moreover, effective surface area was larger of 3 mol% Ho-doped ZnO nanoparticles as it was rod shaped and had least rod diameter than 3 mol% Sm doped ZnO. Real picture of progressive degradation of Rh B solution in the presence of 3 mol% Ho doped ZnO nanoparticles under UV light at different time intervals is shown in Figure 4.37. By increasing the concentration of the photocatalysts, same degradation could be achieved at much lower time [50]. Similar phenomenon could also be observed by lowering the concentration of dyes [49].



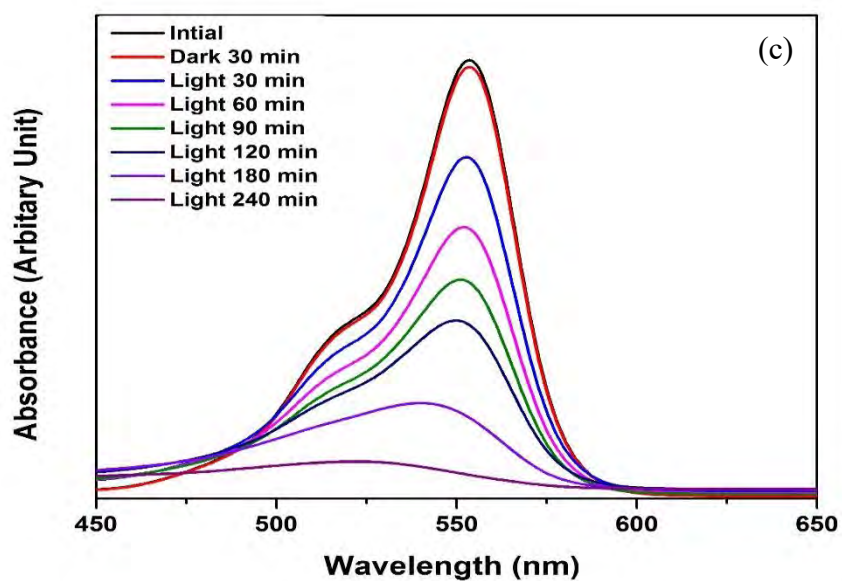


Figure 4.33 Variation of the absorption spectra for Rh B solution in the presence of (a) pristine, (b) 3 mol% Ho doped and (c) 3 mol% Sm doped ZnO nanoparticles under UV light at different time intervals

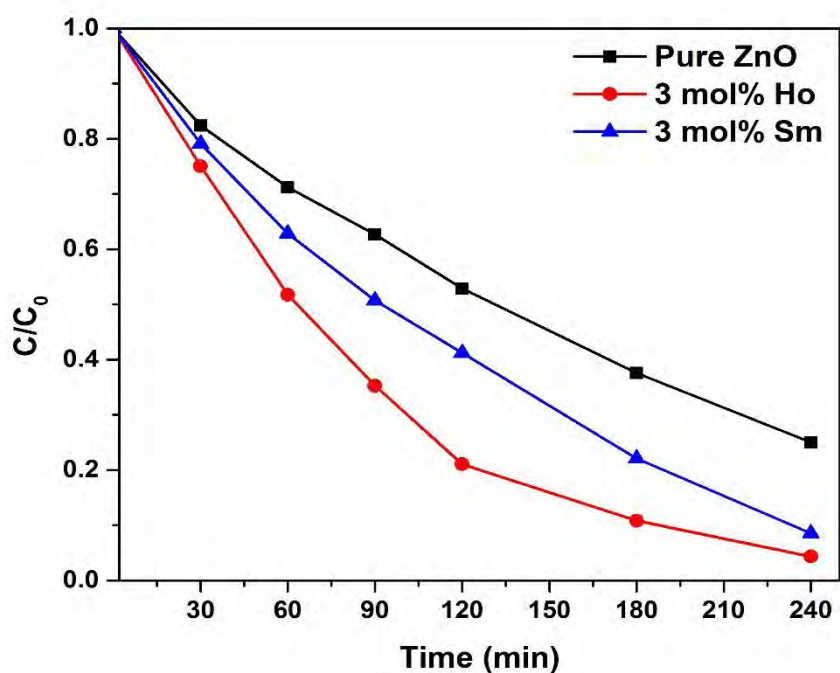


Figure 4.34 Variation in remaining concentration of dye among pristine, 3 mol% Ho and 3 mol% Sm doped ZnO nanoparticles

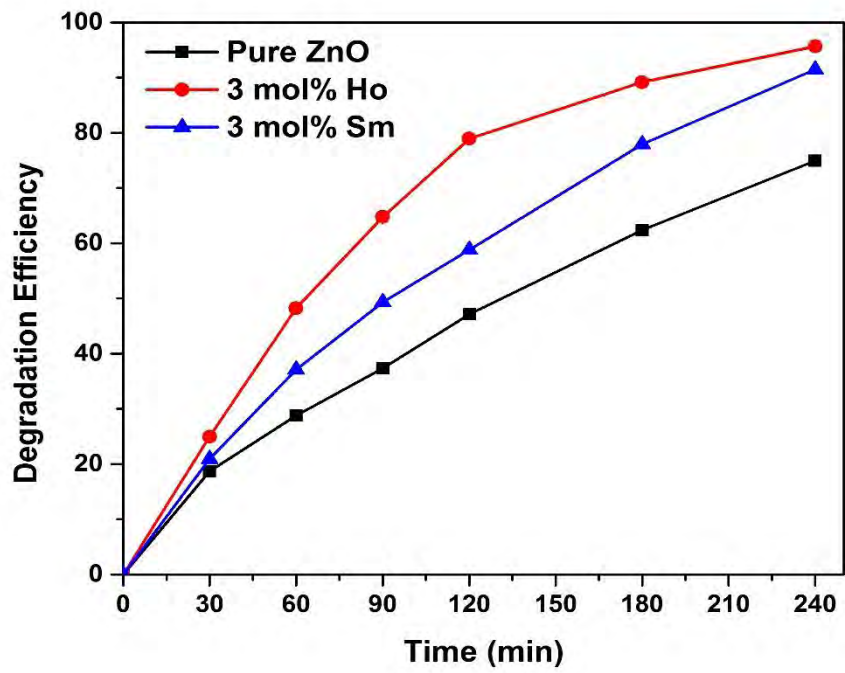


Figure 4.35 Variation in degradation efficiency among pristine, 3 mol% Ho and 3 mol% Sm doped ZnO nanoparticles

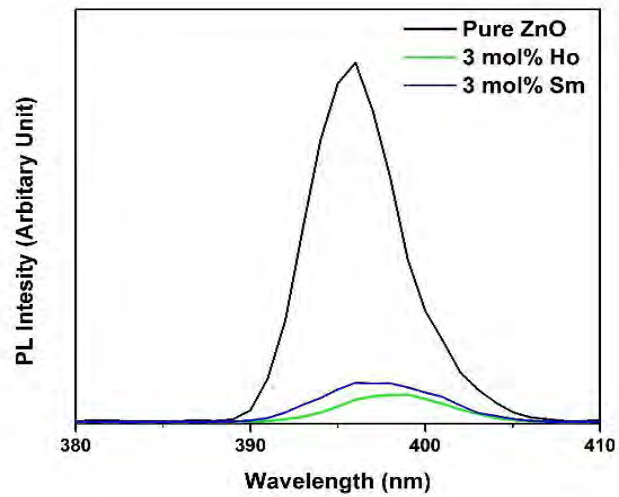


Figure 4.36 PL emission spectra comparing recombination rate among pristine, 3 mol% Ho and 3 mol% Sm doped ZnO

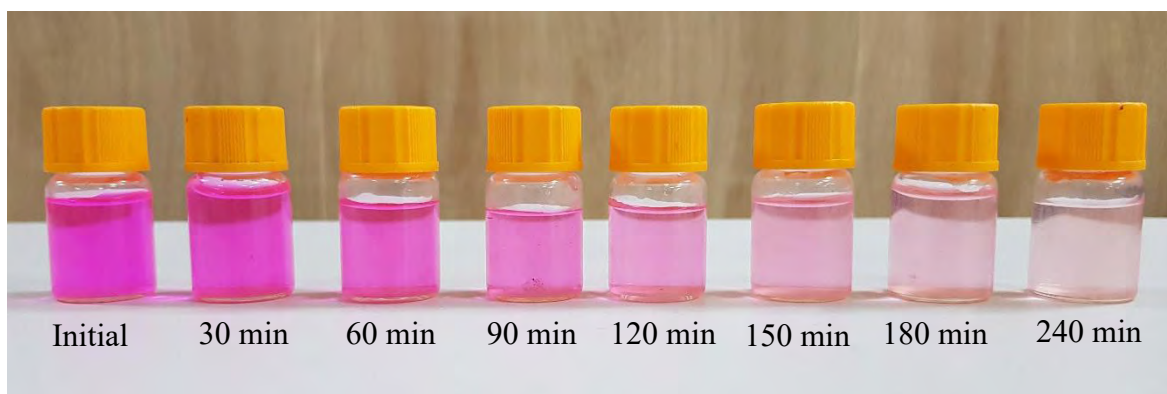


Figure 4. 37 Visual inspection of progressive degradation of Rh B solution in the presence of 3 mol% Ho doped ZnO nanoparticles under UV light at different time intervals

4.3.6.2 Degradation Kinetics of Doped ZnO Nanoparticles

The degradation of various organic dyes over illuminated semiconductor photocatalysts can be modeled by Langmuir-Hinshelwood (L–H) kinetic equation. To obtain more reliable kinetic parameters, the calculation can be done at the beginning of photocatalytic reaction since intermediates are formed during reaction and may interfere with the determination of kinetics [136]. In the case of low initial concentration, simplified apparent first-order kinetics equation (eq.29) can be used.

$$\ln \frac{c_0}{c} = Kt \quad (29)$$

Where,

C_0 = concentrations of organic compound at $t = 0$

C = concentrations of organic compound at t

K = apparent first-order rate constant

A plot of $\ln (C_0/C)$ versus time for the photocatalytic degradation of pristine and doped ZnO nanoparticles is shown in Figure 4.38 and a linear relation was observed in all photocatalysts. The apparent first-order rate constant, K was determined from the slope of the fitted line. Linear fitting was done using Originpro software. The kinetics parameters were calculated and summarized in Table 4.14. The value of rate constant, K was found 0.00555 min^{-1} for pristine ZnO nanoparticles. Value of K was increased for 3 mol% Ho-doped and 3 mol% Sm-doped ZnO nanoparticles compared to pristine ZnO nanoparticles. K was calculated 0.01267 min^{-1}

and 0.09122 min^{-1} for 3 mol% Ho-doped and 3 mol% Sm-doped ZnO nanoparticles, respectively. Degradation rate increased around 2.3 times after 3 mol% Ho doping. Similarly, after 3 mol% Sm doping degradation rate was increased around 1.7 times compared to pristine ZnO nanoparticles. 3 mol% Ho doped ZnO nanoparticles showed best degradation rate due to its higher surface area and lower electron-hole recombination rate compared to 3 mol% Sm doped ZnO nanoparticles.

Table 4.14 Kinetics parameters for pristine and doped ZnO

Photocatalyst	Fitting Equation	R ²	Pearson's r	K (min ⁻¹)
Pristine ZnO	Y= 0.00555 * X	0.99614	0.99828	0.00555
3 mol% Ho doped ZnO	Y= 0.01267 * X	0.99814	0.99917	0.01267
3 mol% Sm doped ZnO	Y= 0.09122 * X	0.98106	0.99168	0.09122

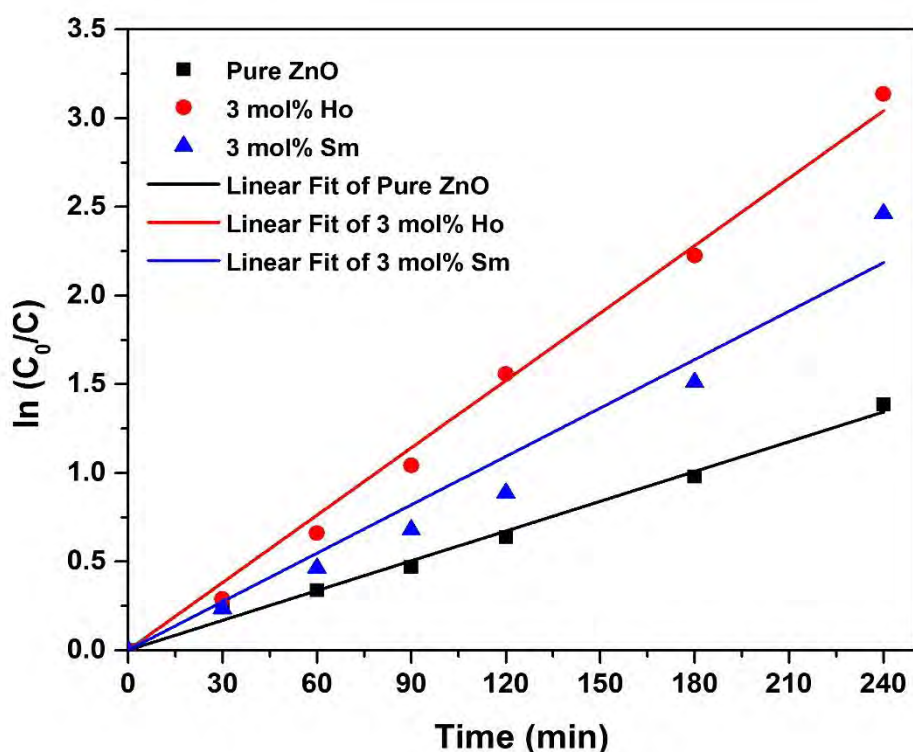
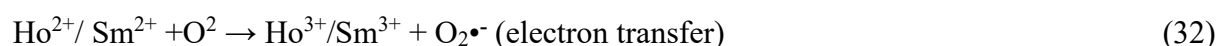


Figure 4.38 Variation in degradation kinetics among pristine, 3 mol% Ho and 3 mol% Sm doped ZnO nanoparticles

4.3.6.3 Degradation Mechanism of Doped ZnO Nanoparticles

Combining our experiment results with the related literatures, a postulated mechanism for the enhanced photocatalysis of rare earth (Ho and Sm) doped ZnO nanoparticles could be proposed in Figure 4.39. Under the irradiation, the electrons ($e_{(cb)}^-$) are excited from the valence band to the conduction band of ZnO leaving behind $h^+_{(vb)}$ (eq. 30). The presence of the rare earth (Ho^{3+} and Sm^{3+}) ions with partially filled f-orbital in ZnO being strong Lewis acid (as Ho^{3+} or Sm^{3+} receives electron) can effectively trap the $e_{(cb)}^-$ and enhance the separation of $e_{(cb)}^- - h^+_{(vb)}$ pairs (eq. 31). The reduced state of Sm^{2+} ions with 6f electrons, and Ho^{2+} ions with 11f electrons, are very instable so that the $e_{(cb)}^-$ can easily be detrapped (eq. 32) and is transferred to the O_2 molecules promoting the superoxide anion radicals ($O_2\bullet^-$) (eq. 33) formation. Then superoxide anion radicals forms hydrogen peroxide by reacting with H^+ and later hydrogen peroxide converts to active $OH\bullet$ (eqs. 34-35). It is clearly evident that Ho and Sm can serve as an effective charge carrier trap and facilitated the excited $e_{(cb)}^-$ transfer under irradiation. At the same time, the photogenerated $h^+_{(vb)}$ can be trapped on the catalyst surface undergoing charge transfer with adsorbed water molecules or with surface-bound hydroxide species to generate active $OH\bullet$ (eq. 36-37). This active $OH\bullet$ degrades the organic pollutants (eqs. 38-39) [68]. The degradation mechanism for the Ho and Sm doped ZnO nanoparticles can be given as



Thus, the separation of the charge carriers was attributed to such trapping by Sm and Ho dopant in ZnO nanoparticles. Subsequently, Sm and Ho doping enhanced the yield of $OH\bullet$ quantities, which further improved the photocatalytic activity.

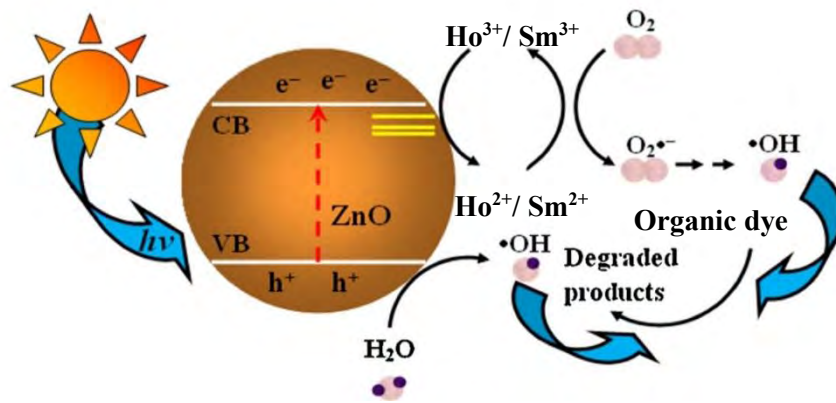


Figure 4.39 Possible photocatalytic mechanism of Ho- and Sm-doped ZnO nanoparticles

5 CONCLUSION

To the best knowledge of the authors, rare-earth elements (Ho and Sm) doped ZnO nanoparticles were successfully synthesized here as potential photocatalysts for the first time by modified sol-gel method.

ZnO nanoparticles were synthesized by modified sol-gel method with minimum complicated chemistry due to usage of water as the solvent. Nanoparticles were annealed at 400-700°C at different annealing temperatures at an interval of 100°C. Increase in annealing temperature resulted in an increase in crystallinity, particle size and recombination rate of photogenerated electron-holes pairs along with a decrease in the optical band gap. However, organics were not completely removed at 400°C and photocatalytic degradation was maximum at 500°C. Maximum photocatalytic activity at this temperature can be attributed to the lowest recombination rate of photogenerated electron-holes pairs at this temperature for the annealing temperature range 500-700°C along with the largest surface to volume ratio of the particles. Thus, 500°C was selected as the optimized annealing temperature for ZnO nanoparticles. The nanoparticles annealed at 500°C had particle size of 37.28 nm and band gap of 3.252 eV. Later, precursor to chelating agent ratio 1:2 was selected for the further experiments as particles were homogenous and densely distributed compared to the counterpart for this ratio.

XRD analysis showed that ZnO nanoparticles were crystallized and dopants were successfully incorporated into the matrix without having any other phases. Crystallinity was decreased with increasing doping concentration for both the dopants as incorporation of Ho and Sm into the ZnO matrix creates lattice disorder due to atomic radius mismatching. Crystallite size was also decreased with increasing doping content due to the formation of Ho–O–Zn and Sm–O–Zn terminating faces inhibiting any further growth of the crystal. As revealed from the SEM micrographs, morphology of the nanoparticles were changed from hexagonal for pristine ZnO nanoparticles to rod shape for doped nanoparticles due to the charge anisotropy on doping. 3 mol% Ho-doped ZnO nanoparticles showed least rod diameter of 18.08 nm among all the Ho-doped samples due to the differential anisotropic growth rate with increasing doping concentration. Similarly, 3 mol% Sm showed least rod diameter of 20.9 nm among all the Sm-doped samples.

Red shift of the optical absorption edge was observed for all the doped products compared to the pure ZnO nanoparticles. The observed red shift indicated the narrower band gap originated from the charge transfer between the ZnO valence band and the Ho/Sm ion (4f level). 3 mol% Ho doping showed least band gap of 3.125 eV due to the most effective sideway band which creates an excessive energy surface between conduction and valence bands of ZnO compared to other Ho-doped samples. Similarly, 3 mol% Sm doping showed least band gap of 3.18 eV among all the Sm-doped samples. Electron-hole recombination rate was decreased in all the doped samples as discrete energy states of Ho and Sm ions were used to trap the electrons. 3 mol% Ho- and 3 mol% Sm-doped nanoparticles exhibited least electron-hole recombination rate compared to the other respective counterparts due to the most effective electron scavenging capacity for this concentration.

Finally, the photocatalytic studies revealed that 3 mol% Ho- and 3 mol% Sm-doped ZnO nanoparticles exhibited the best photocatalytic degradation of Rhodamine B compared to the pristine and other doped ZnO nanoparticles under UV irradiation. The results followed the pseudo-first order rate kinetics. Rate constant K was 2.3 times and 1.7 times larger for 3% Ho-doped and 3% Sm doped, respectively, than that of the pristine ZnO nanoparticles. The enhanced photocatalytic performance of rare earth-doped ZnO nanoparticles can be attributed to the decrease in the recombination rate of photogenerated electron-hole pairs. 3 mol% Ho-doped ZnO nanoparticles showed best degradation rate due to its higher surface area and lower photogenerated electron-hole recombination rate compared to 3 mol% Sm doped ZnO nanoparticles.

6 SCOPE FOR FUTURE INVESTIGATIONS

The following recommendations for future research work may be suggested:

- Co-doping of ZnO with two rare-earth elements can be tried to observe its photocatalytic behavior.
- As both Ho and Sm have high magnetic moments, so magnetic behavior of Ho- and Sm-doped ZnO nanoparticles can be studied.
- In this thesis, modified sol-gel technique was used. Other non-aqueous solvents can be tried to make comparative study among different solvent based processes.
- Antibacterial effect of Ho- and Sm-doped ZnO nanoparticles can be studied.
- Different chelating agent can be used to observe the change in photocatalytic activity of synthesized doped ZnO nanoparticles.
- Coupling doped ZnO nanoparticles with other heterogeneous photocatalyst can be studied to observe the photocatalytic effect of the composite.

REFERENCES

- [1] Hartley, T.W. (2006). Public perception and participation in water reuse. *Desalination*, 187(1–3), pp.115–126.
- [2] Liu L, Johnson HL, Cousens S, Perin J, Scott S, Lawn JE, Rudan I, Campbell H, Cibulskis R, Li M, Mathers C, Black RE (2012) Global, regional, and national causes of child mortality: an updated systematic analysis for 2010 with time trends since 2000. *The Lancet* 379 (9832), pp.2151–2161.
- [3] Capelo-Martínez, J.L., Ximénez-Embún, P., Madrid, Y. and Cámara, C. (2004). Advanced oxidation processes for sample treatment in atomic spectrometry. *TrAC Trends in Analytical Chemistry*, 23(4), pp.331–340.
- [4] Rajeshwar K, Osugi ME, Chanmanee W, Chenthamarakshan CR, Zanoni M, Kajitvichyanukul P, Krishnan-Ayer R (2008) Heterogeneous photocatalytic treatment of organic dyes in air and aqueous media. *J Photochem Photobiol C* 9(4), pp.171–192.
- [5] Rehman S, Ullah R, Butt AM, Gohar ND (2009) Strategies of making TiO₂ and ZnO visible light active. *J Hazard Mater* 170(2–3):560–569.
- [6] Fujishima A, Honda K (1972) Electrochemical photolysis of water at a semiconductor electrode. *Nature* 238(5358), pp.37–38.
- [7] Choi, K., Kang, T. and Oh, S.-G. (2012). Preparation of disk shaped ZnO particles using surfactant and their PL properties. *Materials Letters*, 75, pp.240–243.
- [8] Liang, S., Xiao, K., Mo, Y. and Huang, X. (2012). A novel ZnO nanoparticle blended polyvinylidene fluoride membrane for anti-irreversible fouling. *Journal of Membrane Science*, 394–395, pp.184–192.
- [9] Alfano, O., Bahnemann, D., Cassano, A., Dillert, R. and Goslich, R. (2000). Photocatalysis in water environments using artificial and solar light. *Catalysis Today*, 58(2–3), pp.199–230.
- [10] Herrmann, J.-M. (1999). Heterogeneous photocatalysis: fundamentals and applications to the removal of various types of aqueous pollutants. *Catalysis Today*, 53(1), pp.115–129.
- [11] Rajamanickam, D. and Shanthi, M. (2016). Photocatalytic degradation of an organic pollutant by zinc oxide – solar process. *Arabian Journal of Chemistry*, 9, pp.S1858–S1868.
- [12] Qiu, R., Zhang, D., Mo, Y., Song, L., Brewer, E., Huang, X. and Xiong, Y. (2008). Photocatalytic activity of polymer-modified ZnO under visible light irradiation. *Journal of Hazardous Materials*, 156(1–3), pp.80–85.
- [13] Sirelkhatim, A., Mahmud, S., Seeni, A., Kaus, N.H.M., Ann, L.C., Bakhori, S.K.M., Hasan, H. and Mohamad, D. (2015). Review on Zinc Oxide Nanoparticles: Antibacterial Activity and Toxicity Mechanism. *Nano-Micro Letters*, 7(3), pp.219–242.

- [14] Han G, Wang L, Pei C, Shi R, Liu B, Zhao H, Yang H, Liu S (2014) Size-dependent optical properties and enhanced visible light photocatalytic activity of wurtzite CdSe hexagonal nanoflakes with dominant 001 facets. *J Alloy Compd* 610, pp.62–68.
- [15] Malato S, Fernández-Ibáñez P, Maldonado MI, Blanco J, Gernjak W (2009) Decontamination and disinfection of water by solar photocatalysis: recent overview and trends. *Catal Today* 147(1), pp.1–59.
- [16] Rezaei, M. and Habibi-Yangjeh, A. (2013). Simple and large scale refluxing method for preparation of Ce-doped ZnO nanostructures as highly efficient photocatalyst. *Applied Surface Science*, 265, pp.591–596
- [17] Konstantinou IK, Albanis TA (2004) TiO₂-assisted photocatalytic degradation of azo dyes in aqueous solution: kinetic and mechanistic investigations. *Appl Catal B* 49(1), pp.1–5.
- [18] Nakata K, Fujishima A (2012) TiO₂ photocatalysis: design and applications. *J Photochem Photobiol C* 13(3), pp.169–189.
- [19] Khan MM, Adil SF, Al-Mayouf A (2015b) Metal oxides as photocatalysts. *J Saudi Chem Soc* 19 (5), pp.462–464.
- [20] Hagen J (2006) *Industrial catalysis: a practical approach*/Jens Hagen, 2nd edn. Wiley, Weinheim.
- [21] Gharoy Ahangar, E., Abbaspour-Fard, M.H., Shahtahmassebi, N., Khojastehpour, M. and Maddahi, P. (2014). Preparation and Characterization of PVA/ZnO Nanocomposite. *Journal of Food Processing and Preservation*, 39(6), pp.1442–1451.
- [22] Rauf, M.A. and Ashraf, S.S. (2009). Fundamental principles and application of heterogeneous photocatalytic degradation of dyes in solution. *Chemical Engineering Journal*, 151(1–3), pp.10–18.
- [23] Meng, Y., Lin, Y. and Yang, J. (2013). Synthesis of rod-cluster ZnO nanostructures and their application to dye-sensitized solar cells. *Applied Surface Science*, 268, pp.561–565.
- [24] Ohtomo, A., Kawasaki, M., Ohkubo, I., Koinuma, H., Yasuda, T. and Segawa, Y. (1999). Structure and optical properties of ZnO/Mg_{0.2}Zn_{0.8}O superlattices. *Applied Physics Letters*, 75(7), pp.980–982.
- [25] Antony, J., Chen, X.B., Morrison, J., Bergman, L., Qiang, Y., McCready, D.E. and Engelhard, M.H. (2005). ZnO nanoclusters: Synthesis and photoluminescence. *Applied Physics Letters*, 87(24), pp.241917-241920.
- [26] Huang, M.H. (2001). Room-Temperature Ultraviolet Nanowire Nanolasers. *Science*, 292(5523), pp.1897–1899.
- [27] R.D., D.M., E.K. and V.V. (2019). Microwave Assisted Synthesis of Zinc Oxide Nanoparticles and Its Antimicrobial Efficiency. Volume 5, Issue 1, 2019, 5(1), pp.640–641.

- [28] Kumar, R., Kumar, G. and Umar, A. (2014). Zinc Oxide Nanomaterials for Photocatalytic Degradation of Methyl Orange: A Review. *Nanoscience and Nanotechnology Letters*, 6(8), pp.631–650.
- [29] Morkoç H, Özgür Ü General properties of ZnO. *Zinc oxide*. Weinheim, Germany: Wiley-VCH Verlag GmbH & Co. KGaA; n.d., pp. 1–76.
- [30] Özgür Ü, Avrutin V, Morkoç H. Chapter 16 – zinc oxide materials and devices grown by MBE. *Mol Beam Epitaxy* 2013;pp.369–416.
- [31] Kucheyev, S.O., Bradby, J.E., Williams, J.S., Jagadish, C. and Swain, M.V. (2002). Mechanical deformation of single-crystal ZnO. *Applied Physics Letters*, 80(6), pp.956–958.
- [32] Zhang, Q., Dandeneau, C.S., Zhou, X. and Cao, G. (2009). ZnO Nanostructures for Dye-Sensitized Solar Cells. *Advanced Materials*, 21(41), pp.4087–4108.
- [33] Dal Corso, A., Posternak, M., Resta, R. and Baldereschi, A. (1994). Ab initio study of piezoelectricity and spontaneous polarization in ZnO. *Physical Review B*, 50(15), pp.10715–10721.
- [34] Catti, M., Noel, Y. and Dovesi, R. (2003). Full piezoelectric tensors of wurtzite and zinc blende ZnO and ZnS by first-principles calculations. *Journal of Physics and Chemistry of Solids*, 64(11), pp.2183–2190.
- [35] Özgür, Ü., Alivov, Y.I., Liu, C., Teke, A., Reshchikov, M.A., Doğan, S., Avrutin, V., Cho, S.-J. and Morkoç, H. (2005). A comprehensive review of ZnO materials and devices. *Journal of Applied Physics*, 98(4), pp.041301-041328.
- [36] Castillo-Ledezma JH, Sánchez Salas JL, López-Malo A, Bandala ER (2011) Effect of pH, solar irradiation, and semiconductor concentration on the photocatalytic disinfection of *Escherichia coli* in water using nitrogen-doped TiO₂. *Eur Food Res Technol* 233(5), pp.825–834.
- [37] Zhu, Y. and Zhou, Y. (2008). Preparation of pure ZnO nanoparticles by a simple solid-state reaction method. *Applied Physics A*, 92(2), pp.275–278.
- [38] Kumar, V., Singh, R.G., Purohit, L.P. and Mehra, R.M. (2011). Structural, Transport and Optical Properties of Boron-doped Zinc Oxide Nanocrystalline. *Journal of Materials Science & Technology*, 27(6), pp.481–488.
- [39] Li, M. and Li, J.C. (2006). Size effects on the band-gap of semiconductor compounds. *Materials Letters*, 60(20), pp.2526–2529.
- [40] Kaur, J. and Singhal, S. (2014). Facile synthesis of ZnO and transition metal doped ZnO nanoparticles for the photocatalytic degradation of Methyl Orange. *Ceramics International*, 40(5), pp.7417–7424.
- [41] CHEN, T., ZHENG, Y., LIN, J. and CHEN, G. (2008). Study on the Photocatalytic Degradation of Methyl Orange in Water Using Ag/ZnO as Catalyst by Liquid Chromatography Electrospray Ionization Ion-Trap Mass Spectrometry. *Journal of the American Society for Mass Spectrometry*, 19(7), pp.997–1003.

- [42] Kumar, S.S., Venkateswarlu, P., Rao, V.R. and Rao, G.N. (2013). Synthesis, characterization and optical properties of zinc oxide nanoparticles. *International Nano Letters*, 3(1).
- [43] Štengl, V., Henych, J. and Slušná, M. (2016). h-BN-TiO₂ Nanocomposite for Photocatalytic Applications. *Journal of Nanomaterials*, 2016, pp.1–12.
- [44] Saravanan, R., Thirumal, E., Gupta, V.K., Narayanan, V. and Stephen, A. (2013). The photocatalytic activity of ZnO prepared by simple thermal decomposition method at various temperatures. *Journal of Molecular Liquids*, 177, pp.394–401.
- [45] Ma, H., Yue, L., Yu, C., Dong, X., Zhang, X., Xue, M., Zhang, X. and Fu, Y. (2012). Synthesis, characterization and photocatalytic activity of Cu-doped Zn/ZnO photocatalyst with carbon modification. *Journal of Materials Chemistry*, 22(45), pp.23780-23785.
- [46] Jia, Z., Ren, D., Xu, L. and Zhu, R. (2012). Preparation, characterization and photocatalytic activity of porous zinc oxide superstructure. *Materials Science in Semiconductor Processing*, 15(3), pp.270–276.
- [47] Anjaneyulu, Y., Sreedhara Chary, N. and Samuel Suman Raj, D. (2005). Decolourization of Industrial Effluents – Available Methods and Emerging Technologies – A Review. *Reviews in Environmental Science and Bio/Technology*, 4(4), pp.245–273.
- [48] Neppolian, B. (2002). Solar/UV-induced photocatalytic degradation of three commercial textile dyes. *Journal of Hazardous Materials*, 89(2–3), pp.303–317.
- [49] KANSAL, S., SINGH, M. and SUD, D. (2007). Studies on photodegradation of two commercial dyes in aqueous phase using different photocatalysts. *Journal of Hazardous Materials*, 141(3), pp.581–590.
- [50] Daneshvar, N., Salari, D. and Khataee, A.. (2004). Photocatalytic degradation of azo dye acid red 14 in water on ZnO as an alternative catalyst to TiO₂. *Journal of Photochemistry and Photobiology A: Chemistry*, 162(2–3), pp.317–322.
- [51] Gonçalves, M.S.T., Oliveira-Campos, A.M.F., Pinto, E.M.M.S., Plasência, P.M.S. and Queiroz, M.J.R.P. (1999). Photochemical treatment of solutions of azo dyes containing TiO₂. *Chemosphere*, 39(5), pp.781–786.
- [52] Chen, C., Liu, J., Liu, P. and Yu, B. (2011). Investigation of Photocatalytic Degradation of Methyl Orange by Using Nano-Sized ZnO Catalysts. *Advances in Chemical Engineering and Science*, 01(01), pp.9–14.
- [53] Sahoo, C., Gupta, A.K. and Pal, A. (2005). Photocatalytic degradation of Methyl Red dye in aqueous solutions under UV irradiation using Ag⁺ doped TiO₂. *Desalination*, 181(1–3), pp.91–100.
- [54] Mehrotra, K., Yablonsky, G.S. and Ray, A.K. (2003). Kinetic Studies of Photocatalytic Degradation in a TiO₂ Slurry System: Distinguishing Working Regimes and Determining Rate Dependences. *Industrial & Engineering Chemistry Research*, 42(11), pp.2273–2281.

- [55] Abdollahi, Y., Abdullah, A.H., Zainal, Z. and Yusof, N.A. (2011). Photocatalytic Degradation of p-Cresol by Zinc Oxide under UV Irradiation. *International Journal of Molecular Sciences*, 13(1), pp.302–315.
- [56] Wang, R., Xin, J.H., Yang, Y., Liu, H., Xu, L. and Hu, J. (2004). The characteristics and photocatalytic activities of silver doped ZnO nanocrystallites. *Applied Surface Science*, 227(1–4), pp.312–317.
- [57] Yun, S., Lee, J., Chung, J. and Lim, S. (2010). Improvement of ZnO nanorod-based dye-sensitized solar cell efficiency by Al-doping. *Journal of Physics and Chemistry of Solids*, 71(12), pp.1724–1731.
- [58] Etacheri, V., Roshan, R. and Kumar, V. (2012). Mg-Doped ZnO Nanoparticles for Efficient Sunlight-Driven Photocatalysis. *ACS Applied Materials & Interfaces*, 4(5), pp.2717–2725.
- [59] Phuruangrat, A., Kongnuanyai, S., Thongtem, T. and Thongtem, S. (2013). Ultrasound-assisted synthesis, characterization and optical property of 0–3wt% Sn-doped ZnO. *Materials Letters*, 91, pp.179–182.
- [60] Di Valentin, C. and Pacchioni, G. (2013). Trends in non-metal doping of anatase TiO₂: B, C, N and F. *Catalysis Today*, 206, pp.12–18.
- [61] Duan, L., Zhang, W., Yu, X., Jiang, Z., Luan, L., Chen, Y. and Li, D. (2012). Annealing effects on properties of Ag–N dual-doped ZnO films. *Applied Surface Science*, 258(24), pp.10064–10067.
- [62] Nenavathu, B.P., Krishna Rao, A.V.R., Goyal, A., Kapoor, A. and Dutta, R.K. (2013). Synthesis, characterization and enhanced photocatalytic degradation efficiency of Se doped ZnO nanoparticles using trypan blue as a model dye. *Applied Catalysis A: General*, 459, pp.106–113.
- [63] Sharma, A., Dhar, S., Singh, B.P., Kundu, T., Spasova, M. and Farle, M. (2012). Influence of Tb doping on the luminescence characteristics of ZnO nanoparticles. *Journal of Nanoparticle Research*, 14(2).
- [64] Aneesh, P.M. and Jayaraj, M.K. (2010). Red luminescence from hydrothermally synthesized Eu-doped ZnO nanoparticles under visible excitation. *Bulletin of Materials Science*, 33(3), pp.227–231.
- [65] Goel, S., Sinha, N., Yadav, H., Godara, S., Joseph, A.J. and Kumar, B. (2017). Ferroelectric Gd-doped ZnO nanostructures: Enhanced dielectric, ferroelectric and piezoelectric properties. *Materials Chemistry and Physics*, 202, pp.56–64.
- [66] Phuruangrat, A., Yayapao, O., Thongtem, T. and Thongtem, S. (2014). Preparation, characterization and photocatalytic properties of Ho doped ZnO nanostructures synthesized by sonochemical method. *Superlattices and Microstructures*, 67, pp.118–126.
- [67] Sin, J.-C., Lam, S.-M., Lee, K.-T., Mohamed, A.R. (2013). Preparation and photocatalytic properties of visible light-driven samarium-doped ZnO nanorods. *Ceramics International*, 39(5), pp.5833–5843.

- [68] Sin, J.-C., Lam, S.-M., Lee, K.-T., Mohamed, A.R. (2014). Preparation of rare earth-doped ZnO hierarchical micro/nanospheres and their enhanced photocatalytic activity under visible light irradiation. *Ceramics International*, 40(4), pp.5431–5440.
- [69] Chiang, Y.-J. and Lin, C.-C. (2013). Photocatalytic decolorization of methylene blue in aqueous solutions using coupled ZnO/SnO₂ photocatalysts. *Powder Technology*, 246, pp.137–143.
- [70] Yang, G., Yan, Z. and Xiao, T. (2012). Preparation and characterization of SnO₂/ZnO/TiO₂ composite semiconductor with enhanced photocatalytic activity. *Applied Surface Science*, 258(22), pp.8704–8712.
- [71] Wang, H., Baek, S., Lee, J. and Lim, S. (2009). High photocatalytic activity of silver-loaded ZnO-SnO₂ coupled catalysts. *Chemical Engineering Journal*, 146(3), pp.355–361.
- [72] Zhang, M., An, T., Hu, X., Wang, C., Sheng, G. and Fu, J. (2004). Preparation and photocatalytic properties of a nanometer ZnO–SnO₂ coupled oxide. *Applied Catalysis A: General*, 260(2), pp.215–222.
- [73] Zhang, Y. and Mu, J. (2007). Controllable synthesis of flower- and rod-like ZnO nanostructures by simply tuning the ratio of sodium hydroxide to zinc acetate. *Nanotechnology*, 18(7), p.075606.
- [74] Gupta, J., Barick, K.C. and Bahadur, D. (2011). Defect mediated photocatalytic activity in shape-controlled ZnO nanostructures. *Journal of Alloys and Compounds*, 509(23), pp.6725–6730.
- [75] Ong, C.B., Mohammad, A.W., Rohani, R., Ba-Abbad, M.M. and Hairom, N.H.H. (2016). Solar photocatalytic degradation of hazardous Congo red using low-temperature synthesis of zinc oxide nanoparticles. *Process Safety and Environmental Protection*, 104, pp.549–557.
- [76] Kuriakose, S., Bhardwaj, N., Singh, J., Satpati, B. and Mohapatra, S. (2013). Structural, optical and photocatalytic properties of flower-like ZnO nanostructures prepared by a facile wet chemical method. *Beilstein Journal of Nanotechnology*, 4, pp.763–770.
- [77] Tang, H., Zhu, L., Ye, Z., He, H., Zhang, Y., Zhi, M., Yang, F., Yang, Z. and Zhao, B. (2007). Synthesis of two kinds of ZnO nanostructures by vapor phase method. *Materials Letters*, 61(4–5), pp.1170–1173.
- [78] Ong, W.-J., Voon, S.-Y., Tan, L.-L., Goh, B.T., Yong, S.-T. and Chai, S.-P. (2014). Enhanced Daylight-Induced Photocatalytic Activity of Solvent Exfoliated Graphene (SEG)/ZnO Hybrid Nanocomposites toward Degradation of Reactive Black 5. *Industrial & Engineering Chemistry Research*, 53(44), pp.17333–17344.
- [79] Zhang, X., Xia, Y. and He, T. (2012). Tuning photoluminescence properties of ZnO nanorods via surface modification. *Materials Chemistry and Physics*, 137(2), pp.622–627.
- [80] Hong, R.Y., Li, J.H., Chen, L.L., Liu, D.Q., Li, H.Z., Zheng, Y. and Ding, J. (2009). Synthesis, surface modification and photocatalytic property of ZnO nanoparticles. *Powder Technology*, 189(3), pp.426–432.

- [81] Ao, W., Li, J., Yang, H., Zeng, X., Ma, X. Mechanochemical synthesis of zinc oxide nanocrystalline. *Powder Technol.* 2006, 168, pp.128–151.
- [82] Stanković, A., Veselinović, L.J., Skapin, S.D., Marković, S., Uskoković, D. Controlled mechanochemically assisted synthesis of ZnO nanopowders in the presence of oxalic acid. *J. Mater. Sci.* 2011, 46, pp.3716–3724.
- [83] Tsuzuki, T., McCormick, P.G. ZnO nanoparticles synthesis by mechanochemical processing. *Scr. Mater.* 2001, 44, pp.1731–1734.
- [84] Kołodziejczak-Radzimska, A., Jesionowski, T., Krysztafkiewicz, A. Obtaining zinc oxide from aqueous solutions of KOH and $Zn(CH_3COO)_2$. *Physicochem. Probl. Miner. Process.* 2010, 44, pp.93–102.
- [85] Wang, Y., Zhang, C., Bi, S., Luo, G. Preparation of ZnO nanoparticles using the direct precipitation method in a membrane dispersion micro-structured reactor. *Powder Technol.* 2010, 202, pp.130–136.
- [86] Benhebal, H., Chaib, M., Salomon, T., Geens, J., Leonard, A., Lambert, S.D., Crine, M., Heinrichs, B. Photocatalytic degradation of phenol and benzoic acid using zinc oxide powders prepared by sol-gel process. *Alex. Eng. J.* 2013, 52, pp.517–523.
- [87] Chandrasekaran, P., Viruthagiri, G. and Srinivasan, N. (2012). The effect of various capping agents on the surface modifications of sol-gel synthesised ZnO nanoparticles. *Journal of Alloys and Compounds*, 540, pp.89–93.
- [88] Vafaei, M. and Ghamsari, M.S. (2007). Preparation and characterization of ZnO nanoparticles by a novel sol-gel route. *Materials Letters*, 61(14–15), pp.3265–3268.
- [89] Mahdavi, R. and Talesh, S.S.A. (2017). Sol-gel synthesis, structural and enhanced photocatalytic performance of Al doped ZnO nanoparticles. *Advanced Powder Technology*, 28(5), pp.1418–1425.
- [90] Davar, F. and Salavati-Niasari, M. (2011). Synthesis and characterization of spinel-type zinc aluminate nanoparticles by a modified sol-gel method using new precursor. *Journal of Alloys and Compounds*, 509(5), pp.2487–2492.
- [91] Ba-Abbad, M.M., Kadhum, A.A.H., Mohamad, A.B., Takriff, M.S. and Sopian, K. (2013). Visible light photocatalytic activity of Fe³⁺-doped ZnO nanoparticle prepared via sol-gel technique. *Chemosphere*, 91(11), pp.1604–1611.
- [92] Ciciliati, M.A., Silva, M.F., Fernandes, D.M., de Melo, M.A.C., Hechenleitner, A.A.W. and Pineda, E.A.G. (2015). Fe-doped ZnO nanoparticles: Synthesis by a modified sol-gel method and characterization. *Materials Letters*, 159, pp.84–86.
- [93] Wang, F., Qin, X., Guo, Z., Meng, Y., Yang, L. and Ming, Y. (2013). Hydrothermal synthesis of dumbbell-shaped ZnO microstructures. *Ceramics International*, 39(8), pp.8969–8973.
- [94] Fang, Y., Li, Z., Xu, S., Han, D. and Lu, D. (2013). Optical properties and photocatalytic activities of spherical ZnO and flower-like ZnO structures synthesized by facile hydrothermal method. *Journal of Alloys and Compounds*, 575, pp.359–363.

- [95] Baruwati, B., Kumar, D.K. and Manorama, S.V. (2006). Hydrothermal synthesis of highly crystalline ZnO nanoparticles: A competitive sensor for LPG and EtOH. *Sensors and Actuators B: Chemical*, 119(2), pp.676–682.
- [96] Chen, D., Cio, X., Cheng, G. Hydrothermal synthesis of zinc oxide powders with different morphologies. *Solid State Commun.* 2000, 113, pp.363–366.
- [97] Lim, S.K., Hwang, S.-H., Kim, S. and Park, H. (2011). Preparation of ZnO nanorods by microemulsion synthesis and their application as a CO gas sensor. *Sensors and Actuators B: Chemical*, 160(1), pp.94–98.
- [98] Vorobyova, S.A., Lesnikovich, A.I., Mushinski, V.V. Interphase synthesis and characterization of zinc oxide. *Materials Letter* 2004, 58, pp.863–866.
- [99] Ghosh, S., Majumder, D., Sen, A. and Roy, S. (2014). Facile sonochemical synthesis of zinc oxide nanoflakes at room temperature. *Materials Letters*, 130, pp.215–217.
- [100] Hasanpoor, M., Aliofkhaezai, M. and Delavari, H. (2015). Microwave-assisted Synthesis of Zinc Oxide Nanoparticles. *Procedia Materials Science*, 11, pp.320–325.
- [101] Jiang, D.Y., Zhao, J.X., Zhao, M., Liang, Q.C., Gao, S., Qin, J.M., Zhao, Y.J. and Li, A. (2012). Optical waveguide based on ZnO nanowires prepared by a thermal evaporation process. *Journal of Alloys and Compounds*, 532, pp.31–33.
- [102] Ma, X., Zhang, J., Lu, J. and Ye, Z. (2010). Room temperature growth and properties of ZnO films by pulsed laser deposition. *Applied Surface Science*, 257(4), pp.1310–1313.
- [103] Ouyang, W. and Zhu, J. (2008). Catalyst-free synthesis of macro-scale ZnO nanonail arrays on Si substrate by simple physical vapor deposition. *Materials Letters*, 62(17–18), pp.2557–2560.
- [104] Zhang, N., Yi, R., Shi, R., Gao, G., Chen, G. and Liu, X. (2009). Novel rose-like ZnO nanoflowers synthesized by chemical vapor deposition. *Materials Letters*, 63(3–4), pp.496–499.
- [105] Lee, C.-H. and Kim, D.-W. (2013). Thickness dependence of microstructure and properties of ZnO thin films deposited by metal-organic chemical vapor deposition using ultrasonic nebulization. *Thin Solid Films*, 546, pp.38–41.
- [106] Wang, C., Chen, Z., Hu, H. and Zhang, D. (2009). Effect of the oxygen pressure on the microstructure and optical properties of ZnO films prepared by laser molecular beam epitaxy. *Physica B: Condensed Matter*, 404(21), pp.4075–4082.
- [107] Das, A., Wang, D.Y., Leuteritz, A., Subramaniam, K., Greenwell, H.C., Wagenknecht, U., Heinrich, G. Preparation of zinc oxide free, transparent rubber nanocomposites using a layered double hydroxide filler. *J. Mater. Chem.* 2011, 21, pp.7194–7200.
- [108] Yuan, Z., Zhou, W., Hu, T., Chen, Y., Li, F., Xu, Z., Wang, X. Fabrication and properties of silicone rubber/ZnO nanocomposites via in situ surface hydrosilylation. *Surf. Rev. Lett.* 2011, 18, pp.33–38.

- [109] Liu, H., Yang, D., Yang, H., Zhang, H., Zhang, W., Fang, Y., Liu, Z., Tian, L., Lin, B., Yan, J., et al. Comparative study of respiratory tract immune toxicity induced by three sterilization nanoparticles: Silver, zinc oxide and titanium oxide. *J. Hazard. Mater.* 2013, 248, pp.478–486.
- [110] Mirhosseini, M., Firouzabadi, F. Antibacterial activity of zinc oxide nanoparticle suspensions on food-borne pathogens. *Int. J. Dairy Technol.* 2012, 65, pp.1–5.
- [111] Mason, P. Physiological and medicinal zinc. *Pharm. J.* 2006, 276, pp.271–274.
- [112] Newman, M.D., Stotland, M., Ellis, J.I. The safety of nanosized particles in titanium dioxide and zinc oxide-based sunscreens. *J. Am. Acad. Dermatol.* 2009, 61, pp.685–692.
- [113] Gao, Q., Zhu, Q., Guo, Y. Formation of highly hydrophobic surfaces on cotton and polyester fabrics using silica sol nanoparticles and nonfluorinated alkylsilane. *Ind. Eng. Chem. Res.* 2009, 48, pp.9797–9803.
- [114] Atienzar, P., Ishwara, T., Illy, B.N., Ryan, M.P., O'Regan, B.C., Durrant, J.R., Nelson, J. Control of photocurrent generation in polymer/ZnO nanorod solar cells by using a solution-processed TiO₂ overlayer. *Phys. Chem. Letter.* 2010, 1, pp.708–713.
- [115] Lim, Z.H., Chia, Z.X., Kevin, M., Wong, A.S.W., Ho, G.W. A facile approach towards ZnO nanorods conductive textile for room temperature multifunctional sensors. *Sens. Actuators B Chem.* 2010, 151, pp.121–126.
- [116] Liu, Y., Zhou, J., Larbot, A., Persin, M. Preparation and characterization of nano-zinc oxide. *J. Mater. Process. Technol.* 2007, 189, pp.379–383.
- [117] Mansouri, S., Bourguiga, R., Yakuphanoglu, F. Analytic model for ZnO-thin film transistor under dark and UV illumination. *Curr. Appl. Phys.* 2012, 12, pp.1619–1623.
- [118] Gunaratne, K.D., Berkdemir, C., Harmon, C.L., Castelman, A.W., Jr. Investigating the relative stabilities and electronic properties of small zinc oxide clusters. *J. Phys. Chem. A* 2012, 116, pp.12429–12437.
- [119] Mikrajuddin, F., Okuyama, K., Shi, F.G. Stable photoluminescence of zinc oxide quantum dots in silica nanoparticles matrix prepared by the combined sol-gel and spray drying method. *J. Appl. Phys.* 2001, 89, pp.6431–6434.
- [120] Tang, Z.K., Wong, G.K.L., Yu, P., Kawasaki, M., Ohtomo, A., Koinuma, H., Segawa, Y. Room-temperature ultraviolet laser emission from self-assembled ZnO microcrystallite thin films. *Appl. Phys. Lett.* 1998, 72, pp.3270–3272.
- [121] Wang, M., Wang, X. Electrodeposition zinc-oxide inverse opal and its application in hybrid photovoltaics. *Sol. Energy Mater. Sol. Cells* 2008, 92, pp.357–362.
- [122] Soares, J.W., Whitten, J.E., Oblas, D.W., Steeves, D.M. Novel photoluminescence properties of surface-modified nanocrystalline zinc oxide: Toward a reactive scaffold. *Langmuir* 2008, 24, pp.371–374.
- [123] Roy, S., Basu, S. Improved zinc oxide films for gas sensor applications. *Bull. Mater. Sci.* 2002, 25, pp.513–515.

- [124] Samarasekara, P., Yapa, N., Kumara, N., Perera, M. CO₂ gas sensitivity of sputtered zinc oxide thin films. *Bull. Mater. Sci.* 2007, 30, pp.113–116.
- [125] Tsonos, C., Kanapitsas, A., Triantis, D., Anastasiadis, C., Stavrakas, I., Pissis, P., Neagu, E. Interface states and MWS polarization contributions to the dielectric response of low voltage ZnO varistor. *Ceram. Int.* 2011, 37, pp.207–214.
- [126] Tu, Y., He, J., Wang, Q., Liu, M., Xu, G., Ding, L. Measurement of thermally stimulated current in ZnO varistor. *Proc. CSEE* 2010, 30, pp.116–121.
- [127] Wöll, C. The chemistry and physics of zinc oxide surfaces. *Prog. Surf. Sci.* 2007, 82, pp.55–120.
- [128] Espitia, P.J.P., Soares, N.F.F., Coimbra, J.S.R., de Andrade, N.J., Cruz, R.S., Medeiros, E.A.A. Zinc oxide nanoparticles: Synthesis, antimicrobial activity and food packaging applications. *Food Bioprocess Technol.* 2012, 5, pp.1447–1464.
- [129] Klingshirn, C. ZnO: From basics towards applications. *Phys. Status Solidi* 2007, 244, pp.3027–3073.
- [130] Usman Ali, S.M., Alvi, N.H., Ibupoto, Z., Nur, O., Willander, M., Danielsson, B. Selective potentiometric determination of uric acid with uricase immobilized on ZnO nanowires. *Sens. Actuators B Chem.* 2011, 152, pp.241–247.
- [131] Brayner, R., Ferrari-Iliou, R., Brivois, N., Djediat, S., Benedetti, M.F., Fievet, F. Toxicological impact studies based on *Escherichia coli* bacteria in ultrafine ZnO nanoparticles colloidal medium. *Nano Letter.* 2006, 6, pp.866–870.
- [132] Peng, W.Q., Qu, S.C., Cong, G.W. and Wang, Z.G. (2006). Structure and visible luminescence of ZnO nanoparticles. *Materials Science in Semiconductor Processing*, 9(1–3), pp.156–159.
- [133] Krithiga, R. and Chandrasekaran, G. (2009). Synthesis, structural and optical properties of vanadium doped zinc oxide nanograins. *Journal of Crystal Growth*, 311(21), pp.4610–4614.
- [134] Hayat, K., Gondal, M.A., Khaled, M.M., Ahmed, S. and Shemsi, A.M. (2011). Nano ZnO synthesis by modified sol gel method and its application in heterogeneous photocatalytic removal of phenol from water. *Applied Catalysis A: General*, 393(1–2), pp.122–129.
- [135] Habibi, M.H. and Karimi, B. (2014). Preparation, Characterization, and Application of Zinc Oxide Nanoparticles by Sol-Gel Pyrolysis Method: Influence of Annealing Temperature on Crystalline Phases. *Synthesis and Reactivity in Inorganic, Metal-Organic, and Nano-Metal Chemistry*, 44(9), pp.1291–1298.
- [136] Khataee, A., Saadi, S., Vahid, B., Joo, S.W. and Min, B.-K. (2016). Sonocatalytic degradation of Acid Blue 92 using sonochemically prepared samarium doped zinc oxide nanostructures. *Ultrasonics Sonochemistry*, 29, pp.27–38.